New Strategy to Evaluate the Effectiveness of New Treatments using Animal Models

Conference Paper · October 2014

CITATIONS
2

READS
184

4 authors:

Cibele Bugno Zamboni
Instituto de Pesquisas Energéticas e Nucleares
145 PUBLICATIONS **498** CITATIONS
SEE PROFILE

S. Metairon
45 PUBLICATIONS **101** CITATIONS
SEE PROFILE

Ivone Mulako Sato
Instituto de Pesquisas Energéticas e Nucleares
40 PUBLICATIONS **342** CITATIONS
SEE PROFILE

Marcia Almeida Rizzutto
University of São Paulo
176 PUBLICATIONS **1,359** CITATIONS
SEE PROFILE

Journal Information

Publisher:
Science and Engineering Publishing Company (www.seipub.org)

Editorial Office:
6815 E Manor Drive, Terre Haute, IN 47802, USA

Subscriptions:
TheReview of Applied Physics is quarterly published byScience and Engineering Publishing Company.

Subscription Rates:
To subscribe, please contact Journals Subscriptions Department:
E-mail: rap@seipub.org

Advertisements Service:
Advertisements Sales Department:
E-mail: rap@seipub.org

Reprints:
Reprints Coordinator: Science and Engineering Publishing Company

Production Information:
For manuscripts that have been accepted for publication, please contact:
E-mail: rap@seipub.org

Pricing:
Single Volume Price: $100

Review of Applied Physics

Journal Information

RAP is published by Science and Engineering Publishing Company.RAP is an international open-access journal, aiming to promote diffusion of applied physicsthrough setting a platform for educators to share the experiences.

Scholars from all relevant academia fields are invited to submit high-quality manuscripts that describe the latest research results or innovations. Besides, all the submissions will be peer-reviewed by experts of the same research fields.

Volume 3, 2014

Review of Applied Physics

Contents

Volume 3, 2014

Editorial Board Members

Editor-in-Chief

Editorial Board Members

Investigations of the Nonlinear Optical Phenomena in the Series of Multiatomic Compounds by the Methods of Speeds of Balance Populations and Deactivation on Pumping in the Electronic Excited States

Alexander E. Obukhov

National Research University "Moscow Power Engineering Institute", Krasnokazarmennaya st., 14. 111250, Moscow, Russia

aobukhov@fo.gpi.ru

Received 4 June 2013; Accepted 14 June 2013; Published 13 March 2014

Abstract

With the help of the measurements (the methods are the NMR 1H and 13C, infrared (IR) and the UV-absorption, Raman scattering of light, the fluorescence and the phosphorescence, the pumping of the lasers and lamps, the low-temperature of the spectroscopy in the solutions and vapor and also with application by the methods of balance speeds of populations and deactivation the energy of pumping in the electronic excited states, and the spectroscopy of properties in the range $\lambda_{abs,osc}^{max}$ = 208 - 760 nm have been investigated. Therefore, creation of the complex methods of studying the NMR-magnetic and the optical properties at variations of the electronic and spatial structures in the series three-, penta- and quinclicycles from bi- and bis- of phenyl, furyl-, thienyl- and pyridines and oxazoles and -oxadiazoles the organic compounds. The applications by the fundamental scientific problem of the formation for the quantum technologies and engineering, which allows predicting the practical synthesis of compounds with given the spatial and electronic structures and required the physical properties even before realization of practical synthesis of the luminophores.

Keywords

Spectra; Optical; Photophysic; Electronic Excited States; Dye-laser; Nanocurrent; Quantum Yields; Lifetime of Fluorescence; UV-Absorptions; NMR and IR Absorptions; Raman Scattering; Multiatomic Compounds; Dye-laser

Introductions

Wide introduction in practice of the photophysical, chemical and biological researches of various assignment of the spectral methods of studying of the optical and magnetic properties of the organic and inorganic compounds simultaneously allows to study and widely to apply individual spectral characteristics in the vapor, solutions or crystals with the purpose of interpretation of their the nonlinear photophysical properties of the relaxation formed for time intervals from hundreds and tens up to nano-, pico-, femto- and attoseconds. Therefore, reason of the complex methods of studying of the NMR-magnetic and of the optical properties in the series multiatomic compounds for the decision of fundamental scientific problem it is formation of the new quantum model of nanotechnologies for the science and engineering, which allow to predict required properties even before realization of practical synthesis of organics luminophores. [1 - 5]

Experimental and Theoretical Methods and Materials

In article complex application of nonlinear optical phenomena in the series multiatomic compounds with the help of mechanisms the superfine electronic-nuclear interactions (SFElNIn) in the singlets and triplets electronic excited states and the methods of spectroscopy were investigations. [2, 4]

Materials

All new compounds were synthesized for the decision of the given fundamental spectral problem, and their

structural formulas in papers are considered. [1 - 5]

Methods of Masurements of Spectra

The infrared absorption (IR-) spectra ($\lambda_{abs}^{\max}$) in the Kbr pellets is "Specord-75-IR" spectrometer, and the electronic UV-spectrums of solutions at 296 K is "Specord-M4030" spectrometers (German), and NMR ^{1}H and ^{13}C spectra is "Bruker"-80MGz and 250MGz were measured. Were also used X-ray structural data on the equilibrium of the nuclear configuration in the singlet ground state (S_0 , GrSt) [2, 6]. The fluorescence (Fl) spectrums (W_{fl}^{ν}/ν^3, $\lambda_{osc}^{\max}$), and the fluorescence quantum yields, (QYFl) γ_{fl} , and lifetimes, (LtFl) τ_{fl} , is "SLM-48OOS" (USA) spectrafluorimeter were measured. The duration of fluorescence (Fl), τ_{fl} , with the use of the two techniques: phase and modulation of the methods was measured. The generation radiated of light (GRl) the properties during pumping of solutions of the complex molecules in a transverse arrangement by a "Lambda Physic" excimer laser (Canada), which could provide a single pump pulse, $\Delta\tau_{exit}^{1/2}$, power density of more then, $E_{exit} \geq\leq$ 0,1-35 mJ/cm^2 were measured. The wavelengths of the laser pump-pulse were used: λ_{exit} ≈ 308 nm (XeCl*), λ_{exit} ≈ 248 nm (KrF*), λ_{exit} ≈337 nm (gas N_2). [1 - 5]

The Spectroscopy of Ground States

The mechanisms of superfine a fermi-contact electron-nuclear interaction FC-SFElNIn arises that the nucleus has the magnetic dipole of moment of the spatial and electronics structure of multiatomic compounds in Tables 1, 2 and 3.

The Fermi-contact and Dipole-dipole of Superfine Electron-nuclear Interactions of Mechanisms in the NMR-spectra

At research of the NMR spectrums of compounds in grounds states (S_0 , GrSt) it is necessary to take into account, that contribution to the constant of shielding σ_i^{scr} (in the chemical shifts is chsh) for each nucleus ($H_0\left(1-\sigma_i^{scr}\right)$) in molecule or the complex in NMR spectra as function which is directly proportional to the square $\left(\Delta\rho_{\pi\sigma\ln Z}^{oi}\right)^2$ to the EfTED and is inversely proportional to the cube of distances ($1/R_i^3$) between the valent of bonds by the ratio

$$\Delta\sigma_i^{screen} = -(\mu_0/4\pi)\left(\left(\Delta\rho_{\pi\sigma\ln,Z}^{oi}\right)^2 r^2 \Big/ 2m_e R_i^3\right). \quad (1)$$

According to statement of fundamental problem [1,2,4] for the nucleus ^{1}H and ^{13}C in similar positions in the spatial structure of compounds of the GrSt in the NMR spectrum average of the value SFElNIn, and always change in ranks of bonds, that is determined by character localization of the full EfTED ($\rho_{\pi z}^{0i}$) on the atoms owing to presence the ratio

$$\langle A\rangle = -\left(\mu_0 h/6\pi^2\right)\gamma_s\gamma_I\left|\psi(0)\right|^2 = (4/3)\pi\beta q_N\alpha\beta_N(\rho_{\pi z}^{0i}) = K\int\psi^2\sum_i\left[2S_{\mu\nu}\delta(N)\right]\psi\, d\psi, \quad (2)$$

where β_N is the Bore's-magneton, $S_{\mu\nu}$ is the integral by exchanges between overlaps for μ and ν nucleus, backs of nucleus is $\vec{I}$ and is $\vec{s}$ electron, $\psi(0)$ is wave functions or the EfTED on the nucleus.

The electron has the spin-magnetic moment that determines other fundamental mechanism is the spatial dipole-dipole DD-SFElNIn with the magnetic field of the own nucleus, and also others nucleus in the spatials structure of compounds representations by formula

$$F_i(\theta_i,\phi_i,r_i) = \left\langle D_1^{ax}\times(3Cos^2\Omega_i-1)]/r_i^3\right\rangle + +\left\langle D_2^{nax}\left(Sin^2\Omega_i Cos2\alpha_i/r_i^3\right)\right\rangle, \quad (3)$$

where D_1^{ax} and D_2^{nax} is coefficients of anisotropy of the magnetic susceptibility which can be determined by the following expressions as

$$D_1^{ax} = [\beta_e S_{Ze}(S_{Ze}+1)/45KT]\times(3g_{II}+4g_{\perp})(g_{II}-g_{\perp})$$

and $D_2^{nax} = -1/2(\chi_x-\chi_y)$, here g_e and g is the electron factor of Lande's, β_e is Bore's magneton, $g_{\perp}$ and g_{II} is perpendicular and parallel components of g -factor, S_Z is total backs, K is the Bolzman's constant, T K is the absolute temperature, χ_x and χ_y is the magnetic susceptibility of the complex along axes oX and oY , Ω_i , α_i r_i is spherical coordinates of the nucleus and r_i is distance between the spin-spin interactions (SpSpIn) of nucleus in spatial structure is observed.

The stereo-specific of the geminale SpSpIn between interactions of the nucleus, are defined from the following is ratio

$${}^3J_{CH} = K_H K_C\times\sum_i^{HOMO}\sum_j^{LFMO}\Delta E_{ij}^{-1}\left(C_{i,2S}C_{j,2S}C_{i,1S}C_{j,1S}\right)^2, \quad (4)$$

where $\Delta E_{ij} = \varepsilon_j - \varepsilon_i - K_{ij}$ is the gap energy between the heighest occupied (***HOMOs***) and the lowest free the molecular orbitals (***LFMOs***) in relation of GrSt S_0, C_{ij} is the coefficients by calculations the LCAO-MO SCF expended-CI INDO/S methods.

Let's note, that for the series of phenyl-, furyl- and thienylbisoxazole (OPO, OFO, OTO, and also POPOP, FOPOF, TDPDT and others) nucleus of carbon and the protons located symmetrically concerning the vertical axis (C_{2V}) of the second order have equal of vicinale SpSpIn and geminale SpSpIn and also that defines $\sum_i \rho^{0i}_{\sigma\pi,Z}$ on the atoms in the structure (i.e. carbons, sulfur, nitrogen, and other), them as equivalent groups quasi-oscillators. [1 - 5]

Similar results for the pyridine-containing of compounds ([1-4]azafluorene) are observed. [4]

The studying of NMR-spectra in solutions has shown that the compounds, of incorporating the oxazole or oxadiazole, pyridines cycles with the central of benzene cycles in the spatial structure, have high of aromatics.

The Atomic-nano-current in the Structure

In the quantum mechanics the EfTED ($\sum_i \rho^{0i}_{\sigma\pi,Z}$) located on the atoms of the spatial structure of compounds in shares of the ones of electrons (e) that it is possible to receive the similar form of expression for size of force of the current i_{icur} for $\sigma\pi^*, \pi\pi^*$-electron of the atoms of the carbon in the several heterocyclic is defined and thus, secondary magnetic field $B' = -B_0\sigma^{scr}$ in the NMR spectrometer of this dipole action on the proton atoms located on distance R_i from the centre of the cycle is equal $\mu = R_i^3$ and can be determined from expression

$$B' = -\left(\mu_0/4\pi\right) B_0 \left(3\left(\Delta\rho^{oi}_{\pi\sigma \ln Z}\right)^2 r^2 \Big/ 2m_e R_i^3 \right) \quad (5)$$

where σ^{scr} is the constant of shielding of the each nucleus in the structure of compounds.

For the investigated compounds in the GrSt (S_0) the values EfTED on different types of the atoms is the source (the nano-quasioscillators of minimal size) weak by the electric nanocurrent. [2,4]

Thus, in the atomic models for the multinuclear compounds transfer of the logic-spectral information can be carried out only by change of the nature of mechanizms SFElNIn from the donor to the acceptor which the formed by of a spatial and electronic structure.

Raman Scattering and Infrared Absorptions Spectra

According to the carried out researches in the IR-absorption and Raman scattering in the series poly- and heteroaromatic compounds in the singlet GrSt in the range of the frequencies is (3600 - 3100 cm-1 and 1600 - 1630) cm-1 and (1540 - 1534) cm-1 should correspond to the most high-frequency and intensive combinational strips by the symmetric and the nonsymmetric types is double and unary≤C -H, =N-N=, =C-C=, =C-N=, >C=C< is 415, 495, 530, 695, 720, 772, 810, 858, 910, 980, 1015, 1075, 1110, 1180, 1255, 1305, 1320, 1350, 1420, 1440, 1490, 1530, 1562, 1580, 1620, 2800-3200 cm-1 and the intensive of vibration-deformations or nonfullsymmetry and fullsymmetry of valent bonds in oxazoles and oxadiazoles cycles is B_{1U}, B_{2U} B_{3U} types arises are observed. [2,4,7]

The more rotary and oscillatory degrees of freedom typically for a given of spatial configuration, and thus, there the instability of spatial structure in vapor and solutions is more.

The Specroscopy of Electronic Excited States

In the quantum theory mechanisms of nonlinear optics and spectroscopy can be considered with application the UV-quantum model of speeds of balance populations which allows from establish of the photophysical properties in different conditions are investigations in Fig. 1.

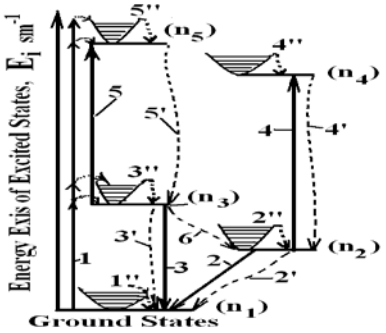

FIG. 1. THE FIVE-LEVELS SYSTEM FROM THE MULTI-ATOMIC MOLECULES. (1) IS THE PROCESS ENERGY OF LASERS PUMPING, (2 AND 2') IS PHOSPHORESCENCE OF THE RADIATION AND NONRADIATED TRANSITIONS, (3 AND 3') IS OF THE FLUORESCENCE OF RADIATION AND THE NONRADIATED TRANSITIONS, (4 AND 5) THE SINGLET-SINGLET AND THE TRIPLET-TRIPLET REABSORPTION OF TRANSITIONS, (2', 3', 4' AND 5') THE INNERCOMBINATION CONVERSIONS OF TRANSITIONS, (1'', 2'', 3'', 4'', 5'') OR (PICOSECONDS OF THE ELECTRON-VIBRATION RELAXATION), (6) IS INTERCOMBINATION CONVERSIONS OF TRANSITIONS.

The Models Speeds of Balance of Populations

When organic molecules are excited with UV pumping sources with a radiation energy > 3 - 4 eV and the lines corresponding to $S_3^* \to S_5^*$ and $T_2 \to T_4$ electronic transitions arise in the spectra of singlets and triplets electronic excited states before photon emission, these transitions playa dominant role in the formation of the gain strips, the lasing, and the multistage processes of multistrips photoionization in Fig. 1. [1, 2, 9, 10]

For a quantum particle with the thri- and five-levels scheme if vibration parameters of the connected dye [(compounds+solutions)+ resonator] satisfy in dye-laser to a ratio

$$\chi_{31}\left(\nu^{osc}\right) = \left[\mathrm{K}_{ampl}\left(\nu^{osc}\right) - \chi_{35}\left(\nu^{osc}\right) - \chi_{24}\left(\nu^{osc}\right)\right]\frac{p_{32}}{p_{31}}, \quad (6)$$

where is $\mathrm{K}_{ampl}(\nu)$ initial coefficient of losses of the resonator, $\chi_{31}\left(\nu^{osc}\right)$, $\chi_{35}\left(\nu^{osc}\right)$ and $\chi_{24}\left(\nu^{osc}\right)$ limiting coefficient of amplification and the singlet-singlets and triplet-triplets reabsorption spectra in dye-laser. [2]

Here the ratio $p_{31} = 1/k_{fl} = 1/k_{31} \approx \tau_{fl}/\gamma_{fl}$, and, $p_{32} = 1/k_{32} \approx \tau_{fl}/\left(1-\gamma_{fl}\right)$ are the probabilities of the radiation and non-radiation transition and less decay of the Fl-spectra (State S_1^*) and Ph-spectra (State T_1) levels: $\tau_{fl} = 1/\tau_{fl}^0$, and $\tau_{ph} = \gamma_{ph}/\gamma_T\tau_{ph}^0$, where τ_{fl}, γ_{fl}, and γ_T is measurement the radiating lifetime (RLtFl) and quantum yield Fl (QYFl). [1]

The cross sections of the transitions between the interacting of the five levels in dye-laser (or OLEDs) at the wavelengths of pumping and lasing $\sigma_{2TT,3SS}^*(\nu^{exit,osc})$ are used as parameters in the latter formula as

$$\mathrm{K}_{ampl}(t,\nu) \cong \sigma_{31}^{osc}(\nu)n_3(t) \geq \sigma_{13}^{abs}(\nu)n_1(t) + \sigma_{24}^{reabs}(\nu)n_2(t) + \sigma_{35}^{reabs}(\nu)n_3(t) + \mathrm{K}_p^0(t,\nu) + \rho'(\nu), \quad (7)$$

where $\sigma_{31}^{osc}(\nu)$ is the stimulated emission cross section (or the GRl) and $\sigma_{13}^{abs}(\nu)$, and $\sigma_{24}^{reabs}(\nu)$, $\sigma_{35}^{reabs}(\nu)$ are the cross sections of UV-absorptions and $S_1^* \to S_5^*$, and $T_1 \to T_4$ -reabsorption spectra and on laser excitation frequency $\nu^{osc,exit}$ at the electronic multistage transitions are $S_0 \to S_1^*$ <≈> S_1^*, S_1^* ≈> T_1, $S_1^* \to S_5^*$, S_1^* <≈> S_5^*, $T_1 \to T_4$ and T_1 <≈> T_4, T_1 <≈> S_1^* in the full spectra of STElExSt.

Thus, one should know the form of the spectral functions $\sigma_{31}^{osc}(\nu)$, $\sigma_{13}^{abs}(\nu^{exit})$, $\mathrm{K}_{ampl}(\nu^{osc})$, $\sigma_{35}^{reabs}(\nu^{osc,exit})$, $\sigma_{24}^{reabs}(\nu^{osc,exit})$, and $\chi_{31}(\nu^{osc})$ to determine the generation radiated of lithg (GRl) and laser excitation frequency $\nu^{osc,exit}$ and the approximate threshold values of the laser limit power P_{exit}, and laser energy of limit pump-pulse E_{lp}.

The cross section of the emission also low also make $\sigma_{31}^{osc}(\nu)$ ≈ 10^{-19} - 10^{-18}, cm^2 in Table 4.

TABLE 1. THE CHEMICAL SHIFTS OF THE PHOTONS IN THE SERIES COMPOUNDS IN THE NMR SPECTRA

Compounds	Chemical shifts of protons, chsh (ppl)				
	Number of atoms				
	$H_{(4)}$[(a)]	$H_{(5)}$	$H_{(3')}$	$H_{(4')}$	$H_{(5')}$
2-(2-phenyl)-oxazol-5-formilcarboaldehid (***PO-COOH***)* (signal -COH)	7,07s (9,75s)*	- 7,51s	6,87dd 6,79dd	6,35dd 7,94dd	7,45d.wid.
2-(2-thienyl-)oxazol-5-carboaldehid (***FO-5-COH***)*	8,07s (9,8s)*	7,51s	8,12m (2H)	7,51s	7,85m -
2′-phenyl-2,5′-bioxazol (***POO***)	7,17s				7,40m (3H)
2′-(furyl-2)-2,5′-bioxazol (***FOO***)	7,39d	8,37d	7,27 dd	6,74dd	7,88dd
2′-(thienyl-2)-2,5′-bioxazol (***TOO***)	7,41s	8,12s	7,85 dd	7,27dd	7,79dd
1,4-phenylen-2,2′-bisoxazol (***OPO***)	7,76s	8,12s	7,3s (4H)	-	7,4 m (3H)
1,4-furylene-2,2′-bisoxazol (***OFO***)	7,36s	8,08s	7,25s (2H)	-	7,4 m (3H)
1,4-thienylen-2,2′-bisoxazol (***OTO***)	7,6s	7,92s	7,23s (2H)	-	7,4 m (3H)

The note: The signals of protons look like overlapped multiplets J_{45} = 7 ÷ 8 Gz, (*) in solution CCl_4 and (**) in the solution $CDCl_3$. In the spectrum on frequence 250 MGz splitting protons of oxazole cycle J_{45} = 0,7 Gz, and also in thiofene cycle J_{34} = 3,5 Gz is observed; J_{35} = 1,0 Gz; J_{45} = 5 Gz and in thiofene cycle $J_{3'4}$ = 4 Gz, $J_{3'5}$ = 1,5 Gz, $J_{4'5}$ =5,5 Gz, (e) in furane cycle $J_{3'5'}$ = 3,5 Gz, $J_{3'4'}$ = 2,5 Gz, (j) is CSSI $J_{4'5'}$ and $J_{3'5}$ but in spectrum NMR ^1H on frequency 60 and 80 MGz are not shown.

TABLE 2. THE CHEMICAL SHIFTS OF THE PHOTONS IN THE SERIES [1-4]-AZAFLUORENES IN THE NMR SPECTRA

Compounds	Solutions	Numeration of protons, J(Gz)									
		$H_{(1)}$	$H_{(2)}$	$H_{(3)}$	$H_{(4)}$	$H_{(5)}$	$H_{(6)}$	$H_{(7)}$	$H_{(8)}$	9-CH_2	3-CH_3
[1]-azafluorene	*azetone-d6*		8,25	7,11	7,93	7,67	7,2	7,17	7,42	3,85	
	CDCl3	-	8,29	7,08	7,77	7,58	7,2	7,18	7,37	3,88	
	DMSO		8,32	7,18	8,07	7,6	7,25	7,28	7,45	3,94	
[2]-azafluorene	ацетон d6	8,7	-	8,48	7,70	7,81	7,31	7,37	7,58	4,1	-
3-Metyl-[3]azafluorene	*Azetone-d6*	8,6			7,41	7,7	7,2	7,21	7,39	3,94	2,61
	CDCl3	8,43	-	-	7,03	7,58	7,17	7,17	7,37	3,75	2,55
	DMSO	8,50			7,6	7,68	7,16	7,17	,36	3,88	2,58
[4]azafluorene	*Azetone-d6*	7,74	7,09	8,38		7,89	7,31	7,28	7,46	3,58	
	CDCl3	7,64	7,04	8,47		8,01	7,34	7,3	7,44	3,71	
	DMSO *	7,86	7,2	8,42		7,88	7,35	7,33	7,54	3,88	

TABLE 3. THE CONSTANT OF THE SPIN-SPIN INTERACTIONS (CSPSPIN) BETWEEN THE PROTONS IN THE SERIES [1-4]-AZAFLUORENES IN THE NMR SPECTRA IN SOLUTIONS CDCL3

Compounds	Numeration interactions of protons, J(Gz)								
	$J_{(2-3)}$	$J_{(2-4)}$	$J_{(3-4)}$	$J_{(5-6)}$	$J_{(5-7)}$	$J_{(5-8)}$	$J_{(6-7)}$	$J_{(6-8)}$	$J_{(7-8)}$
[1]-azafluorene	4,9	1,6	7,5	7,6	1,0	0,8	7,6	1,1	7,5
[2]-azafluorene	-	-	7,1	7,7	1,2	0,7	7,5	1,1	7,6
[4]azafluorene	4,8	$J_{(1-3)}$ 1,5	$J_{(1-2)}$ 7,5	7,4	1,3	0,8	7,1	1,0	7,4

Thus, the QYFl γ_{fl} and LtFl τ_{fl}, which can be measured experimentally for given conditions, contain the information concerning the net effect of external factors on an compounds, although all the formulas involve parameters of innermolecule processes (the rate constants k_{nr}) related to one quantum of absorbed and one quant of emitted the fluorescence and phosphorescence in Table 1.

Variations of the Spectral-luminescence and Generation Radiated of Light Propertie

In these chapters of connection among themselves the spectral, luminescent and the GRl properties of the multinuclear compounds which can be applied in UV-dye-lasers (OLEDs) or as the biological molecules will be considered. [11]

This analysis will be based the spectral-fluorescence characteristics at the variations in the series of electron and spatial structure compounds in vapors and, solutions were measured in Table 4.

Variations the Series of Tri- and Pentacycles of Compounds

The shortest lasing wavelength were found in ***2-PO-5-COOH*** and ***2-PO-5-COOCH3*** (compounds 1 and 2), λ_{gen}^{max} =335 nm, and, λ_{gen}^{max} = 344 nm in DiEG at high threshold the limit energy of density dye-laser, E_{lp} = 8.0 mJ/cm², respectively in Fig. 2.

Of the complex molecules is the paraterphenyl (***PPP***), and 2,5-diphenyl-1,3-oxazole (***POP***) the GRl efficiently in solution is compounds 3 and 4 in Fig. 3.

The molecules 2,5-diphenyl-1,3,4-oxadiazole (***PDP***) in ethanol solutions and for density vapor 2,5-diphenylfurane (***PFP***) QYFl γ_{fl} = 0.84 and 0.62 and at threshold energy of density E_{lp} = 0.2 - 0.35 mJ/cm², respectively.

The value thresholds of the laser pump-pulse E_{lp}, falls in the transition from the bi- to corresponding the phenyl-, furyl-, thienyl- tricycles bis-oxazoles by the molecules is ***POO, FOO, TOO*** of compounds 5, 6, 7, to ***OPO, OFO, OTO*** is compounds 8, 9, and 10.

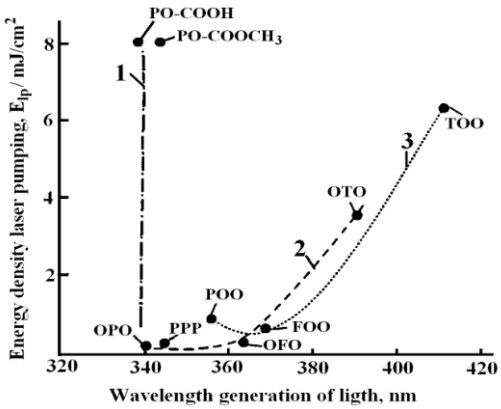

FIG. 2. THE DEPENDENCE OF THRESHOLD PUMP ENERGY DENSITY E_{lp} ON THE LASING WAVELENGTH 320 - 420 NM IN SOLUTIONS OF ETHANOL FOR THE COMPOUNDS (STOKE – DASHED LINE 1) ARE ***PO-COOH***, AND ***PO-COOCH3*** (CONTINUOUS LINE 1); THE SERIES PHENYL-, FURYL-, THIENYL BISOXAZOLES ARE ***OPO, OFO, OTO*** (CONTINUOUS LINE 2) AND SERIES THE PHENYL-, FURYL-, THIENYL BIOXAZOLES ARE ***POO***, ***FOO***, ***TOO*** (CONTINUOUS LINE 2) FOR THE "CRITICS OF RANGE" ARE 320 - 340 NM IN THE UV-SPECTRA.

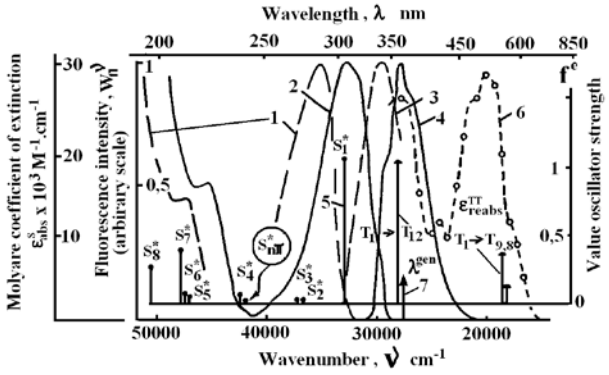

FIG. 3. THE ABSORPTIONS (ε_{abs}^{ν} , 1, 2) (1) IS VAPOUR AND (2) SOLUTIONS IN ETHANOL FOR THE MOLECULE 2-PHENYL-1,3-OXAZOL (***POP***). (1, 2) IS LINES OF VERTICAL CONTINUOUS A SHOW FREQUENCIES AND VALUE OF OSCILLATORS STRENGTH FOR ELECTRONIC TRANSITIONS $S_0 \to S_{1,2,...,8}^*$ ($\pi\pi^*$, $\sigma\pi^*$ -, $n\pi^*$ -TYPES) IN THE UV-ABSORPTIONS SPECTRA, (5) IS 0-0-TRANSITIONS, (3, 4) IS THE $T_1 \to T_{1,...,12}$ TRANSITIONS OF THE INDUCED OF LASER REABSORPTIONS OF SPECTRA BY CALCULATIONS THE LCAO-MO SCF EXTENDED-CI INDO/S METHODS [1].

The series of tricycles molecules in solvent ethanole+H_2SO_4 of Fl-spectra within the visible spectral region in the wavelength range to $\lambda_{gen}^{\max}$ = 390 - 420 nm and with QYFl γ_{fl} = 0.54 - 0.61, but do not GRl even at the high density pump-pulse E_{lp} of laser in Fig. 2.

For example, for the series of bisoxazole is ***OFO*** (compounds is 9) and bioxazoles is ***FOO*** (compounds is 6) with different QYFl γ_{fl} = 0.63 and γ_{fl} = 0.36 in ethanol of solutions, respectively, and also GRl and different thresholds a laser-pump-pulse E_{lp} = 0.33 and 0.73 mJ/cm², respectively in Fig. 2.

At excitation of solution of the 1,4-phenylene-2,2'-bisoxazole (***OPO***) (compounds is 8) by the laser pulse duration of 10 ns and wavelength of $\lambda_{exit}^{\max}(\nu)$ = 308 and 248 nm, the new dye-laser with minimally possible size of a threshold energy of pump density E_{lp} ≈ 0,1 - 0,5 mJ/cm² is received [1].

The latter is lower than the ***PPP***-molecule the GRl with parameters is $\lambda_{gen}^{\max}$ = 340 nm and, E_{lp} = 0.25 mJ/cm² in the ethanol, and thus, it is higher, than the value E_{lp} for the ***OPO*** E_{lp} = 0.14 mJ/cm² under of the same experiments in Fig. 3.

The series tricycles of compounds is 32 - 34 in solvent of ethanole+H_2SO_4 the Fl within the spectral of visible region in the wavelength range to $\lambda_{gen}^{\max}$ = 420 nm with QYFl γ_{fl} = 0.42, but do not the GRl even at the high density pump-pulse of laser. [1,2]

When for the ***OPO*** used as the solvent of 1,1,2,2'-trifluoroethanol we have, to parameter for dye-lasers are E_{lp} < 0.1 mJ/cm², and, $\lambda_{gen}^{\max}$ = 340 nm.

This is the only example known so far of semultaneous shortening the wavelength of GRl and lowering the value E_{lp} for the UV-dye-laser.

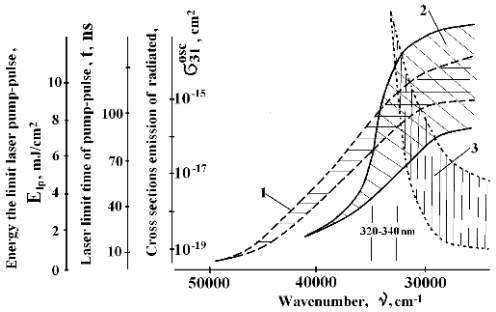

FIG. 4. THE NONLINEAR DEPENDENCE: THE LINE 1 - $\sigma_{31}^{osc}(\nu^{\max})$ ARE THE CROSS SECTIONS THE RADIATED OF LIGHT, LINE 2 - t_{lp} IS THE LIMIT TIME OF FIRST FRONT DURATIONS OF LASER PUMP-PULSE, LINE 3 - E_{lp} IS THE LIMIT THRESHOLD ENERGY OF DENSITY OF LASER PUMP-PULSE FOR "CRITICS OF RANGE" IN THE 320 - 340 NM AND OF RANGE 200 – 760 NM IN THE UV- AND VISIBLE SPECTRUM ARE MEASURED.

The series of pentacycles N-,O-,S-heteroaromatic compounds is 1 - 24 of Fl-spectra within the visible spectral region in the range $\lambda_{gen}^{\max}$ = 388 - 560 nm with QYFl γ_{fl} = 0.33 - 1.0 in Table 4 [1, 2].

When -***OPO***-, -***OFO***-, -***DPO***-, and -***DPD***- (compounds is 25 - 34) are employed as central fragments in the pentacycles of compounds that the QYFl may a range from γ_{fl} = 0.6 to 1.0 depending on the properties of solvents.

The marked compounds GRl with the least threshold density pump-pulse P_{lp} = 1.83 - 2.9 mJ/cm².

If -***OTO***-, -***DTO***-, and -***DTD***-, or other laser-active compounds are employed as central fragments in compounds 32, 33, 34 (is ***POTOP***, ***POTDP***, ***POTDT***), i.e., when the thiophene of cycles in centre of the spatial structure, then we have QYFl γ_{fl} = 0.36 to 0.47 depending on the properties of solvents is positioned, and these compounds GRl with P_{lp} = 4.22 - 5.3 mJ/cm².

The pentacycles of compounds in solvent ethanole+H_2SO_4 (of complexis and protonated) of Fl-spectra within the visible spectral region in the wavelength range $\lambda_{gen}^{\max}$ = 480 - 528 - 760 nm with QYFl γ_{fl} = 0.43 - 0.67, but do not GRl even at high density

P_{lp} capacity pump of laser.

But, in solvent of ethanole+H_2SO_4 the Fl-intensive within the visible spectral region in the wavelength range to λ_{gen}^{max} = 522 - 760 nm with QYFl γ_{fl} = 0.72 - 0.8, but do not GRl even at high density laser.

Time of Limit of First front the Pumping Pump Laser Pulse

The simplified relationship obtained on the basis of kinetic equations of the population balance from to ratio [1]

$$t_{lp} \le 2/k_{ST} \; \sigma_{31}^{osc}(\nu) / \sigma_{2TT}^{reabs}\left(\nu^{osc}\right) \approx \left[2\tau_{fl}/(1-\gamma_{fl})\right] \sigma_{3SS}^{reabs}\left(\nu^{osc}\right) / \sigma_{2TT}^{reabs}\left(\nu^{osc}\right), \quad (8)$$

where k_{ST} is the RC ItCC, $\sigma_{31}^{osc}(\nu)$ and $\sigma_{2TT}^{*}\left(\nu^{osc}\right)$ is the cross sections of stimulated emissions spectra and the triplet-triplets of reabsorptions spectra, respectively in the wavelength of Fl-spectra, ν_{fl}^{max}, and τ_{fl} and γ_{fl} is the LtFl and QYFl. [1-5,10]

The ***POP***-compounds in vapour the QYFl γ_{fl} decrease to γ_{fl} = 0.24 and increase QYFl γ_{fl} = 0.71 in ethanol. [1]

TABLE 4. THE SPECTRAL-FLUORESCENCE AND RADIATED OF LIGHT PARAMETERS FOR THE COMPOUNDS № 1 – 34 IN SOLUTIONS AND VAPOR ARE MEASURED, AND ALSO THE QUANTUM CHEMICAL OF CALCULATIONS BY LCAO-CSF CI INDO/S METHODS

No	Compound (abbreviation)	State of aggregation	λ_{abs}^{max}, *nm*	λ_{osc}^{max}, *nm*	γ_{fl}	ε_{abs}^{max}, 10^3, $M^{-1}\cdot cm^{-1}$	$k_{fl}x$ 10^9, s^{-1}	$k_{st}x$ 10^9, s^{-1}	$\sigma_{31}^{osc}x$ 10^{-16}, cm^2	$\sigma_{31}^{osc}x$ 10^{-16}, cm^2	$t_{lp}x$ 10^{-9}, *s*	E_{lp} (P_{lp}), *mJ* / (*mW*/) cm^2
1	2-phenyl oxazol-5-carboxylic Acid (***PO-5-COOH***)	ethanole DiEG vapor, INDO/S	276 282 271	(326, 335) -	0,03 0,18 0,01	34,1 31,5 -	10^{-3} 0,08 0,06	0,10 0,36 0,44	1,31 1,41 -	2,5 2,87 2,5	10^{-3} 5,9 10^{-3}	- 8,0 -
2	methyl-ether of 2-phenyl-oxazole-5-charboxylic acid (***PO-5-COOCH3***)	ethanole DiEG vapor, INDO/S	277 282 -	335 344 -	0,04 0,22	31,1 32,6 0,1	0,04 0,08 0,07	0,74 0,7 0,44	1,2 1,26 -	4,36 4,87 4,0	0,12 6,2 0,007	- 8,0 -
3	parater-phenyl (***PPP***)	ethanole vapor, laser vapor, lamp vapor, INDO/S	276 258 258 258	340 343 343 343	0,83 0,1 0,01 0,38	30,64 30 30 30	0,68 0,10 0,1 0,1	0,14 0,90 0,6 0,87	1,2 0,23 0,023 0,1	2,8 2,6 2,6 2,6	96,4 5,7 0,3 2,8	0,25 ≥1,8 - -
4	2-phenyl-1,3-oxazole (***POP***)	cyclohexane ethanole ethanole+H_2SO_4 toluene vapor, lamp vapor, laser vapor, INDO/S	302 303 314 306 289 290 290	356 362 406 382 352 350 349	0,81 0,71 0,51 0,51 0,24 0,012 0,24	34,0 29,6 21,0 29,1 9,2 9,2 -	0,58 0,44 0,23 0,72 0,26 0,010 0,61	0,14 0,18 0,21 0,96 0,85 1,10 0,69	13,0 11,4 0,81 11,2 0,36 0,35 0,40	0,84 0,86 0,03 0,48 0,21 0,02 0,34	7,5 1,1 0,07 - 1,2 0,06 2,0	7,5 6,5 0,05 4,7 1,2 0,06 0,05
5	2-phenyl-2,5-bioxazole (***POO***)	cyclohexane ethanole ethanole+H_2SO_4 vapor, INDO/S	302 302 317 315	356 376 388 375	0,37 0,48 0,54 0,25	23,2 29,5 24,4 25,0	0,29 0,30 0,23 0,24	0,49 0,33 0,20 0,72	9,0 11,4 9,4 0,96	0,69 0,65 0,27 0,20	21,9 30,8 0,3 2,2	- 0,9 - -
6	2-(furyl-2)-2,5-bioxazole (***FOO***)	ethanole vapor, INDO/S	314 296	367 -	0,36 0,18	28,4 -	0,3 0,54	0,53 0,96	10,9 -	0,66 0,73	10 0,6	0,73 -
7	2-(thienyl-2)-2,5-bioxazole (***TOO***)	ethanole toluene vapor, INDO/S	320 320 308	- 410 -	0,17 0,17 0,08	-32,0 27,9 -	0,19 0,4 0,58	0,92 0,78 2,82	1,23 1,08 1,0	0,46 0,76 0,35	1,3 5,0 0,1	- 6,4 -
8	1,4-phenyl ene-2,2'-bis oxazole (***OPO***)	1,2,2'-TFTCE* cyclohexane toluene THF ethanole DMFA DMSA DiEG ethanole+H2SO4 vapor, INDO/S	306 308 311 311 309 312 325 313 310 311	340 344 352 350 350 354 368 356 420 345	0,93 0,60 0,49 0,61 0,71 0,81 0,45 0,85 0,61 0,71	42,2 34,6 37,7 35,9 42,8 35,4 38,2 34,8 38,2 40	0,93 0,60 0,49 0,76 0,65 0,73 0,41 0,86 0,28 0,69	0,07 0,40 0,51 0,49 0,27 0,17 0,50 0,16 0,18 0,28	1,63 1,33 1,46 1,38 1,65 1,36 1,47 1,34 1,47 1,06	2,08 1,38 1,18 1,81 1,51 1,80 1,08 2,09 0,83 1,06	644 83 36 50 95 93 15 18 0.2 32	≤0,1 0,38 - - 0,14 - 0,53 - - ≥0,3
9	2,5-furylene-2,2'-bis oxazole (***OFO***)	ethanole vapor, INDO/S	321 303	363 -	0,63 0,35	27,8 -	0,51 0,26	0,30 0,15	1,09 -	1,0 0,56	41,7 3,4	0,33 -

10	2,5-thienyl ene-2,2'-bis oxazole (***OTO***)	toluene ethanole DMFA ethanole+H2SO4 vapor, INDO/S	341 338 339 346 336	395 390 392 418 -	0.14 0.21 0.14 0.42 0.01	0,25 0,35 0,26 0,19 0,02	0,78 1,32 0,79 0,26 18,5	1,32 0,78 0,79 18,5 0,26	1,1 0,97 0,84 0,97 0,99	1,05 0,41 0,40 0,03 0,51	0,43 0,40 0,41 0,01 0,09	0,4 0,43 0,41 0,1 0,01
11	5-(para-aminophenyl)-2-phenyl-1,3-oxazole (***5-p-NH2-POP-1,3***)	toluene	329	388	0,58	32,4	0,48	0,35	1,25	0,34	10,3	-
12	2-(para-aminophenyl)-2-phenyl-1,3-oxazole (***2-p-NH2-POP-1,3***)	toluene	328	389	0,54	33,1	0,45	0,39	1,28	0,4	10,4	-
13	2-(orto-amino phenyl)-2-phenyl-1,3,4-oxadizole (***2-o-NH2-PDP-1,3,4***)	ethanole toluene	357 351	435 404	0.63 0,59	27,9 29,1	0,30 0,35	0,18 0,17	1,08 1,12	0,23 0,20	3,35 7,42	- -
14	2-(para-aminophenyl)-2-phenyl-1,3,4-oxa Dizole (***2-p-NH2-PDP-1,3,4***)	vapor, lamp toluene	304 349	355 380	0,24 0,68	25 27,5	0,34 0,55	0,40 0,26	0,96 1,06	0,4 2,9	3,1 23,3	- -
15	2-(para-dimetyl aminophenyl)-2-phenyl-1,3,4-oxadia zol (***2-p-di-(CH3)2-PDP-1,3,4***)	ethanole DMFA	334 336	364 368	0,52 0,56	28,1 29,4	0,52 0,56	0,01 0,07	1,08 1,13	1,22 1,63	43,1 39,5	- -
16	2-di-(para-metoxi-phenyl)-2-phenyl-1,3,4-oxadizole (***2-di-p-OCH3-POP-1,3,4***)	ethanole laser, vapor	303 283	363 343	0,57 0,20	26,5 25,0	0,38 0,11	0,63 0,44	1,02 0,96	2,63 0,56	23,7 28,6	- -
17	2-di-(para-aminophenyl) phenyl-1,3,4-oxadiazol (***2-di-p-NH2-PDP-1,3,4***)	toluene ethanole DMFA	353 340 342	376 403 402	0,58 0,80 0,67	27,4 31,2 32,4	0,55 0,53 0,48	0,40 0,13 0,24	1,06 1,20 1.25	3,94 2,4 2,94	59,3 52,0 41,9	- - -
18	2-di-(para- metoxi-phenyl) phenyl-1,3,4-oxadiazol (***2-di-p-OCH3-PDP-1,3,4***)	laser, vapor ethanole ethanole+H2SO4	281 316 370	330 357 426	0,17 0,57 0,23	25 28,4 24,2	0,08 0,38 0,10	0,40 0,29 0,34	0,96 1,10 0,94	0,52 2,55 0,51	1,9 32,4 5,7	- - -
19	2-di-(orto-oxiphenyl) phenyl-1,3,4-oxadiazol (***2-di-o-OH-PDP-1,3,4***)	ethanole ethanole+KOH	341 364	397 449	0,49 0,15	27,7 24,3	0,27 0,07	0,28 0,38	1,07 0,94	1,2 0,11	3,5 0,13	- -
20	2-di-(orto-amino phenyl) phenyl-1,3,4-oxadiazol (***2-di-o-NH2-PDP-1,3,4-***)	ethanole	369	406	0,51	25,6	0,34	0,33	0,99	0,37	3,97	-
21	2-phenyl-1,3-benzoxazole (***2PbO***)	laser, vapor cyclohexane	298 300	312 328	0,24 0,78	25 26,9	0,1 0,43	0,90 0,12	0,96 1,04	0,04 0,14	0,07 9,73	- -
22	2-(orto-aminophenyl)-1,3-benz oxazole (***2-o-NH2-PbO***)	toluene	324	348	0,58	27,1	0,36	0,26	1,04	0,22	5,31	-
23	paraquater-phenyle **(*PPPP*)**	ethanole	298	367	37,9	1,46	0,91	0,83	0,008	3,22	87,4	0,51
24	2,5-phenyl-5-(4-bi phenylyl) **-1,3,4-oxa diazole (***PDPP***)**	ethanole	305	376	39	0,88	0,88	0,12	1,5	2,88	68.4	1,87
25	2,5-di-biphenyl-1,3,4-oxa diazole (***PPOPP***)	ethanole	340	409	51,2	0,89	0,75	0,92	1,97	2,24	73,1	0,45
26	2(phenylbenz-1,3-oxazolyle-2)benzole (***BboPobB***)	laser, vapor highlydense vapor, laser chloroforms toluene	318 337 341 373	- 393 (377; 397; 417) (373; 393,5; 446,5)	0,65 0,6 0,9 0,9	53,3 50,0 53,3 50	0,54 0,66 0,64 0,64	0,29 0,45 0,07 0,07	2,1 1,5 2,1 1,9	1,63 1,46 2,19 1,46	37,5 97,5 98,1 91,7	0,25 (0.1-0.58) 0,8 0,9

27	1,4-di-(5-phenyl oxazolyl-2) benzole (***POPOP***)	toluene ethanole ethanole+H2SO4 Highlydense vapor vapor, laser(266 nm) INDO/S	366 360 373 324 324 319	418 422 508 383 392 379	0,86 0,97 0,93 0,80 0,06 0,80	52,3 54,5 39,3 70,0 66,8 -	0,72 0,60 0,43 0,86 0,07 0,96	0,12 0,04 0,09 0,22 1,04 0,22	20,1 21,0 15,0 26,8 27,0 27,8	3,72 2,26 1,39 2,83 0,53 2,79	68,7 96,4 0,1 43,0 4,0 39,2	(2,34) (2,2) -
28	2-[(5-phenyl oxazolyl-2)-5-(5-phenylyl - 2)]benzole (***POPDP***)	toluene ethanole	351 318	412 378	51,9 53	0,93 0,8	0,69 0,89	0,05 0,22	2,0 2,04	1,94 2,17	68,9 55,1	2,25 2,63
29	1,5-phenyl oxazolyl-2-4-[5-(furyl-2)-1,3,4-oxa diazolyl-2] benzole (*POPDF*)	ethanole toluene dioxane DMFA ethanole+H2SO4 vapor, INDO/S	351 352 352 353 356 318	440 434 414 464 528 398	46,7 44,2 50,8 53,8 38,7 50	0,9 0,91 0,52 0,37 0,67 0,8	0,69 0,7 0,41 0,23 0,3 0,73	0,08 0,07 0,38 0,39 0,15 0,18	1,8 1,9 1,95 2,07 1,49 1,93	2,61 2,48 2,11 2,72 1,22 1,15	36,3 49,6 73,5 41,3 0,13 10,1	2,3 2,2 1,83 2,35 - -
30	1,4-di-5-(furyl-2)-1,3,4-oxa diazolyl-2) benzole (***FDPDF***)	toluole ethanole	353 353	434 460	44,2 53,8	0,86 0,37	0,69 0,23	0,11 0,15	1,7 2,07	2,02 1,87	74,6 87,2	2,2 2,3
31	1,5-phenyl oxazolyl-2-4-[5-(thienyl-2)-1,3,4-oxa diazolyl-2] benzole (***POPDT***)	toluole ethanole	335 336	422 422	47,62 42	0,66 0,78	0,57 0,5	0,3 0,11	1,83 1,62	1,53 1,60	35,6 31,9	2,6 2,9
32	2,5-di-(5-phenyl-oxazolyl-2) thiophen (***POTOP***)	toluole ethanol THF DMFA ethanole+H2SO4 vapor, INDO/S	390 386 389 390 405 350	468 458 457 436 512 -	48,2 42,4 41,5 43,9 44,7 45,0	0,36 0,40 0,48 0,33 0,72 0,30	0,40 0,42 0,49 0,35 0,32 0,33	0,70 0,63 5,53 0,70 0,13 0,78	1,85 1,63 1,6 1,69 1,72 1,73	1,30 1,46 1,25 1,59 1,51 1,32	2,9 3,0 3,1 2,8 1,0 0,06	4,8 4,53 4,45 4,22 - -
33	2-(5-phenyl oxazolil-2)-5-[5-phenyl-1,3,4-oxa diazolyl-2] **thiophen** (*POTDP*)	toluole ethanole ethanole+H2SO4 vapor, INDO/S	373 379 401 341	452 452 522 411	43 43,1 41,3 40	0,39 0,45 0,72 0,3	0,43 0,47 0,32 0,33	0,68 0,57 0,12 0,78	1,62 1,66 1,59 1,73	1,82 1,28 2,5 1,27	6,1 2,7 0,13 0,16	4,8 4,43 - -
34	2-(5-phenyl-oxazolil-2-5-[5-(thienyl-2)-1,3,4-oxa diazolyl-2] thiophen (*POTDT*)	ethanole toluole	378 375	460 456	49,6 44,7	0,38 0,47	0,42 0,41	0,68 0,22	1,91 1,72	1,42 1,54	4,34 3,96	5,2 5,3

Notes. Solvents: 1,2,2'-TFTCE is 1,1,2,2'-trifluorotrichloroethanol; THF is tetrahydrofuran; DMFA is dimethylformamide; DMSO is dimethylsulfoxide; DiEG is diethylenglycol; ethanole+H2SO4 is solution of H2SO4 in ethanol with pH ≈ 2,0; vapor, INDO/S is characteristics of the "free states" of the molecule by calculations by the LCAO-MO SCF extended-CI INDO/S methods; $\lambda_{abs}^{\max}$, $\lambda_{fl}^{\max}$ and $\lambda_{gen}^{\max}$ are wavelength of the maxima in the absorption, Fl and GRl spectrums; $\varepsilon_{abs}^{\max}(\nu)$ is the molar's coefficient of extinction the absorption spectra; γ_{fl} is the QYFl, k_{fl} and k_{ST} is the RC Fl and RC ItCC; $\sigma_{13}^{abs}(\nu)$ and $\sigma_{31}^{osc}(\nu)$ are the cross section for of the laser pump-pulse of the absorption spectra and for stimulated emission in the maxima of the wavelengths wide bands in the absorptions and fluorescence (298K) spectrums; E_{lp} is the threshold density of energy absorbed of a single of the laser pump-pulse and average density of power, P_{lp}, at the frequency of following of pulses for F_{exit} ≈ 30 Gz; t_{lp} is the limit of a single the laser pump-pulse at which occurrence the generated radiation of light is possible; vapor, laser are experimental characteristic molecules of vapors [1, 34 - 37].

For the compounds if values the cross sections $\sigma_{24}^{*}(\nu^{osc})$ and the cross sections $\sigma_{31}^{osc}(\nu)$ and $\sigma_{24}^{*}(\nu^{osc})$ but to the time t_{lp} up tends to about 100 ns are comparable, and GRl because t_{lp} = 10^{-11} - 10^{-12} s is impossible in Fig. 4.

The increase in the steepness the limit front time of pump-pulse, t_{lp} should lower the lasing threshold, which should tend to the minimal possible of value.

Since the magnitude of losses related to the triplet-triplet reabsorption spectra is increases in time, the limit of the dye-laser pulse is always shorter than the excitation of pumping ($\Delta\tau_{osc} < \Delta\tau_{exit}$) in Table 4.

The Spectrum Fluorescence and Losses at the Pump Electrons

The probability of emission $W_{fl}(E)$ is characterized by value of the ElQYFl (γ_{fl}^{e}), and also function of excitation which is proportional to total dependence on the energy of electrons and the sections of excitation $\sigma_{i}^{exit}(E)$ of all the STElExSt according to

expression

$$W_{fl}(E) = (j/e)n_0\, h\nu \sum_i \gamma_{fl}^{e}\sigma_i^{exit}(E), \quad (9)$$

where j is density of the current, e is charge of electrons, n_0 is concentration of molecules and $h\nu$ is the quant of light (or Fl). [4, 12]

Average on ensemble of compounds the values of the absorbed energy $\bar{E}_n$ and QYFl $\bar{\gamma}_{fl}$ will be defined ratio [12]

$$\bar{E}_n = \frac{\int \sigma_i^{exit}(E_{exit})E_{exit}dE_{exit}}{\int \sigma_i^{exit}(E_{exit})dE_{exit}} \quad (10)$$

and

$$\bar{\gamma}_{fl} = \frac{\int \sigma_i^{exit}(E_{exit})\gamma_{fl}^{e}(E_{exit})dE_{exit}}{\int \sigma_i^{exit}(E_{exit})dE_{exit}} \quad (11)$$

Therefore the energy-QYFl (γ_{fl}^{e}) at the electron excited of compounds by formula [4]

$$\gamma_{fl}^{e} = \frac{\bar{E}_{fl}\int \sigma_i^{exit}(E_{exit})\gamma_{fl}(E_{exit})dE_{exit}}{\int \sigma_i^{exit}(E_{exit})E_{exit}dE_{exit}}, \quad (12)$$

where $\bar{E}_{fl}$ is average value of energy of the QYFl.

At the electric excitation of values EnQYFl it is appreciable less, than QYFl at optical excitation.

The Efficiency of Fluorescence Spectra and OLEDs

The power efficiency of the OLEDs-device with the standard diagram of the orientation of radiation is function of enclosed voltage U_{entr} and efficiency on the current γ_{cur} . The OLEDs-devices have the working voltage 5 - 8 - 14 V, and also can be reduced up to 3 - 4 V (29 lum/W) at brightness 500 - 1000 kd/m^2. For solid-state of OLEDs-diodes γ_{LED} ice makes 80 lm/W (at the current 20 mlA sometimes up to 150 lm/W). [11]

The value γ_{LED} is calculated by formula

$$\gamma_{LED} = \gamma_{cur}\left(\pi/U_{entr}\right). \quad (13)$$

In view of what efficiency on the current (γ_{cur}) is defined by expression as

$$\gamma_{cur} = k\pi\gamma_{\text{int}}\gamma_{exit}, \quad \gamma_{LED} = k\pi\gamma_{\text{int}}\gamma_{exit}\left(1/U_{entr}\right), \quad (14)$$

where k is constant determined by function of photosensivity of the human eye.

Best samples of the OLEDs-device have efficiency on current γ_{cur} = (2 - 10) and sometimes 40 kd/A. [11]

The external quantum efficiencies γ_{int}, i.e. losses on internal reflection in interfaces between the organic layers can achieve up to 80 %.

The external quantum efficiency (EQYFl) for OLEDs-diode γ_{exit} makes

$$\gamma_{exit} = 1 - \left[\sqrt{1-\left(1/n_r^2\right)}\right], \quad (15)$$

where n_r is parameter of refraction of active layer OLEDs and at n_r = 1,49 value $\gamma_{exit} \le 26$ %, at n_r = 1,7 value $\gamma_{exit} \le 20$ %, and at n_r = 2 value the makes size $\gamma_{exit} \le 13{,}4$ %. [4]

Reception of the intensives of luminescence with the given coordinates of chromaticity speaks the opportunity of thin selection STElExSt of materials in the OLEDs-device. [5,11]

In strong fields at intensity of the electric field between electrodes makes 10^6-10^7 A/cm^2 and process the electronic results to the auto-electronic emission issue and the amplification of electrons up to the energy, causing of the ElExEn and the photoionization. [11]

Thus, the power properties of any the optic-electronics device are defined by active the compounds or related the QYFl (γ_{fl}^{i}) and QYPh (γ_{ph}^{i}) by environments for which not only it is necessary to have the full set of the spectral-fluorescence characteristics, but also it is necessary to carry out authentic interpretations.

Conclusion

The spectral-luminescence by now spectral-calculations of technological methods is offered. The method which allows to establish the spectroscopic characteristics of compounds in the GrSt (S_0) and in the full spectra singlet and triplet STElExSt in different environments and also put into practice: 1) at different parameters of impulse-pumping to define required the spectral-power properties, and the energy-quantum efficiently, and also the energy of contribution for dye-lasers; 2) the fine structure of Raman scattering, and also of NMR-, IR- and UV-absorption, and Fl- and Ph-spectrums; 3) variations of the coefficient is the molyare extinctions, and of refraction or dispersion in vapor, solvent, and moleculare crystals; 4) the absolute and relative of QYFl and the QYPh; 5) the parameters GRl in the dye-lasers; 6) the photo-stability and service life of dye.

REFERENCES

[1]A. E. Obukhov, Laser Physics, **7** (5), 1102 (1997).

http://www.lasphys.com/lasphys/submission-system

[2]*Specroscopy of Ground and Excited States of the Multiatomic Molecules in Variation of Condisions*, edited by A. E. Obukhov, ("Sputnik+", Russia, Moscow, 2010). ББК 22.344. O-26. ISBN 978-5-9973-0657-1.

[3]A. E. Obukhov, Laser Physics, **6**, 890 (1996).

[4]A. E. Obukhov, Proceedings of SPIE. Material Development for Organic Electronics and Photonics, 2012 Photonics Europe, Brussels, Belgium, **8435**, 84351J-1 (2012).

[5]A. E. Obukhov, Sov. J. Quantum. Electronics, **20**, 863 (1993).

[6]Card file JCPDS "Joint Commitee for Powder Diffraction Studies" - ICDD "International Centre for Diffraction Data" (1997).

[7]D. H. Christensen, J. T. Nielsen and O. F. Nielsen, J. of Molecular Spectroscopy, **24**, Issue 1-4, 225 (1967). http://dx.doi.org/10.1016/0022-2852 (67)90084-7

[8]*Modern Spectroscopy*, edited by J. Michael Hollas. (Jon Willey & Sons: West Sussex, England, 2004).

[9]G. A. Abakumov, B. I. Polyakov, A. P. Simonov, at al., Applied Physics B., **27 B**, Issue 1, 57 (1982). http://link.springer.com/article/10.1007/BF00697297.

[10]P. P. Sorokin, J. R., Lancard, E. C. Hammond, and V. L. Moruzzi, IBM J. Res. and Develop, **11**, 130 (1967).

[11]*Organic Electroluminescense*, edited by Kafafi Zakia (Taylor& Francis Group. LLC. New-York, London, 2005).

[12]A. Kazakov, A. Kukhta, and V. Suchkov, J. of Fluorescence, **10 (4)**, 409 (2000).

Alexandr Evgenievich Obukhov the date of birth is 29.10.1953 in Moscow. He graduated from Moscow Power Engineering Institute from 1970 to 1976, and he became a specialist in the field of mechanics engineering aviation devices. He graduated from Belorussian States University from 1989 to 1992, and a receive Ph.D. degree of the candidate of physical and mathematical sciences. In 1996 is lector of Physics in Moscow Mining State University, and also in 2010 senior scientist of Bauman Technical State University. Today A. E. Obukhov work of senior scientist in Moscow Power Engineering Institute "MPEI". In 2012 achieve degree doctor of the physic and mathematic science. A. E. Obukhov published more than 100 Journal papers and one book "Spectroscopy of the Ground and Excited Electronic States of the Multiatomic Molecules in Variation of Condisions". He scientific interests: X-, E-, N-Ray and NMR-spectroscopy, Spatial and electronic structure of multiatomic compounds, Photophysics, Photochemistry and Photobiology, and the Nonlinear phenomena and the innermoleculare quantum mechanisms of the multistips transitions in the full spectrum of the singlets and triplets electronic excited states on the Dye-lasers, OLEDs, OTETs, IR-, SCR-, UV-absorptions, Raman scattering, Fluorescence and Phosphorescence, Emissions and Generation radiated of light, Photochemistry, Photobiology, Chemical reactions, Nanocurrent, and Nanotechnology, and other science.

An Exact Solution for the Free Vibration Analysis of Timoshenko Beams

Ramazan A. Jafari-Talookolaei*[1], Maryam Abedi[2]

School of Mechanical Engineering, Babol Noshirvani University of Technology, 47148 – 71167, Babol, Mazandaran Province, Iran

*[1]ramazanali@gmail.com, [2]maryamabedy2000@yahoo.com

Received 27 May 2013; Accepted 18 June 2013; Published 13 March 2014

Abstract

This work presents a new approach to find the exact solutions for the free vibration analysis of a beam based on the Timoshenko type with different boundary conditions. The solutions are obtained by the method of Lagrange multipliers in which the free vibration problem is posed as a constrained variational problem. The Legendre orthogonal polynomials are used as the beam eigenfunctions. Natural frequencies and mode shapes of various Timoshenko beams are presented to demonstrate the efficiency of the methodology.

Keywords

Timoshenko Beam; Natural Frequencies; Mode Shapes; Legendre Polynomials; Lagrange Multipliers

Introduction

Beams play an important role in the creation of mechanical, electromechanical, and civil systems. Many of these systems are subjected to dynamic excitation. As a consequence, the exact determination of the natural frequencies and mode shapes of linear elastic beams have been studied by many researchers. It has been known for many years that the classical Euler-Bernoulli beam theory is able to predict the frequencies of flexural vibration of the lower modes of thin beams with adequate precision. The vibratory motion of thick beams is described by the Timoshenko beam theory, as they incorporate the effects of rotary inertia and deformation due to shear. During the past decades, the free vibrations of Euler–Bernoulli beams have received considerable attention of many researchers, but only few publications were devoted to including the effects of shear deformation and rotary inertia.

The mode shape differential equation describing the transverse vibrations of a hanging Euler–Bernoulli beam under linearly varying axial force has been derived by Schafer (1985). Lee and Ng (1994) have computed the fundamental frequencies and the critical buckling loads of simply supported beams with stepped variation in thickness using two algorithms based on the Rayleigh-Ritz method. The first algorithm which has been used extensively in analyzing beams with non-uniform thickness, involves using a series of assumed functions that satisfy only the external boundary conditions and disregard the presence of the step. The second algorithm considers a beam with a step as two separate beams divided by the step. Two different sets of admissible functions which satisfy the respective geometric boundary conditions have been assumed for these two fictitious sub-beams. Geometric continuities at the step have been enforced by introducing artificial linear and torsional springs.

Lee and Kes (1990) have conducted a study to determine the natural frequencies of non-uniform Euler beams resting on a non-uniform foundation with general elastic end restraints. The free vibration response of an Euler-Bernoulli beam supported by an intermediate elastic constraint has been studied by Riedel and Tan (1998) using the transfer function method. Rosa and Maurizi (1998) have investigated the influence of concentrated masses and Pasternak soil on free vibration of beams and gave exact solutions for Bernoulli–Euler beams based on the beam theory. A modified finite difference method has been presented by Chen and Zhao (2005) to simulate transverse vibrations of an axially moving string.

Lin and Tsai (2007) have determined the natural frequencies and mode shapes of Bernoulli–Euler

multi-span beam carrying multiple spring-mass systems. An analytical solution has been presented for the natural frequencies, mode shapes and orthogonality conditions of an arbitrary system of Euler–Bernoulli beams interconnected by arbitrary joints and subject to arbitrary boundary conditions by Wiedemann (2007). Failla and Santini (2008) have addressed the eigenvalue problem of the Euler–Bernoulli discontinuous beams. A simulation method called the differential transform method (DTM) has been employed to predict the vibration of an Euler–Bernoulli beam (pipeline) resting on an elastic soil by Balkaya and Kaya (2009). Alim and Akkurt (2011) have investigated the free vibration analysis of straight and circular beams on elastic foundation based on the Timoshenko beam theory. Ordinary differential equations in scalar form obtained in the Laplace domain are solved numerically using the complementary functions method.

He and Huang (1987) have used the dynamic stiffness method to analyze the free vibration of continuous Timoshenko beam. The full development and analysis of four models for the transversely vibrating uniform beam have been presented by Han et al. (1999). The four theories namely the Euler-Bernoulli, Rayleigh, shear and Timoshenko have been considered. Zhou (2001) has studied the free vibration of multi-span Timoshenko beams by the Rayleigh-Ritz method. The static Timoshenko beam functions have been developed as the trial functions in the analysis which are the complete solutions of transverse deflections and rotational angles of the beam when a series of static sinusoidal loads acts on the beam.

A study of the free vibration of Timoshenko beams has been presented by Lee and Schultz (2004) on the basis of the Chebyshev pseudospectral method. Chen et al. (2004) have proposed a mixed method, which combines the state space method and the differential quadrature method, for bending and free vibration of arbitrarily thick beams resting on a Pasternak elastic foundation. The Laplace transform has been used to obtain a solution for a Timoshenko beam on an elastic foundation with several combinations of discrete in-span attachments and with several combinations of attachments at the boundaries by Magrab (2007).

In the present paper, a novel approach is made to the problem of the free vibrations of a Timoshenko beam, in which the orthogonal Legendre polynomials in conjunction with Lagrange multipliers are used. The frequencies and the corresponding mode shapes for common types of boundary conditions are compared extremely well with the available solution.

Problem Formulation

Consider a straight Timoshenko beam of length *L*, a uniform cross-sectional area *A(=b×h)*, the mass per unit length of *m*, the second moment of area of the cross-section *I*, Young's modulus *E*, and shear modulus *G*. It is assumed that the beam is made of a homogenous and isotropic material.

The kinetic energy T and the strain energy U of the vibrating beam can be written as:

$$T = \frac{1}{2}\int_0^L \left\{ m w_{,t}^{\ 2} + m r^2 \psi_{,t}^{\ 2} \right\} d\hat{x} \quad (1)$$

$$U = \frac{1}{2}\int_o^L \left\{ M\psi_{,\hat{x}} + V\gamma \right\} d\hat{x} = \frac{1}{2}\int_0^L \left\{ EI\psi_{,x}^{\ 2} + kAG\gamma^2 \right\} dx \quad (2)$$

Where γ represents the shear angle ($\gamma = w_{,\hat{x}} - \psi$), $w(\hat{x},t)$ and $\psi(\hat{x},t)$ are transverse displacement and the cross-section rotation due to the bending moment, $\hat{x}$ is the axial coordinate of the beam, r is the radius of gyration ($=\sqrt{I/A}$) and k is the beam cross sectional shape factor. Also M and V are the bending moment and shear forces, respectively. Comma denotes differentiation with respect to $\hat{x}$ or t.

Applying Hamilton's principle, the governing equations of motion and boundary conditions are obtained as follows:

$$m w_{,tt} - (kAG(w_{,\hat{x}} - \psi))_{,x} = 0 \quad (3)$$

$$m r^2 \psi_{,tt} - kAG(w_{,\hat{x}} - \psi) - (EI\psi_{,x})_{,x} = 0 \quad (4)$$

$$(M\delta\psi)_0^L = 0,\ (V\delta w)_0^L = 0 \quad (5)$$

in other words, at the ends $\hat{x}$=0 and L, we have:

$$\begin{cases} \text{either } M = 0 \text{ or } \psi = 0 \text{ is specified,} \\ \text{either } V = 0 \text{ or } w = 0 \text{ is specified.} \end{cases} \quad (6)$$

The equation (6) gives the boundary conditions of the present case.

Analytical Solution

In the present work, series of solutions in conjunction with the Lagrange multipliers are used to study the free vibration characteristics of the beam. The main advantage of the Lagrange multiplier technique is that the choice of the assumed displacement function is easy because they do not have to satisfy the boundary conditions of the problem. In the present study, the simple Legendre polynomials are chosen as displacement functions, and this simplifies the problem further since the orthogonality properties

lead to simple energy expression.

Harmonic solutions for the variables $w(\hat{x},t)$ and $\psi(\hat{x},t)$ are assumed as:

$$w(\hat{x},\hat{t}) = W(x)e^{i\omega t}, \quad \psi(x,t) = \Psi(x)e^{i\omega t} \tag{7}$$

in which variables $W(\hat{x})$ and $\Psi(\hat{x})$ are the displacement functions and ω is the circular frequency. As mentioned above, the displacement functions can be expressed in terms of the simple Legendre polynomials and are given by:

$$W(x) = \sum_{m=0}^{n_t} W_m P_m(x), \quad \Psi(x) = \sum_{m=0}^{n_t} \Psi_m P_m(x) \tag{8}$$

Here, Pm is the simple Legendre polynomial of degree m. It should be mentioned that the axial coordinate is transformed to the interval $-1 \le x \le 1$ by letting $x = \dfrac{\hat{x} - L/2}{L/2}$.

We have four boundary conditions for each beam, i.e. two boundary conditions for two ends. These four boundary conditions which are not satisfied by the assumed series, are imposed as constraints. For four common boundary conditions (B.C.s), these constraints can be written as follows:

Clamped-Clamped Beam (C-C):

$$\begin{aligned} &W(-1) = 0, \quad \Psi(-1) = 0 \\ &W(1) = 0, \quad \Psi(1) = 0 \end{aligned} \tag{9a}$$

Clamped-Hinged Beam (C-H):

$$\begin{aligned} &W(-1) = 0, \quad \Psi(-1) = 0 \\ &W(1) = 0, \quad \Psi'(1) = 0 \end{aligned} \tag{9b}$$

Hinged-Hinged Beam (H-H):

$$\begin{aligned} &W(-1) = 0, \quad \Psi'(-1) = 0 \\ &W(1) = 0, \quad \Psi'(1) = 0 \end{aligned} \tag{9c}$$

Clamped- Free Beam (C-F):

$$\begin{aligned} &W(-1) = 0, \quad \Psi(-1) = 0 \\ &\frac{2}{L}W'(1) - \Psi(1) = 0, \quad \Psi'(1) = 0 \end{aligned} \tag{9d}$$

in which prime denotes differentiation with respect to x. The boundary conditions yield linear constraints related to the linear combinations of the Legendre polynomials and subject to the degree of approximation, i.e. the number of polynomials involved. By substituting equations (8) in equation (9), the constraints can be rewritten as:

Clamped-Clamped Beam (C-C):

$$\begin{aligned} &\sum_{m=0}^{n_t} (-1)^m W_m = 0, \quad \sum_{m=0}^{n_t} (-1)^m \Psi_m = 0, \\ &\sum_{m=0}^{n_t} W_m = 0, \quad \sum_{m=0}^{n_t} \Psi_m = 0 \end{aligned} \tag{10a}$$

Clamped-Hinged Beam (C-H):

$$\begin{aligned} &\sum_{m=0}^{n_t} (-1)^m W_m = 0, \quad \sum_{m=0}^{n_t} (-1)^m \Psi_m = 0 \\ &\sum_{m=0}^{n_t} W_m = 0, \quad \sum_{m=1}^{n_t} \Psi_m \sum_{k_1=0}^{\left\lfloor \frac{m-1}{2} \right\rfloor} (2m - 4k_1 - 1) = 0 \end{aligned} \tag{10b}$$

Hinged-Hinged Beam (H-H):

$$\begin{aligned} &\sum_{m=0}^{n_t} (-1)^m W_m = 0, \sum_{m=1}^{n_t} \Psi_m \sum_{k_1=0}^{\left\lfloor \frac{m-1}{2} \right\rfloor} (-1)^{m-2k_1-1} (2m - 4k_1 - 1) = 0 \\ &\sum_{m=0}^{n_t} W_m = 0, \quad \sum_{m=1}^{n_t} \Psi_m \sum_{k_1=0}^{\left\lfloor \frac{m-1}{2} \right\rfloor} (2m - 4k_1 - 1) = 0 \end{aligned} \tag{10c}$$

Clamped- Free Beam (C-F):

$$\begin{aligned} &\sum_{m=0}^{n_t} (-1)^m W_m = 0, \quad \sum_{m=0}^{n_t} (-1)^m \Psi_m = 0 \\ &\frac{2}{L} \sum_{m=1}^{n_t} W_m \sum_{k_1=0}^{\left\lfloor \frac{m-1}{2} \right\rfloor} (2m - 4k_1 - 1) - \sum_{m=0}^{n_t} \Psi_m = 0 \\ &\sum_{m=1}^{n_t} \Psi_m \sum_{k_1=0}^{\left\lfloor \frac{m-1}{2} \right\rfloor} (2m - 4k_1 - 1) = 0 \end{aligned} \tag{10d}$$

In above equation, we have used the following properties of Legendre polynomial (Gradshteyn and Ryzhik, 2007):

$$P_n'(x) = \sum_{k=0}^{\left\lfloor \frac{n-1}{2} \right\rfloor} (2n - 4k - 1) P_{n-2k-1}(x) \qquad (n \ge 1)$$

in which $\left\lfloor \dfrac{n-1}{2} \right\rfloor$ signifies the integral part of *(n-1)/2* (Gradshteyn and Ryzhik, 2007).

A variational principle is formulated based on the kinetic and strain energies by a procedure similar to one followed by Washizu (1982). This variational principle along with the constraint conditions is used to solve the vibration problem. The function to be extremized is given by the expression:

$$F = U + T - \sum_{i=1}^{4} \alpha_i (\text{constraints equation}) \tag{11}$$

where α_i $(i = 1-4)$ are the Lagrange multipliers. Substituting the assumed series for $W(x)$an d$\Psi(x)$ in equation (11) and simplifying yields:

$$F=\frac{EI}{L}\int_{-1}^{1}\sum_{m=1}^{n_t}\Psi_m\sum_{k_1=0}^{\left\lfloor\frac{m-1}{2}\right\rfloor}(2m-4k_1-1)P_{m-2k_1-1}(x)\sum_{n=1}^{n_t}\Psi_n\sum_{k_2=0}^{\left\lfloor\frac{n-1}{2}\right\rfloor}(2n-4k_2-1)P_{n-2k_2-1}(x)dx$$
$$+\frac{kAGL}{4}\sum_{m=0}^{n_t}\frac{2}{2m+1}{\Psi_m}^2$$
$$+\frac{kAG}{L}\int_{-1}^{1}\sum_{m=1}^{n_t}W_m\sum_{k_1=0}^{\left\lfloor\frac{m-1}{2}\right\rfloor}(2m-4k_1-1)P_{m-2k_1-1}(x)\sum_{n=1}^{n_t}W_n\sum_{k_2=0}^{\left\lfloor\frac{k-1}{2}\right\rfloor}(2n-4k_2-1)P_{n-2k_2-1}(x)dx$$
$$-kAG\int_{-1}^{1}\sum_{m=0}^{n_t}\Psi_m P_m(x)\sum_{n=1}^{n_t}W_n\sum_{k_1=0}^{\left\lfloor\frac{n-1}{2}\right\rfloor}(2n-4k_1-1)P_{n-2k_1-1}(x)dx$$
$$-\frac{m\omega^2L}{4}\sum_{m=0}^{n_t}\frac{2}{2m+1}\left({W_m}^2+r^2{\Psi_m}^2\right)-\sum_{i=1}^{4}\alpha_i(\text{constraints equation}) \quad (12)$$

The necessary extremizing conditions are given by:

$$\frac{\partial F}{\partial W_m}=\frac{\partial F}{\partial \Psi_m}=0,\quad m=0,1,2,... \quad (13)$$

Using equation (13) in conjunction with equation (12) results in a system of linear algebraic equations which, in matrix form, can be written as:

$$\underline{\underline{A}}\left\{W_0,W_1,...,W_{n_t},\Psi_0,\Psi_1,...,\Psi_{n_t}\right\}^T=\underline{\underline{B}} \quad (14)$$

in which the right hand side of equation (14) consists of Lagrange multipliers. Solving equation (14) for W_m and Ψ_m $(m=1,2,...,n_t)$ and substituting into the constraint equations (10) results in a system of homogenous linear algebraic equations with the Lagrange multipliers as unknowns. The system of equations is given by:

$$\underline{\underline{C}}\left\{\alpha_1,\alpha_2,\alpha_3,\alpha_4\right\}^T=\underline{0} \quad (15)$$

The natural frequencies and corresponding mode shapes of beams can be calculated using equations (14) and (15). In calculating the natural frequency, the determinant of the coefficient matrix in equation (15) is computed for various values of frequency starting from a near zero value. Determinant change of sign function is identified and the corresponding value of frequency is the natural frequency of the beam in question.

Results and Discussion

In order to demonstrate the high accuracy of the present method, the convergence and comparison studies are carried out. Unless mentioned otherwise, in all of the following analysis the rectangular cross-sectional beams with shear correction factor k=5/6 and the Poisson ratio υ=0.3 are considered. The first five dimensionless frequencies ($\Omega=\sqrt{\frac{mL^4}{EI\pi^4}}\omega$) of hinged-hinged (H-H) and clamped-clamped (C-C) beams are given in Table 1. The number of terms of the Legendre polynomial steadily increases from 6 to 10. One can see that the convergence is very rapid. In general, 10 terms of the Legendre polynomial are enough to give satisfactory results.

TABLE 1 THE CONVERGENCE STUDY ON THE FIRST FIVE DIMENSIONLESS FREQUENCIES OF H-H AND C-C TIMOSHENKO BEAMS FOR (L/H=10)

B.C.	n_t	Ω_1	Ω_2	Ω_3	Ω_4	Ω_5
H-H	6	2.1251	5.4903	10.1815	21.8025	34.7663
	7	2.1251	5.4467	10.0291	15.8141	30.3098
	8	2.1251	5.4461	9.8518	15.4366	22.2419
	9	2.1251	5.4456	9.8425	14.9628	20.6510
	10	2.1251	5.4456	9.8425	14.9628	20.6507
C-C	6	0.9836	3.7670	8.1029	17.3346	37.0371
	7	0.9836	3.7588	7.9795	13.6489	26.0859
	8	0.9836	3.7588	7.9211	13.2646	20.2042
	9	0.9836	3.7588	7.9189	13.0420	18.8547
	10	0.9836	3.7588	7.9189	13.0419	18.8543

The comparison study has been given in Table 2 for the first five dimensionless frequencies of Timoshenko beams by using the present method, the dynamic stiffness method (DSM) (He and Huang, 1987) and static Timoshenko beam function (STBF) (Lee and Schultz, 2004). Three types of boundary conditions: H-H, C-H and CC have been considered. Excellent agreement has been observed for all cases, which shows that the present method has very high accuracy.

TABLE 2 THE COMPARISON STUDY OF THE FIRST FIVE DIMENSIONLESS FREQUENCIES OF H-H, C-H AND C-C TIMOSHENKO BEAMS FOR (L/H=6.667)

B.C.	Methods	Ω_1	Ω_2	Ω_3	Ω_4	Ω_5
H-H	Present	0.9644	3.5195	7.0424	11.0702	15.3445
	DSM	0.9644	3.5194	7.0424	11.0702	15.3444
	STBF	0.9644	3.5194	7.0424	11.0702	15.3444
C-H	Present	1.4387	4.1632	7.6625	11.5809	15.7282
	DSM	1.4386	4.1632	7.6625	11.5807	15.7273
	STBF	1.4386	4.1633	7.6626	11.5814	15.7293
C-C	Present	1.9814	4.7859	8.2462	12.0601	16.0888
	DSM	1.9814	4.7859	8.2461	12.0580	16.0887
	STBF	1.9814	4.7860	8.2462	12.0604	16.0889

Fig. 1 shows the effect of length-to-thickness ratio (L/h), where L varies while h keeps constant, on the dimensionless fundamental frequency of the beam with C-C, C–H, H-H and C-F boundary conditions. It

is clear that for the beam with L/h<30, the variation of L/h has drastic effect on Ω. While for higher values of L/h, the fundamental frequency tends to be constant, that is, the influence of L/h is practically negligible. As expected, the curve shows clearly that the smaller the length-to-thickness ratio is, the lower the frequency will be.

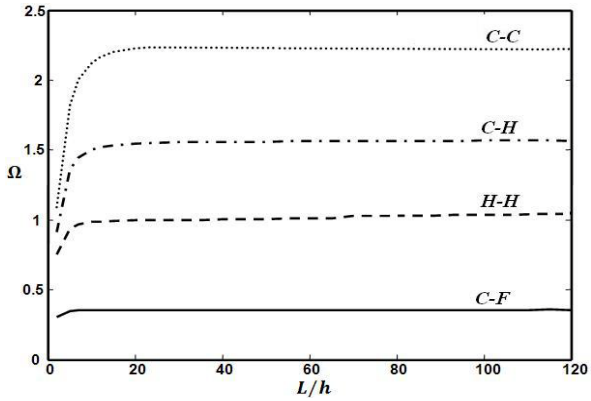

FIG. 1 EFFECT OF LENGTH-TO-THICKNESS RATIO ON THE DIMENSIONLESS FUNDAMENTAL NATURAL FREQUENCIES OF THE BEAM WITH VARIOUS BOUNDARY CONDITIONS

Fig. 2 shows the variation of the displacement Wand the bending slope Ψ along the beam length for the first three modes of vibration of Timoshenko beam with thickness ratio L/h=10 and C-C boundary condition.

Since the conventional beam theories can not involve the effect of Poisson's ratio, it is rather interesting to take a deep insight into it using the present approach. Table 3 gives the variation of the first three natural frequency parameters (Ω) of H-H beams with the Poisson's ratio. It is shown that the natural frequency decreases gradually with the increasing of Poisson's ratio. We can see that the natural frequencies for υ=0.5 have an apparent deviation from that for υ=0.1. From this point of view, the Poisson's ratio is of great significance in structural design especially for composite material beams.

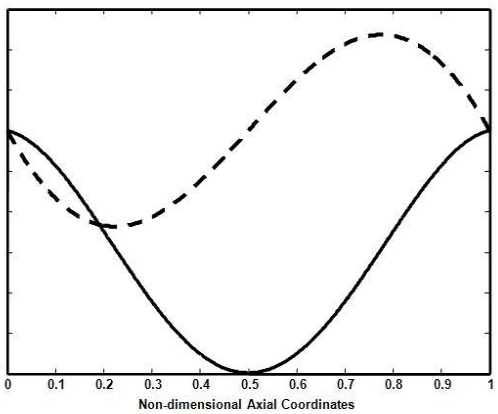

MODE 1

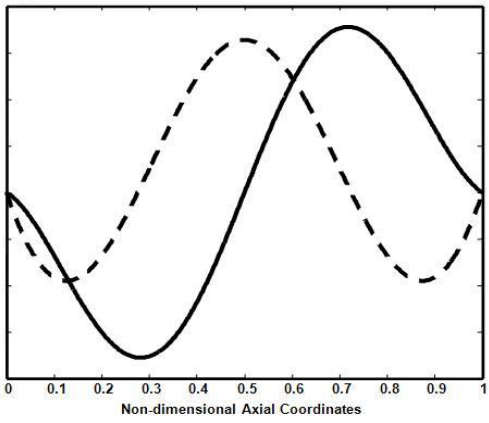

MODE 2

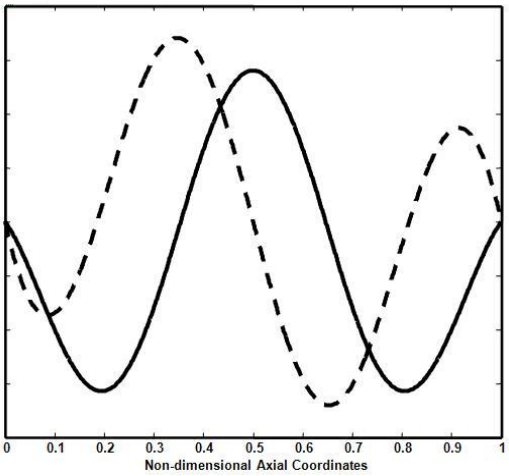

MODE 3

FIG. 2 VARIATION OF DISPLACEMENT AND THE BENDING SLOPE ALONG THE BEAM LENGTH (MODES 1-3)

W (——), Ψ(- - - -)

TABLE 3 EFFECT OF POISSON'S RATIOS ON THE FIRST THREE NATURAL FREQUENCY PARAMETERS (Ω) OF H-H BEAMS

L/h		Poisson's ratio (υ)				
		0.1	0.2	0.3	0.4	0.5
10	Ω_1	0.9854	0.9845	0.9836	0.9827	0.9817
	Ω_2	2.1948	2.1897	2.1821	2.1870	2.1818
	Ω_3	3.7844	3.7714	3.7586	3.7459	3.7334
25	Ω_1	0.9978	0.9977	0.9975	0.9974	0.9972
	Ω_2	3.9625	3.9600	3.9576	3.9551	3.9526
	Ω_3	8.8136	8.8017	8.7900	8.7782	8.7665

Conclusions

The free vibration of the Timoshenko beams is investigated using an assumed series solution in conjunction with Lagrange multipliers. It is observed that the present method is a computationally efficient

tool in predicting the natural frequencies of the beams. This method is particularly attractive because of the ease with which one can choose the generalized displacement functions. This fact is shown by choosing Legendre Polynomials whose orthogonal properties simplify energy expression considerably. The natural frequencies of the Timoshenko beam obtained by this method compare extremely well with the available exact solution. It should be mentioned that by applying this method, the convergence is very rapid.

REFERENCES

Alim, F.F., Akkurt, F.G., "Static and free vibration analysis of straight and circular beams on elastic foundation." Mechanics Research Communications 38 (2011): 89-94.

Balkaya Müge, Kaya Metin O. and Saˇglamer Ahmet, "Analysis of the vibration of an elastic beam supported on elastic soil using the differential transform method." Archive of Applied Mechanics 79(2009): 135–46.

Chen Li-Qun, and Zhao Wei-Jia, "A numerical method for simulating transverse vibrations of an axially moving string." Applied Mathematics and Computation 160 (2005): 411–22.

Chen W.Q., Lu C.F., Bian Z.G., "A mixed method for bending and free vibration of beams resting on a Pasternak elastic foundation." Applied Mathematical Modelling 28 (2004): 877–90.

Failla Giuseppe and Santini Adolfo, "A solution method for Euler–Bernoulli vibrating discontinuous beams." Mechanics Research Communications 35 (2008): 517–29.

Gradshteyn I.S. and Ryzhik I.M., Table of Integrals, Series, and Products, Seventh Edition, Elsevier Inc. 2007.

Han Seon M., Benaroya Haym and Wei Timothy, "Dynamics of Transversely Vibrating Beams Using Four Engineering Theories." Journal of Sound and Vibration 225 (1999): 935-88.

He Y.-S. and Huang T. C., 1987 Advanced Topics in Vibrations: presented at American Society of Mechanical Engineers Design Technology Conferences-11th Biennial Conference on Mechanical Vibration and Noise, 43-48, New York. Free Vibration analysis of continuous Timoshenko beams by dynamic stiffness method.

Lee H. P., and Ng T. Y., "Vibration and Buckling of a Stepped Beam." Applied Acoustics 42 (1994) 257-66.

Lee J. and Schultz W.W., "Eigenvalue analysis of Timoshenko beams and axisymmetric Mindlin plates by the pseudospectral method." Journal of Sound and Vibration 269 (2004): 609–21.

Lee S.Y., and Kes H.Y., "Free vibrations of non-uniform beams resting on non-uniform elastic foundation with general elastic end restraints." Comput. Struct. 34 (1990): 421–29.

Lin HY and Tsai YC, "Free vibration analysis of a uniform multi-span beam carrying multiple spring-mass systems." Journal of Sound and Vibration 302 (2007): 442–56.

Magrab Edward B., "Natural Frequencies and Mode Shapes of Timoshenko Beams with Attachments." Journal of Vibration and Control, 13(2007): 905-34.

Riedel C.H., and Tan C.A., "Dynamic Characteristics and Mode Localization of Elastically Constrained Axially Moving Strings and Beams." Journal of Sound and Vibration 215 (1998): 455-73.

Rosa M.A. De, and Maurizi M.J., "The influence of concentrated masses and Pasternak soil on the free vibrations of Euler beams-exact solution." Journal of Sound and Vibration 212 (1998): 573–81.

Schafer B., "Free vibrations of a gravity-loaded clamped-free beam." Ingenieur-Archiv 55 (1985): 66–80.

Washizu, K. 1982, Variational Methods in Elasticity and Plasticity, New York: Pergamon Press.

Wiedemann S.M., "Natural frequencies and mode shapes of arbitrary beam structures with arbitrary boundary conditions." Journal of Sound and Vibration 300 (2007): 280–91.

Zhou D., "Free Vibration of Multi-Span Timoshenko Beams Using Static Timoshenko Beam Functions." Journal of Sound and Vibration 241 (2001): 725-34.

Representations of the Temperature Correlation Effect in Lattice Calculations

Alain Hébert*[1]

Ecole Polytechnique de Montréal, P.O. Box 6079 station ``Centre-Ville", Montréal Qc. CANADA H3C 3A7

*[1]alain.hebert@polymtl.ca

Received 17 January 2014; Accepted 19 March 2014; Published 27 June 2014

Abstract

We are investigating the accuracy of various techniques for representing the temperature profile inside a fuel pin. The simplest approach consists in replacing the temperature profile by a single effective temperature. Here, we propose to treat explicitly the temperature gradient in fuel pins, using a subgroup self-shielding model together with various representations of the temperature correlation effect between different isotopes and fuel regions. We conclude that it is now possible to use an explicit representation of the temperature distribution in routine lattice calculations, without the introduction of an effective temperature.

Keywords

Lattice Calculation; Resonance Self-shielding; Doppler Effect; Computational Schemes

Introduction

Until recently, the recommended way to represent a temperature profile within the fuel pin was to replace this distribution with a uniform *effective* temperature, defined in such a way to preserve the integrated absorption rate within fuel (see de Kruijf and Janssen, 1996). This effective fuel temperature is an important parameter for the calculation of the Doppler effect and of the neutronic feedback during power transients. The effective fuel temperature is generally obtained as a weighted average of the temperatures in the fuel zones. Two simple theoretical expressions for this weighted averaged are proposed in the literature: the *chord-averaged* and the *volume-averaged* values. However, using such simple expressions has many drawbacks. These expressions are valid if the number density of the resonant isotope is almost constant in the fuel pin, which is only true for ^{238}U. In some cases, the effective temperature is found to be energy-dependent, a situation difficult to handle in many lattice codes. Finally, most effective temperature models are assuming a parabolic shape of the temperatures, a situation valid only under steady-state conditions. Modern lattice designs involve the introduction of different fuel pins with various isotopic contents, with or without burnable poisons. In some cases, the burnable poison is mixed with depleted fuel, leading to lower temperature pins. It is not always possible to find a unique effective temperature for all occurrences of a given isotope in the lattice, so that the accurate representation of temperature gradient effects in fuel cannot be avoided.

A more straightforward approach to represent a temperature profile is to divide the fuel into onion rings and to assign a different temperature to each of them. Most existing lattice codes cannot use this approach because of the strong correlation existing between different cross-section sets of a unique resonant isotope at different temperatures. Without special treatment, a lattice code assumes no correlation between the resonances in different cross-section sets, which is false for a unique resonant isotope at different temperatures.

However, using a modern self-shielding treatment based on the subgroup approach opens the way to the correct representation of these temperature correlation effects.

A first model for representing the temperature correlation effect was first implemented in the lattice code ECCO, dedicated to the study of fast reactor lattices (see Grimstone, Tullett and Rimpault, 1990). This model, implemented within the subgroup algorithm, is assuming a *full correlation* between different cross-section sets of a unique resonant isotope. Another full correlation model was also proposed by Perruchot (1996) in the context of the Sanchez-Coste method of the Apollo2 code. These

models are interesting as they can be used within coarse energy groups, such as those available in XMAS–172g and SHEM–281g. The full correlation model in the context of subgroup equations is also presented in Sect. II B of a technical paper by Hébert (2009).

Recently, we have proposed a new self-shielding method consistent with the introduction of a finer energy mesh, using as many as 295 energy groups (see Hébert, 2009). Using so many groups makes possible a simplification of the Ribon extended model, already presented by Hébert (2004), and the introduction of a new cross section correlation model with the capability to represent a temperature gradient in fuel. The same correlation model is also able to represent the *mutual shielding effect* between different resonant isotopes, although this effect is almost vanishing with a 295–group energy mesh. The proposed self-shielding method is referred as the *subgroup projection method* (SPM). The paper will describe the different correlation models, together with their implementation details.

Theory

The self-shielding calculations are kept apart from the main flux calculation, thanks to the Livolant-Jeanpierre factorization presented in Sect. 4.2.3 of *Applied Reactor Physics* (Hébert, 2009). Our study is based on two types of subgroup-based self-shielding methods. The first method, used with XMAS–172g and SHEM–281g meshes, is the Statistical slowing-down (ST) subgroup method, as introduced in Sect. 4.2.5 also of *Applied Reactor Physics*. It is based in *physical probability tables* where the table corresponding to the total cross section in an energy group is computed so as to match the numerical integration results with the tabulated values for specific values of the microscopic dilution cross section in this group.

The second method, used with SHEM–295g mesh, is the Subgroup Projection Method (SPM) introduced in Hébert's technical paper (2009). The original computing properties of the SPM can be summarized as follows:

1. The SPM is a subgroup approach based on CALENDF–type probability tables (see Hébert and Coste, 2002).
2. The self-shielding calculations are limited to energies above 4.63 eV. The SPM is used below 11.14 keV and the ST approach with physical probability tables is used above.
3. The new cross section correlation model can effectively represent both *mutual shielding effects* and *temperature gradient effects* in fuel, *without* introducing additional CPU costs other than those associated with the use of 151 energy groups.
4. Using as many as 151 energy groups between 4.63 eV and 11.14 keV, the s*uper-homogénéisation* (SPH) treatment of the self-shielded cross sections is not required. However, the SPH treatment is kept in the remaining groups with a lethargy width greater than 0.1.
5. The SPM can represent isotopic correlation effects in three different ways. A non-correlation approximation is first available in the case where resonances belonging to different isotopes are overlapping in a statistical way. A full-correlation model, similar to the model used in the ECCO lattice code, is available if different cross section sets are corresponding to the same isotope at different temperatures (see Grimstone, Tullett and Rimpault, 1990). Finally, a general correlation model is available with the capability to represent any level of correlation, from no correlation to full correlation.

The simplified transport equation presented in Eq. (29) of Hébert's technical paper (2005) can be generalized to heterogeneous situations and used to describe a lattice with a unique resonant isotope. Here, we consider a simplified transport equation over a coarse group g where the non-resonant cross sections are assumed to be constant in lethargy. We write

$$\Omega\cdot\nabla\varphi(r,u,\Omega)+\Sigma(r,u)\varphi(r,u,\Omega) = \frac{1}{4\pi}\left[\Sigma_s^+(r)\mathbf{r}\{\varphi(r,u)\}\right] \quad (1.1)$$

where

$\varphi(r,u,\Omega)$ = fine structure function of the neutron flux

$\Sigma(r,u)$ = macroscopic total cross section of the resonant isotope at position $\boldsymbol{r}$

$\Sigma_s^+(r)$ = macroscopic P_0 scattering cross section of the non--resonant isotopes at position $\boldsymbol{r}$

$N^*(r)$ = number density of the resonant isotope at position $\boldsymbol{r}$

$\mathbf{r}\{\varphi(r,u)\}$ = microscopic slowing-down ope-rator for nuclear reactions with a single heavy isotope.

The *statistical slowing-down* (ST) model is based on the assumption that the resonances of the heavy isotope are narrow, numerous and statistically distributed in group *g*. This model is more accurate than the *narrow resonance* (NR) model where the resonances are assumed to be isolated, which is not the case at high neutron energy. The heavy isotope's slowing-down operator is written with the ST model as

$$\mathbf{r}\{\varphi(r,u)\} = \langle \sigma_s^*(r)\varphi(r)\rangle_g \quad \text{if} \quad u_{g-1} \le u < u_g \tag{1.2}$$

where

$$\langle \sigma_s^*(r)\varphi(r)\rangle_g = \frac{1}{\Delta u_g}\int_{u_{g-1}}^{u_g} du\, \sigma_s^*(r,u)\varphi(r,u). \tag{1.3}$$

In coarse energy group *g*, we define a probability table of order *K* as $\{\omega_k, \sigma_k^*(r), \sigma_{s,k}^*(r), k=1,K\}$. We next define $\varphi_k(r)$ as the space-dependent flux in subgroup *k*. Using Eq. (1.2), the subgroup form of Eq. (1.1) is written

$$\begin{aligned}&\Omega\cdot\nabla\varphi_k(r,\Omega)+\left[\Sigma^+(r)+\Sigma_k(r)\right]\varphi_k(r,\Omega)\\ &=\frac{1}{4\pi}\left[\Sigma_s^+(r)+N^*(r)\sum_{\ell=1}^{K}\omega_\ell\,\sigma_{s,\ell}^*(r)\varphi_\ell(r)\right]\end{aligned} \tag{1.4}$$

where

$\Sigma^+(r)$ = macroscopic total cross sections of the non-resonant isotopes at position $\boldsymbol{r}$

$\Sigma_k(r)$ = macroscopic total cross section of the resonant isotope in subgroup *k*

$\sigma_{s,\ell}^*(r)$ = microscopic P_0 scattering cross section of the resonant isotope in subgroup ℓ.

Equation (1.4) can be solved using an iterative approach. Scattering reduction consists to include the term $N^*(r)\omega_k\sigma_{s,k}^*(r)\varphi_k(r)$ in the LHS in order to reduce the total number of fixed point iterations. Eq. (1.4) is therefore replaced by

$$\begin{aligned}&\Omega\cdot\nabla\varphi_k(r,\Omega)+\left[\Sigma^+(r)+\Sigma_k(r)\right]\varphi_k(r,\Omega)\\ &-\frac{1}{4\pi}N^*(r)\omega_k\,\sigma_{s,k}^*(r)\varphi_k(r)\\ &=\frac{1}{4\pi}\left[\Sigma_s^+(r)+N^*(r)\sum_{\substack{\ell=1\\ \ell\neq k}}^{K}\omega_\ell\,\sigma_{s,\ell}^*(r)\varphi_\ell(r)\right].\end{aligned} \tag{1.5}$$

Equation (1.5) is solved iteratively using the following fixed-point approach:

$$\begin{aligned}&\Omega\cdot\nabla\varphi_k^{(n)}(r,\Omega)+\left[\Sigma^+(r)+\Sigma_k(r)\right]\varphi_k^{(n)}(r,\Omega)\\ &-\frac{1}{4\pi}N^*(r)\omega_k\,\sigma_{s,k}^*(r)\varphi_k^{(n)}(r)=\frac{1}{4\pi}S_k^{(n)}(r)\end{aligned} \tag{1.6}$$

where the space-dependent sources at iteration *(n)* are computed from the subgroup flux unknowns of the previous iteration using

$$S_k^{(n)}(r)=\Sigma_s^+(r)+N^*(r)\sum_{\substack{\ell=1\\ \ell\neq k}}^{K}\omega_\ell\,\sigma_{s,\ell}^*(r)\varphi_\ell^{(n-1)}(r). \tag{1.7}$$

If a second resonant isotope is admixed, or if the same resonant isotope is admixed with a different temperature, we represent this new instance as $b \neq a$ so that Eq. (1.6) must be updated to take into account the effects of *b*. The simplest approximation consists of neglecting any correlation between *a* and *b*. In this case, we write

$$\begin{aligned}&\Omega\cdot\nabla\varphi_k^{a,(n)}(r,\Omega)\\ &+\left[\Sigma^+(r)+\Sigma_k^a(r)+\Sigma_k^{b/a}(r)\right]\varphi_k^{a,(n)}(r,\Omega)\\ &-\frac{1}{4\pi}N^{*a}(r)\omega_k^a\,\sigma_{s,k}^{*a}(r)\varphi_k^{a,(n)}(r)=\frac{1}{4\pi}S_k^{a,(n)}(r)\end{aligned} \tag{1.8}$$

where

$$\Sigma_k^{b/a}(r)=\frac{\sum_{\ell=1}^{K_b}\omega_\ell^b\,\Sigma_\ell^b(r)\varphi_\ell^{b,(n-1)}(r)}{\sum_{\ell=1}^{K_b}\omega_\ell^b\,\varphi_\ell^{b,(n-1)}(r)} \tag{1.9}$$

and where the source term is now written as

$$\begin{aligned}S_k^{a,(n)}(r)=&\Sigma_s^+(r)+N^{*a}(r)\sum_{\substack{\ell=1\\ \ell\neq k}}^{K_a}\omega_\ell^a\,\sigma_{s,\ell}^{*a}(r)\varphi_\ell^{a,(n-1)}(r)\\ &+N^{*b}(r)\sum_{\ell=1}^{K_b}\omega_\ell^b\,\sigma_{s,\ell}^{*b}(r)\varphi_\ell^{b,(n-1)}(r).\end{aligned} \tag{1.10}$$

Equation (1.9) is the component of total cross section belonging to isotope *b* that should be included in the *k*–th subgroup of isotope *a*, taking into account any mutual interaction effect. Here, all mutual interaction effects are neglected. Consequently, the RHS of Eq. (1.9) is independent of index *k* and superscript *a*.

The above approximation is expected to be acceptable, provided that the energy group widths are small enough in the energy domains with overlapping resonances. The approximation is known to fail if isotopes *a* and *b* are corresponding to the same isotope at different temperatures. In this case, a *full-correlation* approximation can be written, as used in the ECCO lattice code (see Grimstone, Tullett and Rimpault,

1990):

$$\Omega\cdot\nabla\varphi_k^{a,(n)}(r,\Omega) + \left[\Sigma^{+}(r)+\Sigma_k^a(r)+N^{*b}(r)\sigma_k^a(r)\right]\varphi_k^{a,(n)}(r,\Omega) - \frac{1}{4\pi}N^{*a}(r)\,\omega_k^a\,\sigma_{s,k}^{*a}(r)\,\varphi_k^{a,(n)}(r) = \frac{1}{4\pi}S_k^{a,(n)}(r). \quad (1.11)$$

The full-correlation approximation consists to process each ring of fuel as a specific self-shielding problem, assuming that the neighboring rings are containing the resonant isotope at the *same temperature* as the temperature being processed. This approximation causes full-correlation in probability tables because all rings have the same resonant microscopic cross sections. Each ring is self-shielded at its exact temperature.

Finally, a general correlation model can be set, using the *correlated weight matrix* $\omega_{k,\ell}^{ab}$ previously introduced and obtained in Sect. II.B. of Hébert's technical paper (2005). In this case, Eq. (1.8) is used with Eq. (1.9) replaced by

$$\Sigma_k^{b/a}(r) = \frac{\sum_{\ell=1}^{K_b}\omega_{k,\ell}^{ab}\,\Sigma_\ell^b(r)\,\varphi_\ell^{b,(n-1)}(r)}{\sum_{\ell=1}^{K_b}\omega_{k,\ell}^{ab}\,\varphi_\ell^{b,(n-1)}(r)}. \quad (1.12)$$

The numerical effect of the correlation can be removed and Eq. (8) can be obtained by writing $\omega_{k,\ell}^{ab}=\omega_k^a\,\omega_\ell^b$. Similarly, a full correlation model can be obtained by writing $\omega_{k,\ell}^{ab}=\omega_k^a\,\delta_{k,\ell}$ where $\delta_{k,\ell}$ is the *Delta Kronecker function*.

Similar expressions can be written for the flux $\varphi_k^{b,(n)}(r,\Omega)$ in isotope *b*. Moreover, the overall approach can be generalized to an arbitrary number of admixed resonant isotopes.

The *k*–th subgroup flux and reaction rates can be averaged over each resonant region *i* using

$$\varphi_{i,k}=\frac{1}{V_i}\int_{V_i}d^3r\,\varphi_k(r) \quad (1.13)$$

and

$$\sigma_{\rho,i,k}=\frac{1}{V_i\,\varphi_{i,k}}\int_{V_i}d^3r\,\sigma_{\rho,k}(r)\,\varphi_k(r) \quad (1.14)$$

where V_i is the volume of the *i*–th resonant region.

After convergence of the subgroup flux unknowns, it is possible to compute the integrated flux $\langle\varphi_i\rangle_g$ and reaction rate $\langle\sigma_{\rho,i}\,\varphi_i\rangle_g$ for reaction ρ in region *i* using

$$\langle\varphi_i\rangle_g=\sum_{k=1}^{K}\omega_k\,\varphi_{i,k} \quad (1.15)$$

and

$$\langle\sigma_{\rho,i}\,\varphi_i\rangle_g=\sum_{k=1}^{K}\omega_k\,\sigma_{\rho,i,k}\,\varphi_{i,k} \quad (1.16)$$

where the probability table of group *g* has been used.

Numerical Results

We have based our validation study on a modified Rowlands pin-cell case (see Rowlands *et al.*, 1999) featuring a temperature gradient in fuel, as depicted in Fig 1. The comparisons were made for a light-water, MOX (UPuO2 fuelled), reactor pin-cell without leakage. The effects of changes in temperature were investigated in order to examine the consistency of temperature calculation methods.

The one-neutron source benchmark is limited to the resolved energy domain where it is possible to precisely define the resonant cross sections. The scattering kernel is assumed to be purely elastic.

Cross sections were defined in the resolved energy domain and distributed over SHEM–295 energy groups 56 to 206, located between 4.63 eV and 11.14 keV. A 1.0 n/cm³ · s source was placed in group number 56, located between 9.1188 keV and 11.138 keV and the absorption rates are computed in the remaining energy groups.

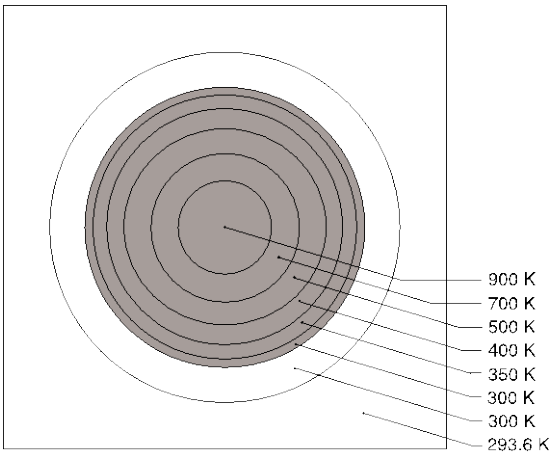

FIG. 1 TEMPERATURE GRADIENT IN A MOX PINCELL

Cross section libraries in PENDF and Draglib formats were build from scratch with NJOY release 99.259+upnea027. Draglib–formatted data is including temperature–dependent Autolib data for all resonant isotopes between 4.63 eV and 11.14 keV. The elementary lethargy width of the Autolib data is 5×10^{-4}.

Two computer codes have been used to perform these tests:

1. A computer code, named CESCOL, makes it possible to solve a fixed-source slowing-down equation using a P_0 elastic slowing-down operator for a mixture of heavy (resonant) isotopes in the resolved energy domain (see Hébert and Marleau, 1991). Heterogeneous cases can also be treated using collision probability (CP) techniques and used to generate reference solutions. CESCOL is implemented as a stand-alone module in a non-official version of DRAGON. Fine-group cross sections used by CESCOL are recovered in Autolib format from the Draglib database. Note that the same Autolib data is also used to compute the CALENDF probability tables used in the SPM subgroup model.
2. A self-shielding operator was written in the DRAGON Version 4.0.2 lattice code (see Marleau, Hébert and Roy, 2006 and Hébert, 2006) based on the SPM subgroup model. Self-shielded cross sections are obtained for a coarse energy grid and used in the existing CP flux solution operators. Consistency is emphasized by using the same CP calculation operator in both heterogeneous CESCOL and lattice code calculations.

We studied the absorption rates for the resonant isotopes in energy groups 56 to 206 and reported the discrepancies between CESCOL and lattice code. The main purpose of the numerical tests was to compare the proposed self-shielding methodology with reference

TABLE 1 SUMMARY OF MOX (FUEL 1) ONE-NEUTRON SOURCE BENCHMARK. USE OF SHEM—295

	effective temperature[a]	temperature gradient: no correlation	temperature gradient: full correlation (ECCO)	temperature gradient: correlated weight matrices (SPM)
ϵ^{int} (%)	0	5.700	0.327	0.280
$\bar{\epsilon}$ (%)	0.908	7.246	1.093	0.698
ϵ^{max} (%)	4.025	51.417	7.318	3.319
in group	126	100	131	124
^{235}U ϵ^{int} (%)	0.375	-4.009	-0.418	0.163
^{238}U ϵ^{int} (%)	-0.206	11.884	-0.204	0.245
^{238}Pu ϵ^{int} (%)	0.123	-3.610	-1.155	0.050
^{239}Pu ϵ^{int} (%)	0.202	1.808	0.680	0.416
^{240}Pu ϵ^{int} (%)	-0.437	4.501	1.032	0.021
^{241}Pu ϵ^{int} (%)	0.265	-2.435	0.971	0.134
^{242}Pu ϵ^{int} (%)	0.141	0.944	0.295	0.180
^{241}Am ϵ^{int} (%)	0.304	-2.250	1.423	0.176
^{238}U ϵ^{int} (%)				
shell 1	-5.318	7.450	0.126	0.775
shell 2	-3.912	8.529	1.261	0.766
shell 3	0.372	20.448	0.555	1.716
shell 4	5.023	21.519	-0.542	0.729
shell 5	8.914	31.739	-2.419	-1.832
shell 6	10.398	3.612	-3.218	-2.630

[a] Effective temperature set to T_{eff} = 628.95 K (ϵ^{int} = 0).

TABLE 2 SUMMARY OF MOX (FUEL 1) ONE-NEUTRON SOURCE BENCHMARK. USE OF XMAS–172

	effective temperature[a]	temperature gradient: no correlation	temperature gradient: full correlation (ECCO)
ϵ^{int} (%)	0	18.556	0.890
$\bar{\epsilon}$ (%)	2.744	14.051	3.084
ϵ^{max} (%)	10.775	61.209	11.781
in group	69	75	73
^{235}U ϵ^{int} (%)	0.846	-12.498	0.281
^{238}U ϵ^{int} (%)	-2.336	48.223	-2.094
^{238}Pu ϵ^{int} (%)	-1.443	-10.339	-1.984
^{239}Pu ϵ^{int} (%)	0.393	0.821	1.805
^{240}Pu ϵ^{int} (%)	4.492	12.221	8.606
^{241}Pu ϵ^{int} (%)	3.878	-8.723	3.767
^{242}Pu ϵ^{int} (%)	-2.768	-2.095	3.419
^{241}Am ϵ^{int} (%)	4.738	-7.744	4.165
^{238}U ϵ^{int} (%)			
shell 1	-6.172	24.247	-3.381
shell 2	-5.566	42.356	-3.781
shell 3	-1.884	107.491	-1.435
shell 4	1.778	86.643	0.524
shell 5	4.388	95.434	0.454
shell 6	5.029	12.078	-0.205

[a] Effective temperature set to T_{eff} = 449.25 K (ϵ^{int} = 0).

TABLE 3 SUMMARY OF MOX (FUEL 1) ONE-NEUTRON SOURCE BENCHMARK. USE OF SHEM–281

	effective temperature[a]	temperature gradient: no correlation	temperature gradient: full correlation (ECCO)
ϵ^{int} (%)	0	26.602	1.069
$\bar{\epsilon}$ (%)	3.426	22.001	3.119
ϵ^{max} (%)	16.286	61.006	18.866
in group	89	85	89
^{235}U ϵ^{int} (%)	-0.386	-9.676	-0.718
^{238}U ϵ^{int} (%)	-2.703	61.691	-1.406
^{238}Pu ϵ^{int} (%)	0.346	-4.853	0.073
^{239}Pu ϵ^{int} (%)	2.130	2.986	2.937
^{240}Pu ϵ^{int} (%)	2.256	8.999	5.277
^{241}Pu ϵ^{int} (%)	1.384	-6.519	1.068
^{242}Pu ϵ^{int} (%)	-1.194	-0.260	-0.265
^{241}Am ϵ^{int} (%)	2.830	-6.727	2.488
^{238}U ϵ^{int} (%)			
shell 1	-8.504	37.085	-2.256
shell 2	-4.954	56.041	-1.737
shell 3	0.718	115.593	-0.155
shell 4	4.546	94.756	0.496
shell 5	6.345	105.304	-0.295
shell 6	5.675	39.758	-1.746

[a] Effective temperature set to T_{eff} = 521.3 K (ϵ^{int} = 0).

CESCOL calculations. The corresponding numerical results corresponding to meshes SHEM–295, XMAS–172 and SHEM–281 are presented in Tables 1 to 3, respectively. We are reporting global error values for maximum ϵ^{max}, averaged $\bar{\epsilon}$ and integrated error ϵ^{int} isotopic and spatially-dependent ϵ^{int} values. This overall exercise was repeated with legacy SHEM–281g and XMAS–172g energy meshes. The percent errors on absorption rates are plotted in Fig. 2. Meshes XMAS–

172 and SHEM–281 are too coarse to enable use of CALENDF–based SPM. Consequently, the subgroup equations were solved using physical probability tables, as explained in Sect. 4.2.4 of *Applied Reactor Physics* (Hébert, 2009). Mesh SHEM–295, on the other hand, is fully compatible with the SMP and with the correlated weight matrix calculation presented in this paper.

An important observation is related to the use of the SPM–type general correlation model. The application of the SPM–type general correlation model permits to reduce the maximum error by a factor of two. It is important to note that the correlation model introduces no additional CPU costs in the subgroup solution, so that it can be left active in all situations. Both ECCO– and SPM–type correlation models permit to treat correctly the fuel temperature coefficient in presence of temperature gradient.

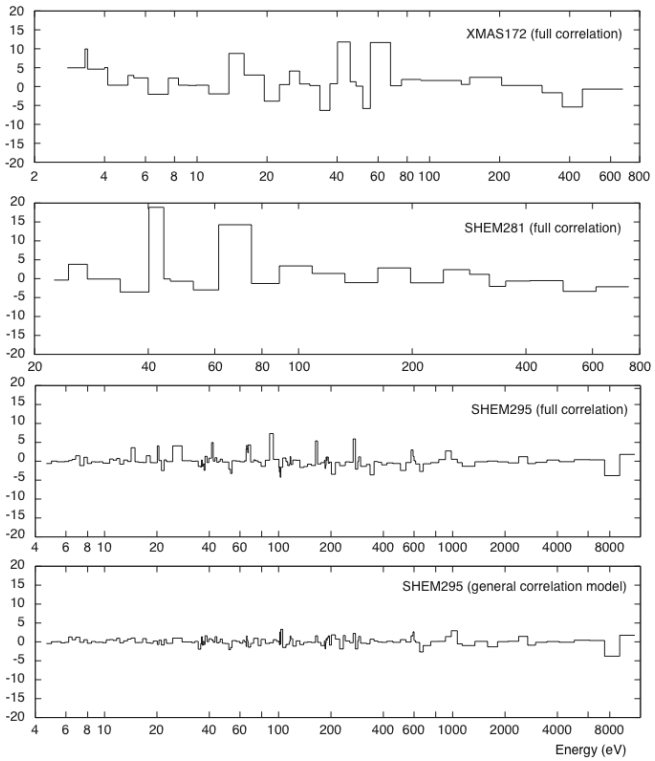

FIG. 2 PERCENT ERRORS ON ABSORPTION RATES

Conclusions

Current self-shielding approaches existing in legacy production codes are generally based on the effective temperature approximation. The ECCO approximation is a major leap forward for subgroup-based self-shielding methodologies. We observe that a full correlation model, similar to the ECCO approximation, can be included in those current approaches to represent temperature gradient effects in fuel. The main improvement on radiative capture accuracy occurs in the external fuel layer where ^{239}Pu builds up. The SPM goes one step further.

It can be combined with a general correlation model based on a rigorous CALENDF probability table approach. It is therefore possible to represent explicitly the temperature distribution. Moreover, the general correlation model of the SPM was found more accurate than the full correlation model. We have compared the SPM with current methodologies and presented numerical results related to simple MOX benchmarks.

REFERENCES

De Kruijf, W. J. M. and Janssen, A. J. "The Effective Fuel Temperature to be Used for Calculating Resonance Absorption in a $^{238}UO_2$ Lump with a Nonuniform Temperature Profile," *Nucl. Sci. Eng.*, **123**, 121 (1996).

Grimstone, M. J., Tullett, J. D. and Rimpault, G. "Accurate Treatments of Fast Reactor Fuel Assembly Heterogeneity with the ECCO Cell Code." *Proc. Int. Conf. on the Physics of Reactors: Operation, Design and Computation -- PHYSOR 90*, Marseille, France, p. IX:24, April 23-27 (1990).

Hébert, Alain and Marleau, Guy. "Generalization of the Stamm'ler Method for the Self-Shielding of Resonant Isotopes in Arbitrary Geometries," *Nucl.~Sci.~Eng.*, **108**, 230 (1991).

Hébert, Alain and Coste, Mireille. "Computing Moment-Based Probability Tables for Self-Shielding Calculations in Lattice Codes." *Nucl. Sci. Eng.*, **142**, 245–257 (2002).

Hébert, Alain. "The Ribon Extended Self-Shielding Model." *Nucl. Sci. Eng.*, **151**, 1–24 (2005).

Hébert, Alain. "Towards Version4." *Proc. of Int. Mtg. on the Physics of Fuel Cycles and Advanced Nuclear Systems: Advances in Nuclear Analysis and Simulation PHYSOR 2006*, Vancouver, Canada, (2006).

Hébert, Alain. "Development of the subgroup projection method for resonance self-shielding calculations." *Nucl. Sci. Eng.*, **162**, 56–75 (2009).

Hébert, Alain. "Applied Reactor Physics." Presses Internationales Polytechniques , Montréal (2009). See the website at http://www.polymtl.ca/pub/.

Marleau, Guy, Hébert, Alain and Roy, Robert. "A User's Guide for DRAGON, Version DRAGON Release 4.00." Report IGE-174, Institut de Genie Nucléaire, Ecole

Polytechnique de Montréal, Montréal (2006). Dragon can be downloaded from the website at http://www.polymtl.ca/merlin/.

Perruchot-Triboulet, Sophie. "Validation et extensions du module d'autoprotection du code de transport neutronique multigroupe APOLLO2," Ph. D. Thesis, Université d'Aix-Marseille, Marseille (1996).

Rowlands, John *et al.* "LWR Pin Cell Benchmark Intercomparisons. An Intercomparison study organized by the JEF Project, with contributions by Britain, France, Germany, The Netherlands, Slovenia and the USA.," *JEF Report to be published* , OECD/NEA Data Bank (1999).

Sources Localization for Brain Biomagnetic Activity

Spectral-analytical aproach

Sergey Makhortykh[*1], Ekaterina Lyzhko[2]

[1,2]Institute of Mathematical Problems of Biology Russian Academy of Sciencies
4 Institutskaya Str., Pushchino Moscow reg., Russia 142290

[*1]makh@impb.ru; [2]lyzko@yandex.ru

Received 19 March 2014; Accepted 27 March 2014; Published 27 June 2014

Abstract

A method for classifying types of brain activity in magnetoencephalographic (MEG) signals is proposed. Sources of abnormal cortical activity are localized by performing a generalized spectral analysis in the space of Fourier coefficients of the expansions of recorded signals in adaptive orthogonal bases. The basic principles of the method are discussed, and the results of its application to actual MEG records are presented for functional brain mapping in normal and pathological states.

Keywords

Biomagnetic Field; Magnetoencephalography; Generalized Spectral-analytical Method; Sources Localization

Introduction

Magnetoencephalography (MEG) is a recently developed experimental technique for studying human neural activity, mapping functional brain areas, and diagnosing various disorders. Research in this area is motivated by the possibility of noninvasive imaging of cortical and subcortical processes.

Until recently, the technique was difficult to apply because of the extreme weakness of both spontaneous and evoked neuromagnetic fields generated by current sources. Accordingly, the measuring apparatus to be employed must meet particularly stringent requirements.

Despite technical difficulties and the high cost of the required apparatus, this technique can be used as complementary or alternative to electroencephalography because magnetic field is much less perturbed by intracranial inhomogeneities and integumentary tissues than electric field, and the accuracy of source localization can therefore be substantially improved without detailed knowledge of the intracranial structure.

Data to Study

The input experimental data used in the present study were obtained by means of a 148-channel Magnes 2500 WH neuromagnetometer (a highly sensitive SQUID-based on magnetic field measurement system) at the New York University School of Medicine. The system was housed in a magnetically shielded room.

The analysis presented in this paper is focused on recognition and classification of patterns of magnetic field distribution over the subject's scalp for localizing neuromagnetic activity sources. This problem arises from the complex variability of an MEG signal during the measurement time (approximately 10-20 min), which includes alternating intervals of abnormal and normal activity. Intervals of abnormal and normal activity can easily be identified visually when they differ by the mean amplitude of the signal. Otherwise, visual inspection cannot be reliably used to identify intervals corresponding to different activity modes, and the dominant type of activity can be determined by analyzing the spatial field pattern, which strongly correlates with the number, location, and orientation of the current sources responsible for magnetic field generation.

The proposed approach was validated against data derived from a reference group of healthy individuals and a group of patients suffering from Parkinson's syndrome. The signal was a 148-dimensional time series measured at 148 points on the head surface at a

sampling rate of 500 Hz per channel.

The data analysis can be divided into the following tasks:

- detection of a signal associated with a particular type of brain activity (e.g., response to auditory, visual, tactile, or other stimulation; generation of Parkinson's tremor or auditory hallucinations; etc.);
- selection of instants for sampling the spatial field distribution over the head surface to be used as input in solving the inverse problem of current source localization;
- solution of the inverse problem of source localization in the cases of abnormal and normal activity;
- the use of fMRI data as physiological constraints.

Measurements with Phantom Sources

For the setting of algorithms for inverse problem solving the preliminary measurements were carried out. Here the data used have been obtained in measurements with phantom spherical conductor and were generated by 10 fixed dipoles of variable moments. Fig. 1 demonstrates this case. On the right figure points correspond to sensors positions, black and white are for positive and negative flux of the magnetic induction respectively.

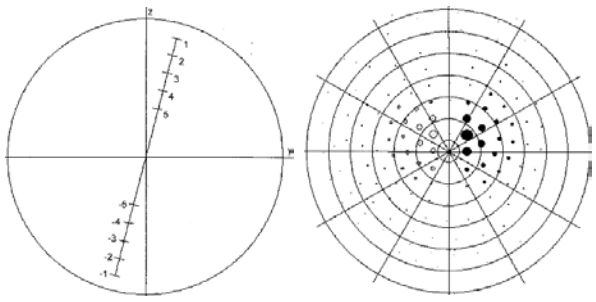

FIG1. TEST DIPOLES 1 - 5 AND THEIR ANTIPODES (LEFT) AND EXPERIMENTAL DATA SET FOR DIPOLE 1 (RIGHT)

An advantage of such problem formulation was in a priori knowledge of dipole positions. Thus, we can compare results of computer calculations in inverse problem with real dipole coordinates.

MEG Data Pre-processing

The reprocessing refers to the reading, segmenting around interesting events such as triggers, temporal filtering and optionally re-referencing of the data set. In the work preprocessing implements a Fourier transform filter, a Butterworth and a FIR filter for low-pass, high-pass and band-pass filtering.

Detection of artefacts can be done byusing manual or automatic artefact detection and visual identifying independent components (ICA).There are two ways to remove artefacts: 1) rejecting trial or the piece of trial containing the artefact; 2) subtracting the spatio-temporal contribution of the artefact from the data.ICA is most widely used for cleaning from cardiac, eye movements and blinks artefacts.

The application of transcranial magnetic stimulation (TMS) pulses during the data acquisition poses some specific challenges. This is an occurring of TMS artefact right after TMS pulse (pulseartefact, ringing/step response artefact, cranial muscle artefact) and recharging artefact in500ms after stimulation onset. There is a general trend for increase in artefact magnitude with TMS intensity. The following artefacts removal methods were used: removal large muscle artefacts from TMS by ICA (Korhonen et al., 2011), adapted recording system with software artefact correction (Litvak et al., 2007), off-line removal of TMS-induced artefacts on human magnetoencephalo-graphy by Kalman filter, based on cross-correlation coefficients of ICA (LeeU. et al., 2013). Thentime average ERP/ERF for all trials is computed andbaseline correction can be applied.

Frequency Analysis

It can be shown by means of spectral routines that oscillatory components contained in the MEG signal power changes regarding the system status. For this purpose frequency or time-frequency analysis based on Fourier bases and wavelets were used.

As an example, monaural audible stimulus was applied. Pulsing frequency was 7 Hz, while the response was localized at frequencies near 10 and 20 Hz. Fig. 2 shows this situation on the wavelet diagram (Makhortykh[2], 2009).

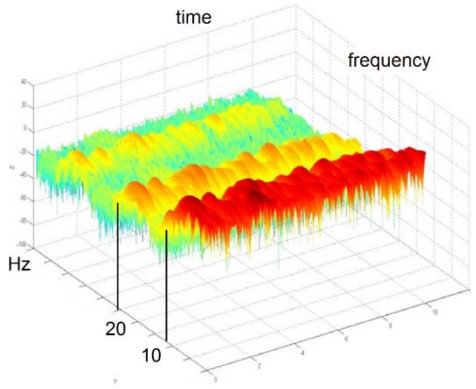

FIG.2. HAAR WAVELET DIAGRAM OF MEG RESPONSE FOR 7 HZ PULSING AUDIBLE STIMULATION

The Direct Problem

Consider the dipole current density **J** generated in an active region *G* of conductive brain tissue characterized by conductivity σ. Assuming a constant permeability$\mu = \mu_0$, we write the quasi-static Maxwell equations as

$$\begin{aligned} \mathbf{E} &= -\nabla\varphi, \\ \nabla\cdot\mathbf{B} &= 0, \\ \mathbf{J} &= \mathbf{J}_p + \sigma\mathbf{E}, \end{aligned} \tag{1}$$

where φ is the electric potential and **J** is the total current density. The magnetic field is calculated by the Biot- Savart law:

$$\mathbf{B}(r) = \frac{\mu_0}{4\pi}\int \mathbf{J}(r)\times\frac{(\mathbf{r}-\mathbf{r}')}{|\mathbf{r}-\mathbf{r}'|^3}dv'. \tag{2}$$

The variable of integration $\mathbf{r}'$ is dipole radius-vector.

Here we assume that the conductive region is a sphere and the source is a current dipole $\mathbf{J}(\mathbf{r}) = \mathbf{Q}\delta(\mathbf{r}-\mathbf{r_0})$ with dipole moment $\mathbf{Q}$ and position vector of a source $\mathbf{r_0}$.

According to (Sarvas, 1987), the magnetic induction on a homogeneous sphere enclosing the dipole can be calculated as

$$\mathbf{B}(\mathbf{r}) = \frac{\mu_0}{4\pi}F^2(F\mathbf{Q}\times\mathbf{r}_0 - \mathbf{Q}\times\mathbf{r}_0\cdot\mathbf{r}\nabla F) \tag{3}$$

It is clear that the outer magnetic field generated by a radially oriented source vanishes.

Therefore, the inverse problem is ill posed: thesource characteristics can be determined only up to an arbitrary radial component of the current dipole moment. Note also that the contribution of volume currents to the magnetic induction given by Eq. (3) does not depend on the conductivity σ.

The Inverse Problem

The locations and orientations of the sources of spontaneous activity are determined by using the magnetic field values at the measurement points to solve the inverse problem for Eq. (3). For the adopted model of brain activity and head geometry, the inverse problem can generally be reformulated as a nonlinear optimization problem for calculation of the locations and moments of the set of dipoles that provides the best approximation of the measured MEG data with respect to RMS deviation. The inverse problem is difficult solve primarily because it is ill posed: there exist infinitely many solutions consistent with the experimental data. The computational complexity of the nonlinear optimization problem is explained by the existence of multiple local extrema of the objective function, particularly when the number of dipole sources is large.

There also exist technical difficulties due to the weakness of both spontaneous and evoked magnetic fields generated by brain current sources against a high background noise level in MEG measurements.

To classify the types of neuromagnetic activity and identify abnormal intervals in MEG records, we use the feature space spanned by the spectral expansion coefficients of the total magnetic field on a sphere, which are invariant under rotation. The natural basis for describing the spatial field distribution is the set of spherical harmonics. Relevant features are extracted at the training stage of the algorithm by estimating the variability of the expansion coefficients for the class of objects under analysis. The upper bound for the dimension of the feature space depends on the length *N* of the Fourier expansion. There exists a simple analytical relationship between the expansion coefficients of functions whose arguments are related by an SO (2) transformation (Vilenkin, 1968), which makes it possible to develop a fast search procedure for functions in a particular class.

Source Analysis

Source estimation comprises two steps: 1) estimation of the potential or field distribution for a known source and for a known model of the head is referred to as direct modelling; 2) estimation of the unknown sources corresponding to the measured MEG is referred to as inverse modelling.

The head model specifies how currents that are generated by sources in the brain, e.g. dipoles, are influenced by the tissue properties and how these result in externally measureable MEG fields. For MEG the following head models are used: analytical single sphere model; local spheres model for MEG, one sphere per channel; realistically shaped single shell approximation, based on the implementation from Guido Nolte; magnetic dipole in an infinite vacuum. In the earliest studies, head models with simple geometries and homogeneous parameters were used, permitting many simplifications in the computation. When using models with spherical symmetry, solving the direct problem can be reduced to evaluating an analytic expression in Eq. (3).

To reconstruct the location and the time-course or

spectral content of a source in the brain, various source-localization methods are available. Here calculations with audible stimulation data and Parkinson patients' records used MRIAN software (Ustinin, Makhortykh *et al*., 2002). It is rather efficient for one- and two- dipoles problem with usage of structural restrictions by means of fMRI tomograms.

Results of spontaneous and induced sources localizations are presented by Fig. 3. It shows the response on the monaural audible stimulus in auditory cortex: 10 Hz source is in the contra lateral as long as 20 Hz source (see Fig. 2) is in the ipsilateral hemispheres. Fig. 3 b) demonstrates one of the localized source of pathological activity for the case of parkinsonian patient. Full description is brought out in (Makhortykh[1)], 2009).

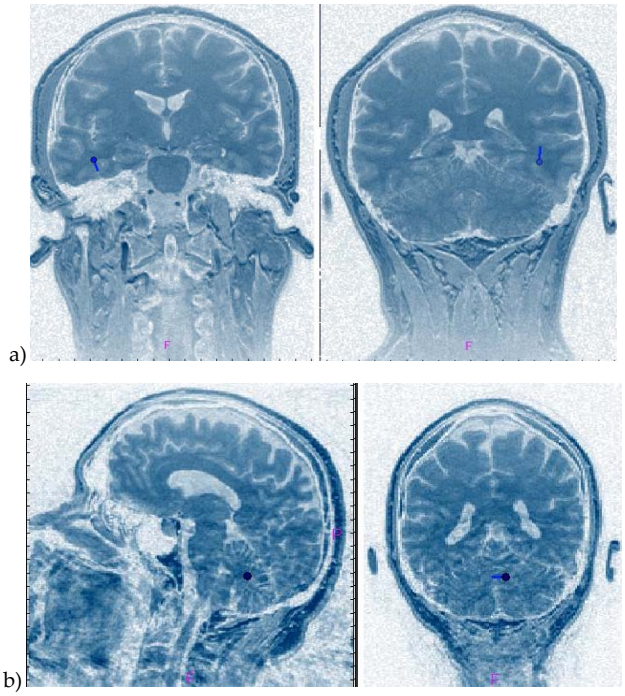

FIG.3. SOURCES LOCALIZATION (CIRCLES WITH RODS) FOR: A) INDUCED ACTIVITY (AUDIBLE STIMULUS RESPONSE) AND B) SPONTANEOUS PARKINSONIAN SIGNAL.

Conclusions

Analysis of MEG records and localization of brain biomagnetic activity are the bases of the cerebralprocesses functional mapping. Data preprocessing by means of generalized spectral method (Dedus, Makhortykh et al.,) allows to removing noise, highlighting the desired signal and in many cases determines the success of the solution. It uses a set of orthogonal bases so that spectral description can be scaled down to fit a particular class of signals. In many cases correct source localization and model parameters estimates can be obtained only after projection of the signal on the proper basic function (as on Fig. 2). Also expansion coefficients can be used as features for the system control and signal type recognition.

ACKNOWLEDGMENT

The work is supported by Russian Foundation for Basic Researches, projects 13-01-00340 and 14-07-00419.

REFERENCES

Dedus, A.F., F.F.Dedus, S.A.Makhortykh and M.N.Ustinin. "Generalized spectral-analytic method: theoretical fundaments." Proc. SPIE2363 (1995): 109.

Dedus, F.F., S.A.Makhortykh and M.N.Ustinin. "Generalized spectral-analytic method: Applications." Proc. SPIE 2363(1995): 113.

Lee, U. and W.K.Yoo. "TMS-induced EEG Artifacts Removal Methods based on Cross-Correlation Coefficients of ICA Components. "International Journal of Bio-Science and Bio-Technology5(5) (2013): 161-170.

Litvak, V, S. *et al.*"Artifact correction and source analysis of early electroencephalographic responses evoked by transcranial magnetic stimulation over primary motor cortex." NeuroImage37 (2007):56–70.

Makhortykh[1)], S.A. and R.A.Semechkin. "Brainmagneticfield study for Parkinson decease". Bulletin of Experimental Biology and Medicine 147(3) (2009): 351.

Makhortykh[2)], S.A. and R.A. Semechkin. "Localization and brain biomagnetic activity study for auditory stimulation." Bulletin of Experimental Biology and Medicine 147(4) (2009):477.

Sarvas, J."Basic mathematical and electromagnetic concepts of the biomagnetic inverse problem." Phys. Med. Biol. 32(1), (1987): 11-22.

Ustinin, M.N., S.A. Makhortykh *et al*. "Problems of magnetoencephology data analysis." In Computers and supercomputers in biology, edited by V.D.Lakhno and M.N.Ustinin. Moscow: Institute of Computer Science, 2002: 327-349 (In Russian).

Vilenkin, Ya. Special Functions and Theory of Group Representations. New York: AMS, 1968.

UWB Multi-Angle Human Posture Recognition

L B. Jiang, Y W. Ji, Y H. Bai, L. Che

School of Information and Communication Engineering, Guilin University of Electronic Technology,Guilin 541004, China

jlbnj@163.com, wenwen34wl@163.com, 815175300@qq.com, jlrq1@163.com

Abstract

In order to take the target aspect sensitivity of UWB echo into consideration and solve the problem that bispectrum has large amount of information, which is not favorable for classification. A method that extract rolling characteristics of average spectrum diagonal within 20°as features to recognize target using the Back Propagation(BP) classifier is presented. Human echo is simulated by using finite difference time domain (FDTD) algorithm based on 3D model. And measured data received from UWB radar prove the correctness of the simulation and the effectiveness of the recognition method.

Keywords

Ultra-Wide Bandwidth; Limited Finite Difference Time Domain (FDTD); Back Propagation; Rolling Characteristics; Target Aspect Sensitivity

Introduction

Human target detection and recognition have been widely used in military and security. Since 1990s,the research related to UWB radar target recognition

about human target has developed rapidly.

Doppler characteristics are often used in human body detection, but at that time doppler characteristics was not obvious, Static characteristics were very important. Compared with polarization characteristics, higher order statistics is simpler. Higher order statistics have been widely used in ships and other targets recognition, but seldom used in human posture recognition. Target aspect sensirimty of UWB radar echo and echo bispectrum have a large amount of information, which is unfavorable for classification. A method that extract rolling characteristics of average spectrum diagonal within 20° as features is presented in this paper. Target aspect sensirimty of UWB echo is an important issue which should be taken into consideration..

Radar echo simulation is the basis of echo characteristics analyzation. Target aspect sensitivity is one of the intrinsic defect of UWB echo. It has a great influence on target recognition. So at the time of feature extraction, this point must be taken into consideration.

Because human target is complex, human target radar echo simulation is a complicated problem.FDTD algorithm can directly simulate the field distribution, precision is high, which is one of the common methods to do numerical simulation. In this paper ,human target electromagnetic scattering FDTD model is put forward by Dogaru T., such as using FDTD technology to descript human target's radar cross section (RCS) precisely.

In order to take the target aspect sensitivity of UWB echo into consideration and solve the problem that bispectrum has large amount of information, which is not favorable for classification. A method that extract rolling characteristics of average spectrum diagonal within 20°as features to recognize target using the BP classifier is presented. Then human echo is simulated by using FDTD algorithm based on 3D model, these simulated data prove the effectiveness of the proposed method. Finally measured data from UWB rada prove the correctness of the model and the effectiveness of the proposed method. And then the paper discusses the problem about target aspect sensitivity of UWB echo.

Bispectrum Feature Extraction

Bispectrum Theory Derivation

Higher order statistics is simpler than the other main methods of analyzing characteristics. The third order cumulant and its bispectrum are used in this section. The indirect calculation method is used in this paper.

Data{x(1),⋯,x(n)} are divided into K section, each section contains M samples.

Firstly, estimate the third order cumulant of each section.

$$c^{(i)}(l,k)=\frac{1}{M}\sum_{t=M_1}^{M_2}x^{(i)}(t)x^{(i)}(t+l)x^{(i)}(t+k),i=1\ 2\cdot;\cdot,K \tag{1}$$

Where $\{x^{(i)}(n),n=1,2\ldots\}$ is the i.th section,

$$M_1=max(0,-l,-k)\quad M_2=min(M-1,M-1-l,M-1-k)$$

Then, the third-order cumulant average of all sections are calculated:

$$\hat{c}(l,k)=\frac{1}{K}\sum_{i=1}^{K}c^{(i)}(l,k) \tag{2}$$

Lastly, estimate bispectrum

$$\hat{B}_{IN}(w_1,\ w_2)=\sum_{l=-L}^{L}\sum_{k=-L}^{L}\hat{c}(l,k)w(l,k)exp\{-j(w_1l+w_2k)\} \tag{3}$$

Where L<M-1; $\omega(l,k)$ is window function, selecting the optimal window in this calculation.The optimal window is:

$$d_0(m)=\begin{cases}\frac{1}{\pi}\left|sin\frac{\pi m}{L}\right|+\left(1-\frac{|m|}{L}\right)cos\frac{\pi m}{L},|m|\le L\\ 0,|m|>l\end{cases} \tag{4}$$

The data x(n) in (1) is UWB human echo . Each echo is divided into 10 section (K=10).In order to reduce the complexity of calculation,L in(3)chooses 10; w_1,w_2 value range is between 0 and 200, sampling interval is 10.

Diagonal Rolling Feature Extraction

The bispectrum which is calculated according to expression (1)—(4) is a 21×21 matrix, take the diagonal of this matrix and do normalization.The diagonal b={b(1), b(2)…b(21)} is a vector with 21 elements.

In order to discuss the problem about target aspect sensitivity of UWB echo. Allowing for the average diagonal within 20 °(the gap is 1°), it can effectively reduce the effects of target aspect sensitivity.

$$b_{ave}(n)=\left[\sum_{i=\theta-10}^{\theta+10}b(n)\right]/2 \tag{5}$$

Where θ is the initial angle.

As the first element is zero, ignore the first element, the remainning elements are divided into four groups on average

$$ave(i)=[\sum_{n=2+5*(i-1)}^{6+5*(i-1)}b_{ave}(n)]/5\quad i=1,2,3,4 \tag{6}$$

The rolling feature T(m):

$$T(m)=\begin{cases}1 & ,ave(m+1)-ave(m)>0\\ 0 & ,ave(m+1)-ave(m)<0\end{cases}\quad m=1,2,3 \tag{7}$$

Simulation

Human Echo Simulation

3D models with precise size are established by Auto CAD. These models consists of three parts: "stand","sit" and "squat".There are 10 models in each part; the difference of these models in one part is the nuances of limb position or body tilt angle. Models which are selected from each part are shown in Fig.1

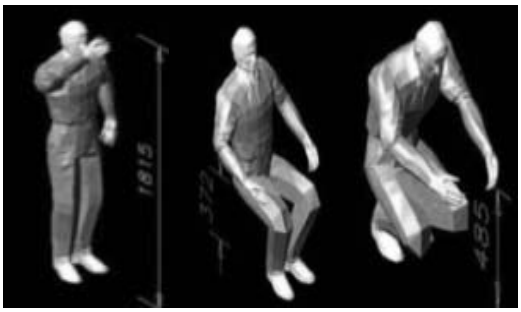

(A) (B) (C)

FIG.1 3 D MODEL OF DIFFERENT BODY POSTURE: (A)"STAND" (B) "SIT" (C) "SQUAT"

Then human echo can be calculated by FDTD algorithm. FDTD transforms the Maxwell curl equation into difference equations and can be combined with computer technology to deal with complicated electromagnetic problems . So the scattering models of human body are established by using FDTD method in this paper.

Due to the large internal impedance, electromagnetic field is weak inside human body, the human body internal electromagnetic field can be ignored in the research field of this paper. Set parameters by using electromagnetic parameters of the human body from the ARL experiment. Specific parameter Settings are shown in table 1:

TABLE 1: PARAMETERS OF SCATTERING MODEL

Parameters	Value
Center frequency	1GHz
pulse width	1ns
Incident angle	0°(or 45° or 90°)
Excitation source type	Plane Wave
Modulation Type	Modulated Gaussian
Average permittivity of human	50
Conductivity of human	1

Human target echo are shown in fig2-3:

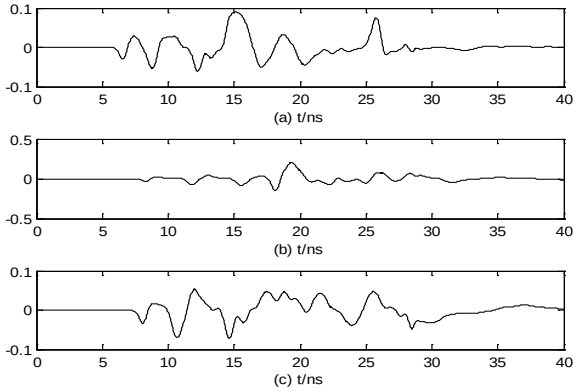

FIG 2: FAR FIELD TIME-DOMAIN ECHO(SIMULATION) FOR INCIDENCE ANGLE 0°,(A)"STAND" (B) "SIT" (C) "SQUAT"

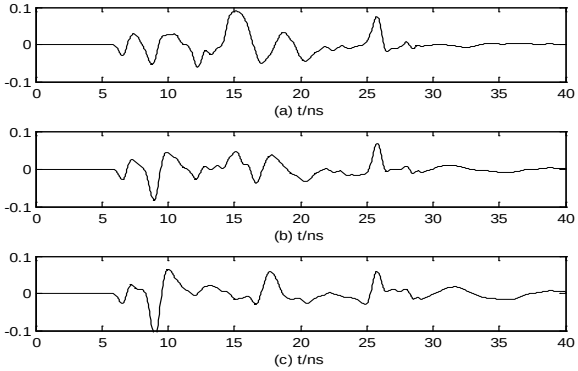

FIG3: FAR FIELD TIME-DOMAIN ECHO(SIMULATION)FOR HUMAN POSTURE IS "STAND", INCIDENCE ANGLE (A) 0° (B) 45°(C) 90°

Characteristics Of Simulation Data

The bispectrum calculated according to expression(1) - (4) is shown in fig 4 and fig 5:

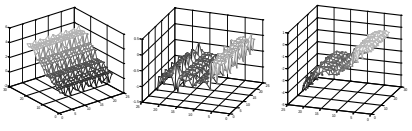

(A) (B) (C)

FIG 4: BISPECTRUM OF HUMAN BODY (INCIDENCE ANGLE 0°): (A)"STAND" (B) "SIT" (C) "SQUAT"

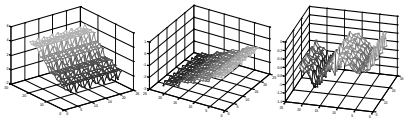

(A) (B) (C)

FIG 5: BISPECTRUM OF HUMAN BODY (, POSTURE IS "SIT"):INCIDENT ANGLE (A)0° (B)45° (C)90°

Then take diagonal of the bispectrum. Fit the data on the diagonal using the LS algorithm. The smooth fitting curves are shown in fig6 to fig8:

Conclusions can be got from the fitted curve. Firstly, when incident angle is 0°,"stand" fitting curve is similar to the linear growth."Sit" is oscillating, but the oscillation amplitude decrease. Although "Squat" curve has ups and downs, it can approximate to linear decrease. Then compare fitted curve with different incident angles. For "sit" attitude under different angle, the trend's difference is obvious. It shows that aspect sensitivity has effects on characteristics. This is unfavorable for target recognition. We do processing characteristics of different azimuth, in order to take the influence of aspect sensitivity into consideration.

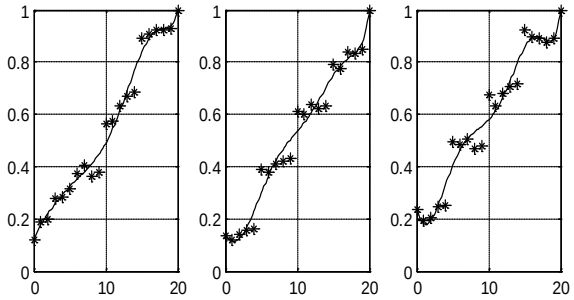

(A) (B) (C)

FIG 6: DIAGONAL OF HUMAN BODY "STAND" POSTURE:INCIDENCE ANGLE (A) 0° (B) 45° (C) 90°

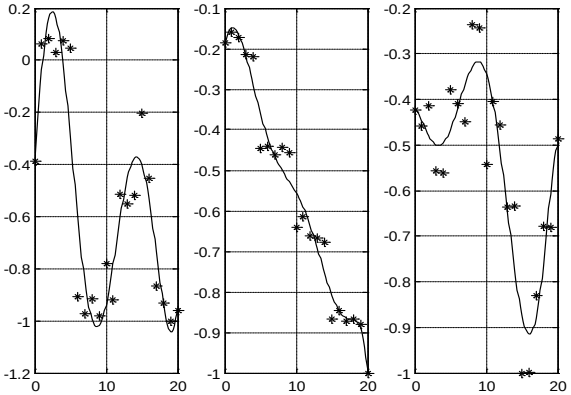

(A) (B) (C)

FIG7: DIAGONAL OF HUMAN BODY "SIT" POSTURE:INCIDENCE ANGLE (A) 0° (B) 45° (C) 90°

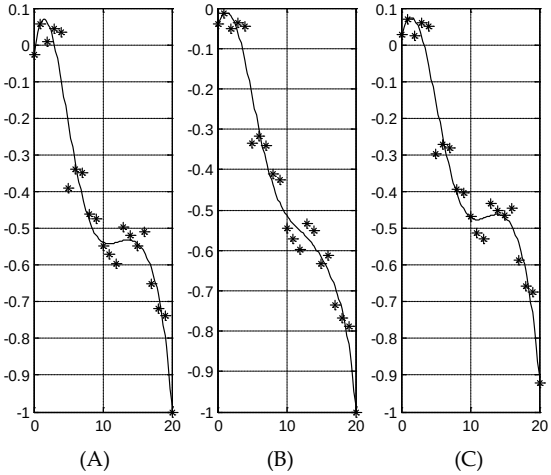

(A) (B) (C)

FIG 8: DIAGONAL OF HUMAN BODY "SQUAT" POSTURE:INCIDENCE ANGLE (A) 0° (B) 45° (C) 90°

Here we select 0 ° as the original angle, in the range of -10 ° to 10 °.The average diagonal calculated by expression(5) is shown in fig 9:

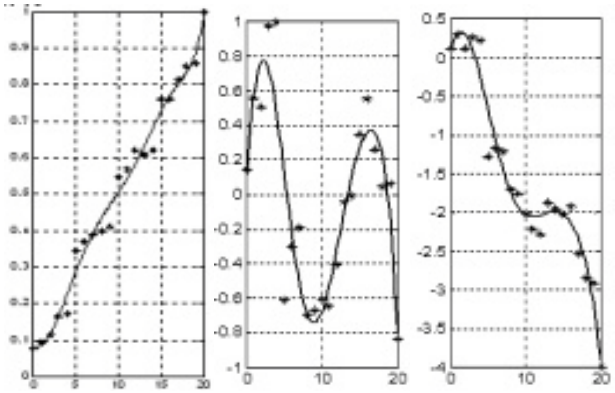

(A) (B) (C)

FIG9: AVERAGE DIAGONAL WITH INITIAL ANGLE 0°(A)"STAND" (B) "SIT" (C) "SQUAT"

Figure 9 shows that within a certain range, aspect sensitivity will have little impact on the characteristics. The target azimuth is divided into several parts (azimuth has little impact in each part), rather than considering each characteristics in different angle, it will effectively reduce the influence of aspect sensitivity.

The rolling characteristics are calculated according to expression(6) - (7) in 0 ° is shown in table 2:

TABLE 2: THE DIAGONAL ROLLING CHARACTERISTICS OF HUMAN BODY IN THREE DIFFERENT POSTURE WITH INITIAL ANGLE 0 ° (SIMULATION DATA)

posture	M1=1	M2=2	M3=3
stand	1	1	1
sit	0	0	1
squat	0	0	0

BP Neural Network Classification

BP neural network can learn and store a lot of input - output model mapping, without prior reveal describe the mathematical equations of the mapping relationship. Its learning rule is to use the steepest descent method, by back propagation to constantly adjust the network weights and threshold, minimize the error sum of squares of the network.

Here {M1,M2,M3} in table 2 are considered as input in BP network. And virtual output is 0,2,4. Where 0 means "stand", 2 means "sit",4 means "squat".

9 samples(each class 3samples) are randomly selected as test sample,the remaining as training sample. The classification accuracy of BP classifier is 100%

The pecific results are shown in fig 10:

As can be seen from the figure 10, the classification accuracy of simulation data is 100%.

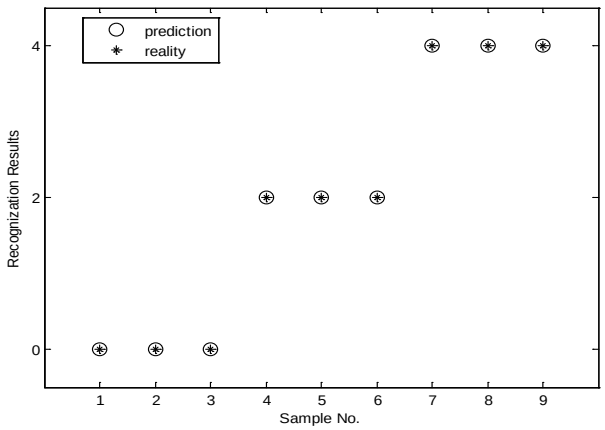

FIG10: CLASSIFICATION RESULTS(SIMULATION DATA):PREDICTION AND REALITY, 0 MEANS "STAND", 2 MEANS "SIT",4 MEANS "SQUAT".

Measure Data Validation

All the data are measured by UWB radar which center frequency is 1GHz,. pulse width is 1 ns.

The photo of measuring echo data is shown in fig11:

FIG11: MEASURING ECHO DATA

The echo signal measured by UWB radar is shown in fig12 and fig 13

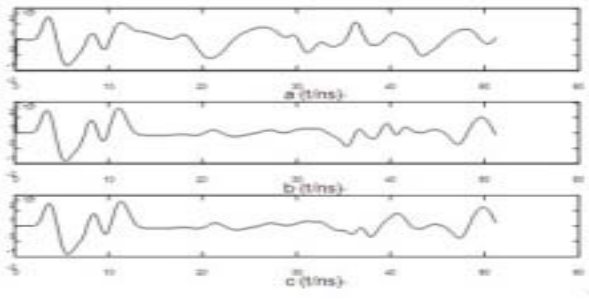

FIG 12: MEASURED ECHO :(A)"STAND" (B) "SIT" (C) "SQUAT"

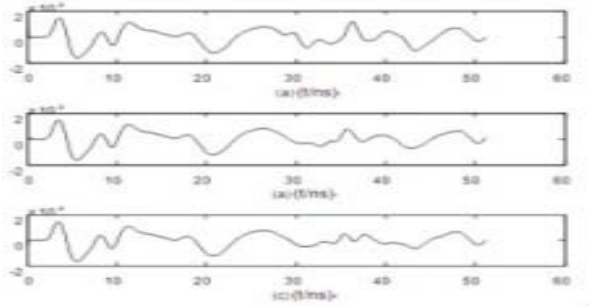

FIG13:MEASURES DATA:HUMAN POSTURE IS"STAND", INCIDENCE ANGLE(A) 0°(B) 45° (C) 90°

The first 112 points are radar coupling signal at the receiving terminal, only the last 400 points need to be analyzed. The bispectrum and its diagonal are shown in Fig 14 to fig16

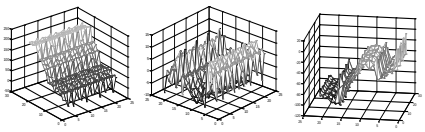

(A) (B) (C)

FIG 14: BISPECTRUM OF MEASURED DATA(INCIDENCE ANGLE 0°): (A)"STAND" (B) "SIT" (C) "SQUAT"

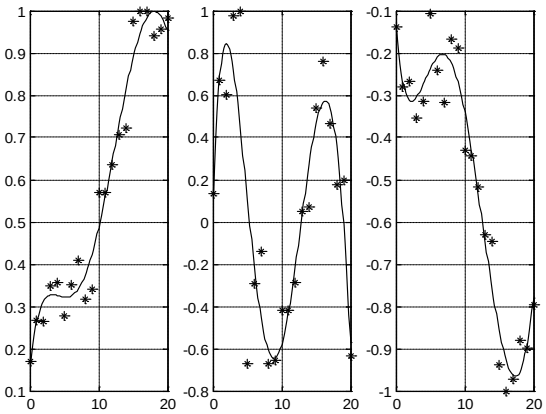

(A) (B) (C)

FIG 15: DIAGONAL OF MEASURED DATA(INCIDENCE ANGLE 0°: (A)"STAND" (B) "SIT" (C) "SQUAT"

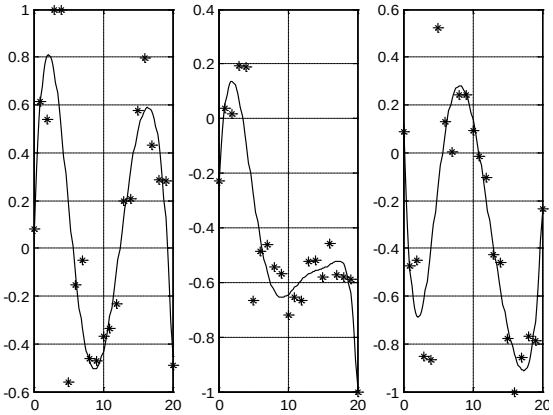

(A) (B) (C)

FIG16: DIAGONAL OF HUMAN BODY "SIT" POSTURE ,INCIDENCE ANGLE:(A)0°(B) 45° (C) 90°

Fig16 show the influence of target aspect sensitivity.

Compared with Fig15 and the theoretical results in Fig7, "sit" attitude of bispectrum diagonal is still rolling waveform, and the amplitude decreases. "stand" and "squat" attitude, though the bispectrum diagonal line in the middle of the data area, is still a trend of increasing and decreasing, respectively, consistent with the theoretical data, but at both ends, fitting curve shows slight ups and downs. Conclusion is basically the same from measured data and simulation data. The average diagonal calculated by expression(5). The rolling characteristics are calculated according to expression(6) - (7) with initial angle 0 ° are shown in table 3:

TABLE 3: THE DIAGONAL ROLLING CHARACTERISTICS OF HUMAN BODY ECHO SPECTRUM IN 0 °(MEASURED DATA)

posture	m=1	m=2	m=3
stand	1	1	1
sit	0	0	1
squat	1	0	0

18 samples(each class 6 samples) are randomly selected as test sample, the remaining as training sample.The pecific results of measured date are shown in fig 17

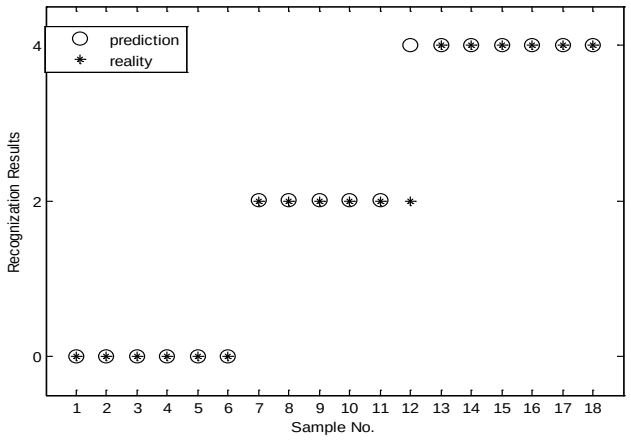

FIG17: CLASSIFICATION RESULTS(MEASURED DATA):PREDICTION AND REALITY, 0 MEANS "STAND", 2 MEANS "SIT",4 MEANS "SQUAT".

Make a misjudgment ,one "sit" is judged as "squat". The classification accuracy of measured data is 94.4%.

Conclusions

Aspect sensitivity is one of the intrinsic problems of UWB radar echo. By "sit" bispectrum diagonal values under different angle, we can see that aspect sensitivity has obvious influence on these characteristics. In this paper in order to take the effect of aspect sensitivity into consideration, take the average of diagonal values within 20 °(the gap is 1°). Then a method that extract rolling characteristics of average spectrum diagonal as feature to recognize target using BP neural network classifier is presented to solve the problem that bispectrum has large amount of information, which is not favorable for classification.

Simulated data which is simulated by FDTD based on precise body entity model prove effectiveness of the proposed method. The recognition accuracy (simulation data) reaches 100% with the intial angle is

0°.Measured data from UWB rada provethe correctness of the model and the effectiveness of the proposed method. The recognition accuracy (measured data)reaches 94.4% with the intial angle is 0°.

ACKNOWLEDGMENT

The authors thank guidance from vice professor Jiang and help from Bai Yun hao .

The National Natural Science Foundation of China **under Grant (61162007).**

Natural science fund project in guangxi (2013GXNSFAA019323)

Guangxi science and technology development plan (14122006-6);

REFERENCES

Balan A N, Azimi-Sadjadi M R." Detection and classification of buried dielectric anomalies by means of the bispectrum method and neural networks". Instrumentation and Measurement, IEEE Transactions on, 1995, 44(6).

Bryan J D, Kwon J, Lee N, et al."Application of ultra-wide band radar for classification of human activities", IET Radar, Sonar & Navigation., 2012,6,(3).

Jin W, Li Z J, Wei L S, et al. "The improvements of BP neural network learning algorithm". Signal Processing Proceedings, 2000. WCCC-ICSP 2000. 5th International Conference on. IEEE, 2000, 3.

Kong L Y, Wang J, Yin W Y."A NOVEL DIELECTRIC CONFORMAL FDTD METHOD FOR COMPUTING SAR DISTRIBUTION OF THE HUMAN BODY IN A METALLIC CABIN ILLUMINATED BY AN INTENTIONAL ELECTROMAGNETIC PULSE (IEMP)". Progress In Electromagnetics Research, 2012.

Li Y, Jing X, Lv H, et al. "Analysis of characteristics of two close stationary human targets detected by impulse radio UWB radar". Progress In Electromagnetics Research, 2012.

Luo Y, Zhang Q, Qiu C, et al."Micro-Doppler feature extraction for wideband imaging radar based on complex image orthogonal matching pursuit decomposition" IET Radar, Sonar & Navigation,2013, 7(8).

Van Dorp P, Groen F C A. "Human motion estimation with multiple frequency modulated continuous wave radars". Radar, Sonar & Navigation, IET, 2010, 4(3).

Warren C, Giannopoulos A. "Investigation of the directivity of a commercial Ground-Penetrating Radar antenna using a Finite-Difference Time-Domain antenna model".Ground Penetrating Radar (GPR), 2012 14th International Conference on. IEEE, 2012.

Yarovoy A G, Ligthart L P, Matuzas J, et al. "UWB radar for human being detection". Aerospace and Electronic Systems Magazine,2006,21(3).

Zhang Xianda."Time series analysis, higher order statistics method" . Tsinghua university press, 1996.

LiuBing.Jiang(China,1973.09.21)

He achieved his Bachelor of Engineering degree from the university of electronic science and technology in 1997 and the Master of Engineering degree from nanjing university of science in 2007.

Prof Jiang worked in Guilin University of Electronic Technology.His research field is radar signal processing, intelligent information processing

YaWen. Ji(China,1989.12.12)

She achieved her Bachelor of Engineering degree from Nanjing university of posts and communication in 2008.

Ms Ji is studying for her master's degree in Guilin University of Electronic Technology. Her research field is radar signal processing.

YuHao. Bai(China,1990.3.10)

He achieved her Bachelor of Engineering degree from Guilin University of Electronic Technology in 2008.

Mr.Bai is studying for her master's degree in Guilin University of Electronic Technology. Her research field is radar signal processing.

Li. Che(China,1977.6)

She achieved her Bachelor of Engineering degree from Hefei university of technology in 2000 and the Master of Engineering degree from Guilin University of Electronic Technology in 2011.

Ms. Che is working in Guilin University of Electronic Technology as a Senior experimentalist.Her research field is radar signal processing.

Charmonium Suppression in a Strongly Interacting Quark Gluon Plasma

Vineet Kumar Agotiya*[1], Indrani Nilima[2]

Centre for Applied Physics, Central University of Jharhand, Ranchi, India

agotiya81@gmail.com

Abstract

We study the survival probability of charmonium states in a strongly-interacting quark–gluon plasma with the dissociation temperatures obtained by correcting the full cornell potential not its Coulomb part alone with a dielectric function encoding the effects of deconfined medium. Our results show nice agreement with the experimental results at RHIC.

Keywords

Debye Mass; Medium-Modified; Heavy Quark Potential; Dissociation Temperature

Introduction

Charmonium suppression has long been proposed as a signature of QGP formation [1] and has indeed been seen at SPS[2]and RHIC experiments [3]. The heavy quark pair leading to the J/Ψ mesons are produced in nucleus-nucleus collisions on a very short time-scale ($1/2m_c$), where m_c is the mass of the charm quark. The pair develops into the physical resonance over a formation time τ_ψ and traverses the plasma and the hadronic matter before leaving the interacting system to decay (into a dilepton) to be detected. This long `trek' inside the interacting system is fairly`hazardous' for the J/Ψ. Even before the resonance is formed it may be absorbed by the nucleons streaming past it[4]. By the time the resonance is formed, the screening of the colour forces in the plasma may be sufficient to inhibit a binding of the $c\bar{c}$ [1].The resonance(s) could also be dissociated either by an energetic gluon [5,6] or by a commoving hadron. In order to extract these different effects, we must know the properties of quarkonium in medium and determine their dissociation temperatures.

The propagation of charm quark in SIQGP is different from wQGP because in SIQGP there will be a rapid equilibration due to the multiple momentum exchange in the momentum space but in the coordinate space, the motion is diffusive in nature and slower [7]. Therefore, the usual picture of charmonium suppression [1] may not be true in SIQGP. Moreover, in the RHIC era (small μ_B), it has been confirmed from the recent studies that the transition from nuclear matter to QGP is not a phase transition, rather a crossover [8].It is then reasonable to assume that the string-tension does not vanish abruptly at the deconfinement point, so we may expect presence of non-perturbative effects such as non-zero string tension in the deconfined phase and one should study its effects on heavy quark potential even above Tc. This is indeed compatible with the medium-modified heavy quark potential which was derived by correcting the full Cornell potential but not its Coulomb part alone with a dielectric function encoding the effects of the deconfined medium.We found that this approach led to a long-range Coulomb potential with an (reduced) effective charge in addition to the usual Debye-screened form. With such an effective potential, we determined the binding energies and dissociation temperatures of the ground and the first excited states of charmonium and bottomonium spectra[9].

The main motivation of this article is to remedy the above shortcomings in multifold respects: First we use an appropriate equation of state (EoS) which should reproduce the lattice results verifying the strongly-interacting nature of QGP. Then we explore the effects of dissipative terms on the hydrodynamic expansion by considering the shear viscosity η up to first-order in the stress-tensor. Basically we consider the ratio of the shear viscosity-to-entropy density (η/s)as $(1/4\pi)$ and 0.3 which was predicted from the AdS/CFT correspondence [10] and perturbative QCD [11], respectively and we consider ideal hydrodynamics with $\eta/s = 0$ for the sake of comparison. And finally the most important point is to know the properties of quarkonium in the medium. Finally we study the survival of charmonium states.

Equation Of State

The equation of state for the quark matter produced in RHIC is a very important observable and the expansion of QGP is quite sensitive to the equation of state (EoS) through the speed of sound. Both experimental [12] and theoretical (lattice) results [13]show that matter formed near or above Tc is non-ideal. There have been many attempts to explain such a matter using various models such as bag models, other confinement models [14], quasi particle models [15], strongly interacting quark gluon plasma (sQGP) [16] etc. Here we propose that the QGP near Tc is in fact what is called strongly coupled plasma[17], widely studied in QED plasma where the plasma parameter, γ , defined as the ratio of the average potential energy to the average kinetic energy of the particles, is of the order of 1 or larger. And the strong running coupling constant gives an expression for the energy density as a function of the plasma parameter, γ

$$\varepsilon = (2.7 + u_{ex}(\Gamma))nT \tag{1}$$

where the first term corresponds to the ideal EoS and the second term gives the non-ideal (or excess) contribution to EoS. So, the scaled energy density (in terms of Stefan-Boltzmann limit)is given by

$$e(\Gamma) \equiv \frac{\varepsilon}{\varepsilon_{SB}} = 1 - \frac{1}{2.7}\frac{\sqrt{3}}{2}\Gamma^{3/2} \tag{2}$$

where

$$\varepsilon_{SB} = 3a_f T^4$$

with degrees of freedom

$$a_f \equiv (16 + 21n_f / 2)\pi^2 / 90$$

we get the pressure

$$\frac{p}{T^4} = \left(\frac{p_0}{T_0} + 3a_f T^4 \int_T^{T_0} d\tau \tau^2 e(\Gamma(\tau)) \right) / T^3 \tag{3}$$

where p_0 is the pressure at some reference temperature T_0. If we calculate $p(T)/T^4$ versus T for pure gauge, 2-flavor and 3-flavor QGP, a surprisingly good fit with the lattice data was found [14,17]. Another important observable, the speed of sound which appears in the equation of motion for the expansion through the relation,

$$C_s^2 = \frac{\partial p}{\partial \varepsilon} \tag{4}$$

In view of the excellent agreement with lattice simulations the above phenomenological EoS is a right choice for the strongly-interacting matter possibly formed at RHIC to calculate the thermodynamical quantities *viz*. screening energy density,the speed of sound etc. and also to study the hydrodynamical expansion of plasma.

Longitudinal Expansion In The Presence Of Dissipative Forces

In the presence of viscous forces the energy-momentum tensor is written as

$$T^{\mu\nu} = (\varepsilon + p)u^\mu u^\nu + g^{\mu\nu} p + \pi^{\mu\nu}, \tag{5}$$

where $\pi^{\mu\nu} = \eta\langle \nabla^\mu u^\nu \rangle$ is the stress-energy tensor.In (1+1) dimensional Bjorken expansion in the first-order dissipative hydrodynamics, only one component $\pi^{\eta\eta}$ of the viscous stress tensor is non-zero. In this case the equation of motion reads,

$$\frac{\partial \varepsilon}{\partial \tau} = -\frac{\varepsilon + p}{\tau} + \frac{4\eta}{3\tau^2} \tag{6}$$

The solution of the above equation in the case of constant value of η/s is known analytically [18,19] and is given by

$$\varepsilon(\tau)\tau^{1+C_s^2} + \frac{4a}{3\tilde{\tau}^2}\tau^{1+C_s^2} = \varepsilon(\tau_i)\tau_i^{1+C_s^2} + \frac{4a}{3\tilde{\tau}_i^2} = const \tag{7}$$

Where

$$a = \left(\frac{\eta}{s}\right) T_i^3 \tau_i$$

and

$$\tilde{\tau}^2 = \left(1 - C_s^2\right)\tau^2$$

The first term in both LHS and RHS accounts for the contributions coming from the zeroth order expansion and the second term is the first-order viscous corrections. We shall employ Eq.(7) to study the charmonium suppression in a strongly interacting QCD medium formed in a ultra-relativistic heavy-ion collisions in the next section.

Suppression Of J/Ψ In A Longitudinally Expanding Plasma

To study the fate of charmonium in SIQGP, we need to consider the equation of state for SIQGP and the effects of dissipative forces (shear viscosity) on the expansion, and an appropriate criterion for the dissociation of charmonium in hot QCD medium. So we briefly discuss the nature of dissociation by examining the effects of perturbative and non-

perturbative terms in the Debye masses and listed the dissociation temperatures in Table 1 which will be used to quantify the suppression. Finally we derive the survival probability of J/ψ in an expanding SIQGP.

The dissociation of quarkonium in QGP has successfully been addressed by deriving an appropriate form of the medium-modified heavy quark potential [9] as

$$V(r,T) = \left(\frac{2\sigma}{m_D^{\,2}(T)} - \alpha\right)\frac{\exp(-m_D(T)r)}{r} - \frac{2\sigma}{m_D^{\,2}(T)r} + \frac{2\sigma}{m_D(T)} - \alpha m_D(T) \quad (8)$$

The medium modified form of the potential thus obtained has an additional long range Coulomb term with an effective charge in addition to the conventional Yukawa term. The binding energies and hence the dissociation temperatures for various quarkonia states have been determined by solving the Schrodinger equation numerically with the potential (8). For this work, we consider two forms of the Debye masses [7] and the lattice parametrized form [20] to study the dissociation of resonances. In the work of Chu and Matsui [21], the p_T dependence of the survival probability of charmonium was studied by choosing the speed of sound for ideal EoS. Instead of taking arbitrary values of speed of sound we tabulated the values of speed of sound as well as other parameters in Tables 1 and 2, corresponding to different sets of dissociation temperatures of the quarkonia states calculated from Bannur model [17].

In nucleus-nucleus collisions, it is known that only about 60% of the observed J/ψ originate directly in hard collisions while 30% of them come from the decay of χc and 10% from the decay of ψ′. Hence, the P_T-integrated inclusive survival probability of J/ψ in the QGP becomes [22,23].

$$\langle S^{incl} \rangle = 0.6\langle S^{dir} \rangle_{\psi} + 0.3\langle S^{dir} \rangle_{\chi_c} + 0.1\langle S^{dir} \rangle_{\psi'}$$

The hierarchy of dissociation temperatures in lattice correlator studies [24] (Table 2) thus leads to sequential suppression pattern with an early suppression of ψ′ and χc decay products and much later one for the direct J/ψ production. However (Table 1) employing medium modification to the full Cornell potential and also results from potential model studies [20] on dissociation temperatures, all three species will show essentially almost the same suppression pattern.

Results and Discussions

There are three time-scales involved in the screening scenario of J/ψ suppression in an expanding plasma. First one is the screening time, τ_s as the time available for the hot and dense system during which J/ψ's are suppressed. Second one is the formation time of J/ψ in the plasma frame which depends on the transverse momentum by which the $c\bar{c}$ pairs was produced. Third one is the cooling rate which depends on the speed of sound through the EoS. The screening time not only depends upon the screening energy density but also on the speed of sound through EoS. If screening energy density is greater than or equal to initial energy density, then there will be no suppression at all i.e., survival probability is equal to 1. If the dissociation temperature T_D is higher, screening energy density will also be higher. Therefore, the system will get less time to kill J/ψ in the deadly region marked by the screening radius, r_s results in less suppression in the J/ψ yield. However, for smaller values of T_D, the system will take more time to reach screening energy density resulting more suppression.

More precisely, the screening time depends upon the difference between the initial energy and the screening energy density: the more will be the difference, the more will be the suppression, the speed of sound: the values of c^2_s which are less than 1/3, the rate of cooling will be slower which, makes the screening time large for a fixed difference in screening energy density and initial energy density leading to more suppression, and the η/s ratio: if the ratio is larger then the cooling will be slower, so the system will take longer to reach screening energy density resulting in the higher value of screening time and hence more suppression compared to η/s = 0. With this physical understanding we analyse survival probability as a function of the number of participants N_{Part} [3] in an expanding QGP.

TABLE 1 FORMATION TIME (FM), DISSOCIATION TEMPERATURE T_D (IN UNITS OF TC=197 MEV FOR A 3-FLAVOR QGP) WITH THE DEBYE MASS IN LEADING-ORDER(LATTICE PARAMETRIZED FORM) [9], SPEED OF SOUND AND SCREENING ENERGY DENSITY CALCULATED IN SIQGP

States	τ_F	T_D		$\varepsilon_s/\varepsilon_{Q\bar{Q}}$
J/ψ	0.89	1.61(1.18)	0.26(0.24)	17.66(4.83)
Ψ′	1.50	1.16(0.85)	0.24(0.18)	4.51(1.21)
χ_c	2.00	1.25(0.90)	0.24(0.19)	6.15(1.54)

Conclusions

In conclusion, we have studied the charmonium suppression in a longitudinally expanding Quark

Gluon Plasma in the presence of dissipative forces. We find that the presence of viscosity enhances the screening time for J/ψ in the SIQGP medium and hence the survival probability gets decreased compared to that without the viscous forces. These conclusions are true for both the directly and sequentially produced J/ψ. We have employed the SIQGP equation of state to estimate the screening energy density and the speed of sound to study the J/ψ yield. To compare our results with those obtained by employing the simple screening picture of quarkonia commonly considered in the literature [24], we find that the results on J/ψ survival probability agree with the Phenix Au-Au data [2] with the set of dissociation temperatures (Table 1) obtained with the perturbative result of the Debye mass.

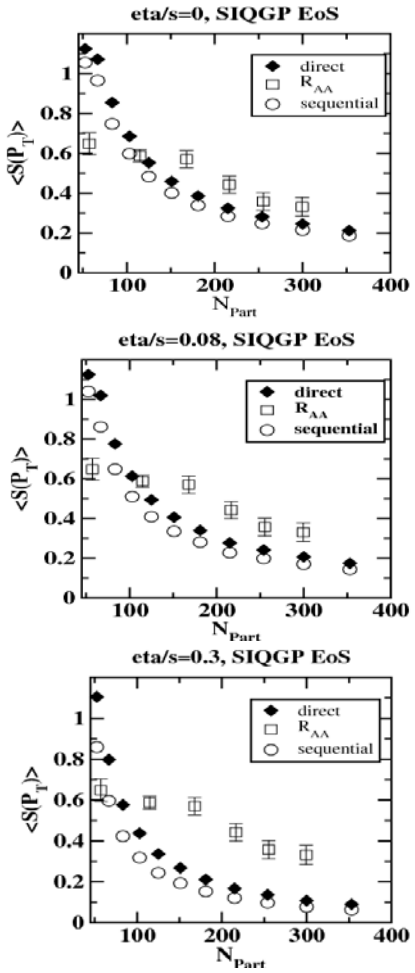

FIG. 1 THE VARIATION OF P_T INTEGRATED SURVIVAL PROBABILITY (IN THE RANGE ALLOWED BY INVARIANT P_T SPECTRUM OF J/Ψ BY THE PHENIX EXPERIMENT [3]) VERSUS NUMBER OF PARTICIPANTS AT MID-RAPIDITY. THE EXPERIMENTAL DATA (THE NUCLEAR-MODIFICATION FACTOR R_{AA}) ARE SHOWN BY THE SQUARES WITH ERROR BARS WHEREAS CIRCLES AND DIAMONDS REPRESENT THE SEQUENTIAL AND DIRECT MELTING USING THE RELATED PARAMETERS FROM TABLE 1 USING SIQGP EQUATION OF STATE.

TABLE 2 FORMATION TIME (FM), DISSOCIATION TEMPERATURE T_D [24] (IN UNITS OF TC=175 MEV FOR A 3-FLAVOR QGP) WITH THE DEBYE MASS IN LATTICE PARAMETRIZED FORM [9], SPEED OF SOUND AND SCREENING ENERGY DENSITY CALCULATED IN SIQGP

States	τ_F	T_D		
J/ψ	0.89	2.10	0.27	2.85
Ψ′	1.50	1.12	0.21	2.36
χ_c	2.00	1.16)	0.22	2.74

ACKNOWLEDGMENT

VKA Acknowledges MHRD, New Delhi (India) for the financial support and also thankful to the Vice Chanceller of Central University of Jharkhand Ranchi, India for provided the infrastructural facilities.

REFERENCES

T. Matsui and H. Satz, Phys. Lett. B 178 (1986) 416.

G. Borges, NA50 Collaboration, J. Phys. G 32 (2006) S 381.

J. Adams, et al., Phys. Rev. Lett. 92 (2004) 112301.

C. Gerschel and J. Hufner, Phys. Lett. B 207 (1988) 253.

X. M. Xu, D. Kharzeev, H. Satz, and X. N. Wang, Phys. Rev. C 53 (1996) 3051.

B. K. Patra, V. J. Menon, Eur. Phys. J. C 37, 115 (2004); Eur. Phys. J. C 44 (2005) 567.

C. Young and E. Shuryak, Phys. Rev. C 79 (2009) 034907.

F. Karsch, hep-lat/0601013; Journal of Physics: Conference Series 46 (2006) 121.

V. Agotiya, V. Chandra and B. K. Patra, Phys. Rev. C 80 (2009) 025210, arXiv:Nucl-th/0910.0586

P. Kovtun, D. T. Son, A. O. Starinets, Phys. Rev. Lett. 94 (2005) 111601.

P. Arnold, G. D. Moore, and L. G. Yaffe, JHEP 11 (2000) 001; ibid 05 (2003) 051.

M. Gyulassy, nucl-th/0403032 (2004).

G. Boyd, J. Engels, F. Karsch, E. Laermann, C. Legeland, M. Lutgemeier and B. Petersson, Phys. Rev. Lett. 75 (1995) 4169; Nucl. Phys. B 469 (1996) 419.

V. M. Bannur, Phys. Lett. B 362 (1995) 7.

A. Peshier, B. Kampfer, O. P. Pavlenko and G. Soff, Phys. Lett. B 337 (1994) 235.

E. Shuryak, Nucl. Phys. A 750 (2005) 64.

V. M. Bannur, J. Phys. G: Nucl. Part. Phys. 32, 993 (2006); Phys. Rev. C 76 (2007) 044908; Phys. Lett. B 647(200 7) 271.

H. Kouno, M. Maruyama, F. Takagi, and K. Saito, Phys. Rev. D 41 (1990) 2903.

A. Muronga, Phys. Rev. Lett. 88 (2002) 062302 [Erratum-Phys. Rev. Lett. 89 (2002) 159901]; Phys. Rev. C 69, 034903 (2004) 034903.

A. Mocsy and P. Petreczky, Phys. Rev. Lett. 99 (2007) 211602.

M. C. Chu and T. Matsui, Phys. Rev. D 37 (1988) 1851.

D. Pal, B. K. Patra, and D. K. Srivastava, Eur. Phys. J. C 17 (2000) 179.

H. Satz, Nucl. Phys. A 783 (2007) 249.

S. Datta, F. Karsch, P. Petreczky, and I. Wetzorke, Phys. Rev. D 69 (2004) 094507.

New Strategy to Evaluate the Effectiveness of New Treatments using Animal Models

Cibele B. Zamboni[1], Sabrina Metairon[*1], Ivone M. Sato[1] , Marcia A. Rizzutto[2]

[1]Instituto de Pesquisas Energéticas e Nucleares (IPEN/CNEN- SP), Brazil/ [2]Universidade de São Paulo (IFUSP- SP), Brazil

[1]Av. Professor Lineu Prestes 2242, 05508-090, São Paulo, SP, Brazil

[2]Rua: do Matão Travessa R 187, 05508-090, São Paulo, SP, Brasil

[1]czamboni@ipen.br;[*1]metairon@live.com;[1]imsato@ipen.br;[2]rizzutto@if.usp.br

Abstract

In this study we intend to present a new strategy to clinical practices that can help researchers in medical and correlated areas to evaluate the effectiveness of new treatments which has been tested in animal models. Furthermore, we also present a discussion about the economic viability of applying these alternative procedures in clinical laboratories.

Keywords

XRF; Whole Blood; Clinical Practices; Animal Models

Introduction

In health area animal models are used in medical investigation of new treatments, drugs, vaccines and many other biological products before being applied in human being. As a routine these animals are submitted to several biochemistry analyses (such as: Calemia, Calcemia, Natremia, etc.), usually performed in serum. However, when small size animal model is involved the biological material can be scarce and limit its collections. The viability to perform these clinical analyses using EDXRF (Energy Dispersy of X Ray fluorescency) technique can simplify several steps involved in checking the effectiveness of new treatments or drugs. The main advantage for using this technique is the viability to use small quantities of body fluids (10 times less, at least, compared with the conventional clinical tests). Recently the Spectroscopy and Spectrometry Radiation Laboratory at IPEN – CNEN/SP (Brazil) has applied this clinical alternative in body fluids analyses (mainly whole blood and urine) of animal models, mainly small size (such as mice, rats and rabbits). In this study we intend to present the details for implementation and execution of clinical practice using this alternative procedure.

Material and Methods

The biological samples from Wistar rats (n = 10, male), were collected according to the rules approved by Animal Research Ethics Committee (087/99). More details are presented in a previous study [Oliveira L., et al.]. Immediately after the collection 50μL of biological fluid (whole blood, serum and urine) was transferred to the filter paper (Whatman, nº 41) using a calibrated micropipette and each biological sample was dried for few minutes using an infrared lamp (see an example of whole blood dried in Figure 1a). The same procedure was applied for serum and urine. The XRF analysis was performed using two X-Ray spectrometers: an EDXRF Spectrometer SHIMADZU Co. model Rany 720 (Figure 1b), with: 50kV, 100 μA-variable, Rh target, Si(Li) detector and fixed time counting of 100s, and a MINI-X spectrometer (Amptek) (Figure 1c) with: 30kV, 5μL- variable, Ag X-ray Target and a Si Drift detector (25 mm2 x 500μm / 0.5 mil) with Be window (1.5") and variable range time (300s and 600s). The quantitative analyses used in the EDXRF and Mini X-Ray spectrometers were performed with Shimadzu and WINAXIL software's, respectively.

a) b) c)

FIG. 1 a) BLOOD SAMPLE; b) SHIMADZU EDXRF SPECTROMETER; c) AMPTEK MINI X-RAY SPECTROMETER

Results and Discussion

The adequacy of the measurment was evalute for Fe using the certified reference material IAEA-A-13 Animal blood. The evaluation of the Z-score test (-0.8) is satisfactory ($|Z| < 2$).

The Iron concentrations determined in serum, whole

blood and urine samples from boths spectrometers are in agreement. In Table 1 is presented a summary of the data obtained using MINI X-ray spectrometer. The results were expressed by: Time Counting (Tc), Median Value (MV), Standard Deviation (1SD), Detection Limit (DL), Quantification Limit (QL) and Reference Values (RV) (for a confidence interval of 95%).

TABLE 1. IRON CONCENTRATIONS RESULTS IN BIOLOGICAL MATERIAL

Serum (Tc = 600s)	**Fe, µg dL^{-1}**
MV ± 1SD	58 ± 18
DL	2.2
QL	6.7
RV	22 – 94
Urine (Tc = 600s)	**Fe, µg dL^{-1}**
MV ± 1SD	60 ± 13
DL	3.1
QL	9.4
RV	34 – 86
Whole Blood (Tc = 300s)	**Fe, mg dL^{-1}**
MV ± 1SD	388 ± 52
DL	7.5
QL	22.7
RV	284 – 492

To illustrate, in Fig. 2, 3, 4 and 5 are presented the results for detection limit and Iron concentration in whole blood and serum, respectively. In Fig. 6 the whole blood and serum spectra using MINI X-ray spectrometer are presented.

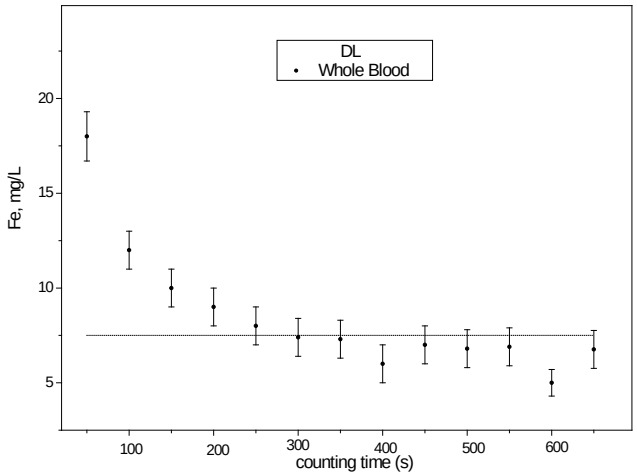

FIG. 2 WHOLE BLOOD DETECTION LIMIT USING PXRFS

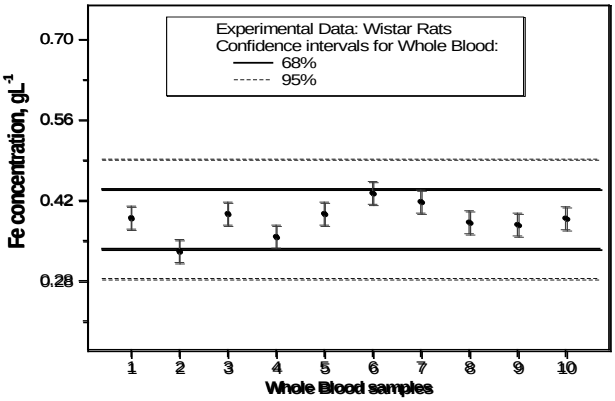

FIG. 3 WHOLE BLOOD IRON CONCENTRATIONS

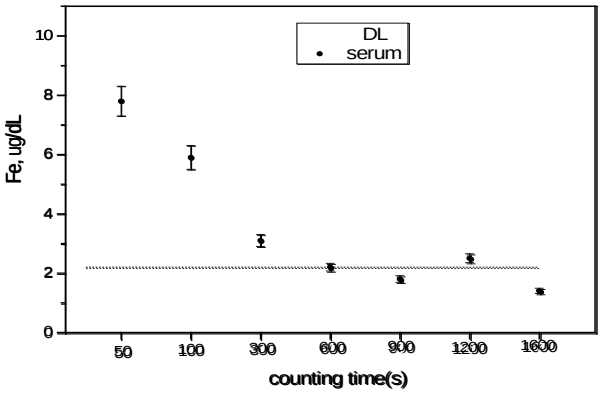

FIG. 4 SERUM DETECTION LIMIT USING PXRFS

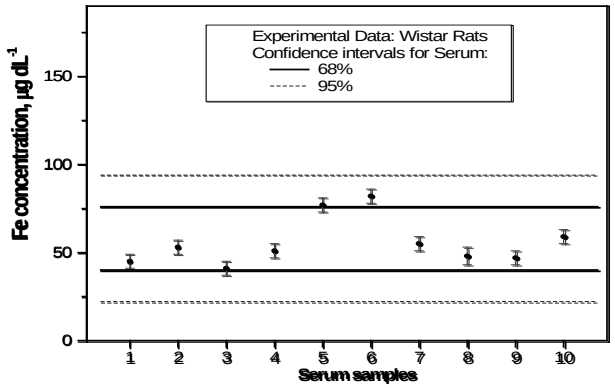

FIG. 5 SERUM IRON CONCENTRATIONS

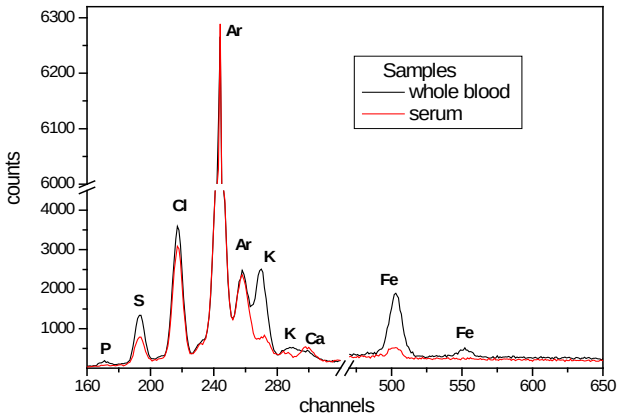

FIG. 6 WHOLE BLOOD AND SERUM SPECTRA USING MINI X-RAY SPECTROMETER

The XRF technique using the MINI-X Spectrometry showed to be adequate for Fe determination in whole blood, serum and urine samples from animal model. Its applicability requires a small amount of biological material, short time of analysis (minutes) and simple sample preparation. Moreover, the samples can be stored for a long period for future examination without refrigeration.

Recently, the MINI X-Ray Fluorescence Spectrometry performance was investigated to be used for clinical practices for Iron determination in whole blood and serum samples of Brazilian population showing to be appropriate for this clinical finalities. These results also emphasis its application in clinical laboratories.

Considering the viability of using MINI-X Ray Spectrometer for clinical investigations using whole blood, serum and urine, other elements also relevant in clinical practice, such as Ca, Cl, K,P and S, can also been evaluated simultaneously.

Finally, it is also relevant to discuss about the economic viability. According to the last Program External Quality Assessment of clinical laboratories (Brazil, 2012), 1.4 billion clinical tests have been done (~ 4% are biochemical test, mainly for Ca, Cl, Fe and K); moreover, it is estimated an increase of about 2% of clinical examinations in 2014. Considering these estimates, the MINI X-ray spectrometer can be an economical alternative for clinical practice, especially in underserved regions with poor medical care and hospitals.

Conclusions

This tool could help the researchers to evaluate the efficiency of new treatments as well as to compare the advantages of different treatment approaches, before performing tests in human being in fast and economic way. The principal audiences are researchers who work in health and related area using experimental animals, such as: Veterinary Toxicology, Immunology, Nutrition and Genetics. Additionally, this alternative procedure meets the needs of the Brazilian legislation that emphasizes the need to propose alternative methods for clinical practice that contribute to animal welfare.

ACKNOWLEDGMENT

The authors would like to acknowledge the Conselho Nacional de Desenvolvimento Científico e Tecnológico (CNPq) and Instituto de Pesquisas Energéticas e Nucleares (IPEN) for the financial support.

REFERENCES

Aguiar Rodrigo O., Zamboni Cibele B., Medeiros José A. G. "Analysis of Ca and Mg in blood of golden hamster using NAA technique" In: Proceedings of International Nuclear Atlantic Conference (INAC) 2009, Rio de Janeiro, ABEN.

Metairon Sabrina, Zamboni Cibele B., Suzuki Miriam F., Bueno Carlos R. Jr., Sant'Anna Osvaldo A., "Elemental analysis of biological tissues of Dmd^{mdx}/J and C57BL/6J mice strains investigated by NAA." J Radioanal Nucl Chem 296(2013): 579-84.

Metairon Sabrina, Zamboni Cibele B., Suzuki Miriam F., Bueno Carlos R. Jr., Sant'Anna Osvaldo A., "Elemental analysis of biological tissues of animal models in muscular dystrophies investigation." J Radioanal Nucl Chem 291(2012): 373-78.

Oliveira Laura C., Zamboni Cibele B. "Determination of reference values of elements in whole blood of the wistar rats using NAA." In: Proceedings of International Nuclear Atlantic Conference (INAC) 2011, Belo Horizonte, ABEN.

Oliveira Laura C., Zamboni Cibele B., Genezini Frederico A., Figueiredo, Ana M. G., Zahn Guilherme S. "Use of thermal neutrons to perform clinical analyses in blood and urine samples." J Radioanal Nucl Chem 263(2005): 783 - 786.

Oliveira Laura C., Zamboni Cibele B., Pessoal Edson. A., Borges, Fernanda T. "Characterization of ions in urine of animal model with acute renal failure using NAA." AIP, 1351 (2011): 353-356.

Redígolo Marcelo M., Aguiar Rodrigo O., Zamboni Cibele B., Sato Ivone M., "Determination of reference interval values for inorganic elements in whole blood samples of humans and laboratory animals by X-ray fluorescence spectrometry." J Radioanal Nucl Chem 297(2013): 463-67.

Zamboni Cibele B., Aguiar Rodrigo. O., Kovacs Luciana, Suzuki Miriam F., Sant'Anna Osvaldo A., "NAA technique for clinical investigation of mice immunized with Bothrops venom." AIP, 1139(2009): 166-67.

Zamboni Cibele B., Metairon Sabrina, Oliveira Laura C., Simons Simoni M., Chudzinski-Tavassi Ana M., Oliveira

Daniela G. L., "Determination of elements in blood of White New Zealand rabbits by NAA." J Radioanal Nucl Chem 291(2012): 433-37.

Zamboni Cibele B., Metairon Sabrina, Suzuki Miriam F., Furtado Marcia F., Sant' Anna Osvaldo A., Tambourgi Denise V. "Quantitative evaluation of blood elements by neutron activation analysis in mice immunized with Bothrops snake venoms." J Radioanal Nucl Chem 282 (2009): 37 - 39.

Zamboni Cibele B., Suzuki Miriam F., Metairon Sabrina, Sant' Anna Osvaldo A. "Investigation of whole blood of SJL/J mice using neutron activation analysis." J Radioanal Nucl Chem 281(2009): 97–99.

Zamboni Cibele B., Suzuki Miriam F., Sant' Anna Osvaldo A. "Simultaneous determination of five elements in whole blood of dystrophin-deficient mdx mouse by NAA." J Radioanal Nucl Chem 278(2008): 585 - 589.

Zamboni, Cibele B., Metairon, Sabrina, Marcia A. Rizzutto and Suene B. dos Santos, "The use of Portable X-Ray Fluorescence Spectrometry (PXRFS) for clinical practices" [Proccendigns of Science, Dezember 1-6, 2013] in press.

An Electromagnetic Gauge Technique for Measuring Particle Velocity of Electrically Conductive Samples in Extreme Conditions

David X.P. Cheng[*1], Akio Yoshinaka[2]

Defence Research and Development Canada – Suffield
PO Box 4000, Station Main, Medicine Hat, Alberta T1A 8K6 Canada

[*1]david.cheng@drdc-rddc.gc.ca; [2]akio.yoshinaka@ drdc-rddc.gc.ca

Abstract

This paper presents an electromagnetic velocity (EMV) gauge technique which allows use of conductive samples in the measurement of material velocity subject to shockwave compression. A dynamic model of the induced current in the EMV gauge caused by the conductive samples moving in a uniform magnetic field is developed and the motional emf generated in the EMV gauge is extracted from the measured signal. Experimental results are presented and discussed to demonstrate the effectiveness of the technique.

Keywords

Electromagnetic velocity gauging; Shockwave; Particle velocity

Introduction

Piezo-resistive film gauges are used regularly to determine normal stress in matter under shock compression. The functionality of these gauges relies on a pre-calibrated relationship between the change in relative resistance and the change in normal stress. Under extreme conditions, both substrate and adhesive constituents of these gauges can undergo phase and/or chemical changes whose effects on the overall performance of the gauge are not clear (Rosenberg, 2009). Electromagnetic velocity (EMV) gauges are another class of film gauges which permit the direct in-situ measurement of shocked material flow velocity. The active sensing element does not need pre-calibration; rather, this method requires exposure of the moving element to a well quantified external static magnetic field in order to produce motional electromotive force (emf). While applications of this technique for measuring velocities of shocked materials have been widely reported in the literature (Sheffield, 1999; Fritz, 1973), it is limited to non-metallic materials only. This is due to signal distortion caused by the induced currents within electrically conductive materials moving in an externally applied magnetic field at high velocities. To use an EMV gauge with conductive samples, the motional emf generated in the pickup foil has to be extracted from the measured signal which results from the superposition of both motional emf and voltage from induced currents.

In this paper an electromagnetic technique is developed which uses an analytical model to estimate the dynamics of induced current between the copper substrate and the EMV gauge. The former is modelled as a non-magnetic conductor moving in a uniform magnetic field with a uni-directional translational velocity. The Foucault current in the moving conductor is discretized as a piece-wise constant signal. For a mm thick copper sample disk moving in a static magnetic field with a uniform translational velocity, the volume conductor is modelled as a magnetic dipole loop carrying a current and the EMV gauge is modelled as a closed circuit loop moving in the field of the magnetic dipole. The field produced by the magnetic dipole is calculated throughout the space in which the pickup foil gauge moves. Equations of mutual induction are derived and the induced current in the EMV gauge loop is solved numerically, which allows separation of the emf signal for measurement of the particle velocities. Numerical analysis is provided for the induced current in the EMV gauge with respect to the Foucault current in a copper sample undergoing a step wise change in velocity. A few experiments were performed in an attempt to demonstrate the feasibility of the proposed technique to compensate for signal distortion in measuring particle velocities of shock compressed copper. The ability to use EMV gauges within samples of high

conductivity complements our use of manganin film stress gauges to quantify shocked states in matter.

EMV Gauge Modelling

Fig. 1 shows the setup for the EMV gauging technique described in this paper. A shock wave is transmitted into a sample, comprising a copper disk above and below an insulated metallic foil element, where both copper and foil element are set in motion and, under the influence of an external magnetic field, generate a signal that is proportional to their velocity. According to Faraday's law, the particle velocity of the sample is given by $v = Bl/V_1$, where V_1 is the voltage across the active foil element, B is the average magnetic flux density as measured with a Gaussmeter at the location of the gauge, l is the length of the active element and v is the velocity of the gauge.

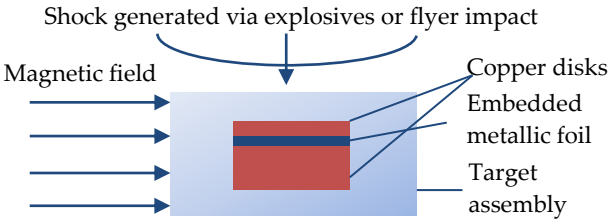

FIG. 1: EMBEDDED ELECTROMAGNETIC VELOCITY GAUGES WITH EXTERNALLY APPLIED MAGNETIC FIELD

A Model of the Induced Magnetic Field

In this paper, only the copper disk above the gauge is modeled as a loop of radius a carrying a current I_1 and moving along the z-axis with a constant translational velocity v toward the EMV gauge, as shown in Fig 2. The effect of induced current from the copper disk downstream from the gauge is for now neglected for simplicity.

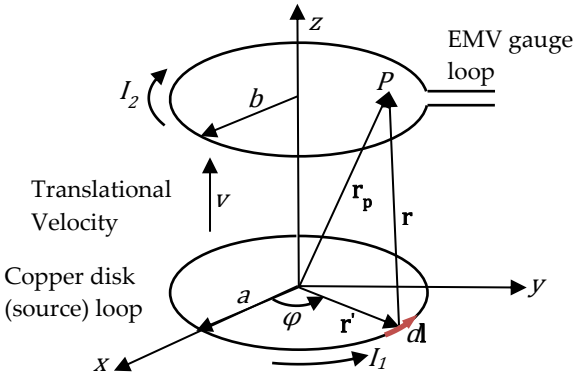

FIG. 2: MODELS FOR THE EMV GAUGE AND COPPER DISK

By the Biot-Savart law, the magnetic field at a point P on the surface of the EMV gauge loop is

$$\mathbf{B} = \frac{\mu_0 I_1}{4\pi} \oint \frac{d\mathbf{l} \times \mathbf{r}}{r^3} \tag{1}$$

where

$$\mathbf{r} = -a\cos\varphi\mathbf{i} + (y - a\sin\varphi)\mathbf{j} + z\mathbf{k} \tag{2}$$

with a magnitude

$$r = (a^2 + y^2 + z^2 - 2ay\sin\varphi)^{1/2} \tag{3}$$

The differential current loop element satisfies

$$d\mathbf{l} = -a\sin\varphi\, d\varphi\mathbf{i} + a\cos\varphi d\varphi\mathbf{j} \tag{4}$$

The cross product $d\mathbf{l} \times \mathbf{r}$ becomes

$$d\mathbf{l} \times \mathbf{r} = \begin{vmatrix} \mathbf{i} & \mathbf{j} & \mathbf{k} \\ -a\sin\varphi d\varphi & a\cos\varphi d\varphi & 0 \\ -a\cos\varphi & y - a\sin\varphi & z \end{vmatrix} = ad\varphi[z\cos\varphi\,\mathbf{i} + z\sin\varphi\,\mathbf{j} + (a - y\sin\varphi)\mathbf{k}] \tag{5}$$

From eq. (1) the magnetic field at a point P on the EMV gauge loop surface is

$$B_x = 0 \tag{6}$$

$$B_y = \frac{\mu_0 I_1 az}{4\pi} \int_0^{2\pi} \frac{\sin\varphi\, d\varphi}{(a^2 + y^2 + z^2 - 2ya\sin\varphi)^{3/2}} \tag{7}$$

$$B_z = \frac{\mu_0 I_1 a}{4\pi} \int_0^{2\pi} \frac{(a - y\sin\varphi)d\varphi}{(a^2 + y^2 + z^2 - 2ya\sin\varphi)^{3/2}} \tag{8}$$

B_y and B_z can be expressed as elliptic integrals and computed numerically. On the z-axis where y=0, B_y and B_z are

$$B_y = 0, \quad B_z = \frac{\mu_0 I_1 a^2}{2(a^2 + z^2)^{\frac{3}{2}}} \tag{9}$$

Models of the Copper Disk and EMV Gauge Loops

Let the mutual inductance of the copper disk and the EMV gauge loops be M_{12}. The circuit equations for the two loops can be expressed as

$$R_1 I_1 + L_1 \frac{dI_1}{dt} + \frac{dM_{12}}{dt} I_2 + M_{12} \frac{dI_2}{dt} = V_1 \tag{10}$$

$$L_2 \frac{dI_2}{dt} + R_2 I_2 + \frac{dM_{12}}{dt} I_1 + M_{12} \frac{dI_1}{dt} = 0 \tag{11}$$

In a configuration where the distance between the copper disk and the EMV gauge is much smaller than the radius of the current loops (i.e., $z \ll a$), the magnetic field generated by the source loop can be approximated by the magnetic density on the z-axis, given by eq. (9), and the magnetic flux going through the EMV gauge loop can be simplified as

$$M_{12} I_1 = B_z(0,0,z)(\pi b^2) = \frac{\mu_0 \pi I_1 a^2 b^2}{2(a^2 + z^2)^{\frac{3}{2}}} \tag{12}$$

And the mutual inductance can be expressed as

$$M_{12} = \frac{\mu_0 \pi a^2 b^2}{2(a^2 + z^2)^{\frac{3}{2}}} \tag{13}$$

Thus the total time derivative of M_{12} is

$$\frac{dM_{12}}{dt} = \frac{dM_{12}}{dz} \cdot v = -\frac{3\mu_0 \pi a^2 b^2 v}{2} \cdot \frac{z}{(z^2 + a^2)^{2.5}} \tag{14}$$

where v is the moving velocity of the copper disk toward the EMV gauge. To simplify the problem, we assume that the current running around the copper disk loop I_1 holds a constant value in a short time interval so that eq. (11) becomes

$$L_2 \frac{dI_2}{dt} + R_2 I_2 = -\frac{dM_{12}}{dt} I_1 \tag{15}$$

Applying eq. (14), we get

$$L_2 \frac{dI_2}{dt} + R_2 I_2 = I_1 \cdot \frac{3\mu_0 \pi a^2 b^2 v}{2} \cdot \frac{z}{(z^2 + a^2)^{2.5}} \tag{16}$$

To perform a modal analysis for the induced current I_2, we define the following dimensionless ratios

$$\tau = \frac{v}{a} t, \quad \rho = \frac{L_2 v}{a R_2}, \quad I = \lambda \frac{I_2}{I_1}, \quad \lambda = \frac{2aL_2}{3\mu_0 \pi b^2} \tag{17}$$

Substituting (17) into (16), we derive the modal equation for the induced current in terms of the ratio I

$$\frac{dI}{d\tau} + \frac{1}{\rho} I = \frac{\tau}{(\tau^2 + 1)^{2.5}} \tag{18}$$

which can be solved numerically as shown in Fig. 3. From the numerical solutions of the induced current, we have observed that

a. The Foucault currents in the copper disk moving with a uniform velocity induce currents on the EMV gauge before the gauge starts to move.
b. The induced current causes a reversal of the emf signal with a positive overshoot.
c. The positive overshoot extends for a longer time with higher copper disk velocity.

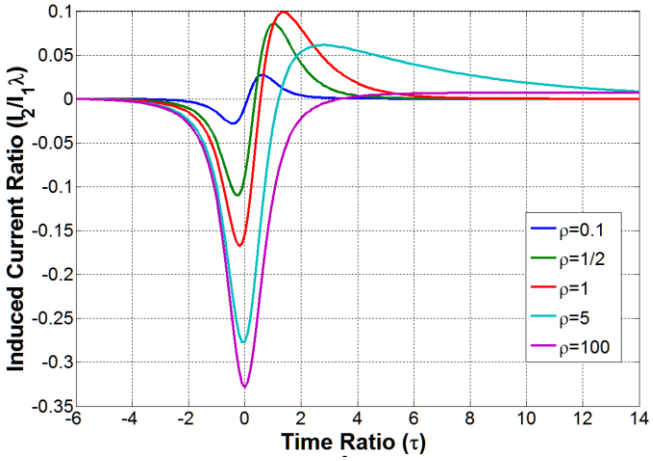

FIG. 3 MODES OF INDUCED CURRENTS IN THE EMV GAUGE

Modal Analysis

The procedures for applying modal analysis to the experimental data for signal extraction are as follows:

- Step 1: Use a Fast Fourier Transform to low-pass filter the raw experimental data in order to get a smoothed curve so that the mode shapes are evident.
- Step 2: Determine the boundary values of the emf that corresponds to the modes of the induced current demonstrated in Fig. 3.
- Step 3: Solve eq. (18) as a boundary value problem and obtain a modal solution.
- Step 4: Apply the modal to the smoothed experimental data by means of superposition.
- Step 5: Repeat Steps 2 to 4 until the mode shape is not evident on the curve of the experimental data.
- Step 6: Combines all the modals solved from Steps 2 to 5 to construct a complete induced emf profile and extract the motional emf from the raw signal.

Experimental Tests, Results and Discussion

In order to test the performance of the models of signal extraction for EMV gauging in shock wave environments, a number of trials were performed whereby composition C-4 military explosive, hand packed in a PVC tube (52mm i.d. x 4.2mm wall x 203mm high for test 275A and 20.2mm i.d. x 3.3mm wall x 101mm high for test 295A) was used to generate an incident shock wave in copper.

The EMV gauges used for the tests were manufactured in-house (Fig. 4 (a)). A 25μm thick brass foil was cut with an active length of 10 mm, which produces motional emf when moving through a magnetic field. The foils were encapsulated with 250μm (test 295A) or 500μm (test 275A) thick Teflon adhesive sheets on both sides. The completed gauges were then embedded between two copper disks (31.75 mm dia. x 3.09 mm thick above and 22 mm thick below for test 295A, and 57.05 mm dia. x 3.09 mm thick above and 10 mm thick below for test 275A) using liquid epoxy adhesive, as shown in Figs. 4 (b) and (c).

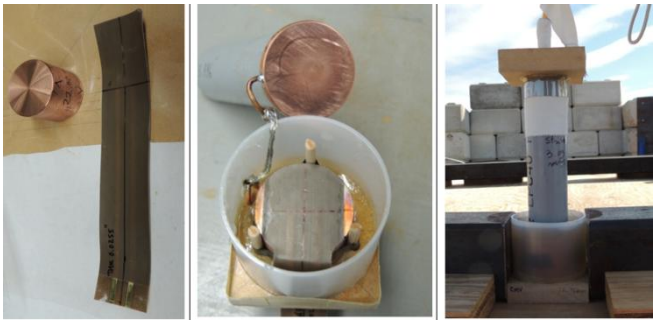

FIG. 4 (A) IN-HOUSE MADE EMV GAUGE AND (B) EMV GAUGE IN THE TARGET SAMPLE (C) DONOR/TARGET ASSEMBLY

For trial 275A, a 75 Ω resistor was connected in series with the EMV gauge and terminated with 75 Ω on a single scope channel for impedance matching of the whole gauge circuit loop. For trial 295A, each lead of the EMV gauge was connected to a different oscilloscope channel via the center conductor of a 1.5 m long RG-179 coaxial cable, resulting in a differential input to reject common mode noise. Each channel was terminated with 75 Ω and the voltage difference between these channels provided us with a measure of voltage across the foil, accounting for resistive losses across cables. The top and bottom copper disks were grounded to a central grounding point at the instrumentation bunker for all tests.

An electromagnet built in-house was used to provide an external static magnetic field. The magnet essentially consisted of 50.8 mm square A36 mild steel bars used as pole pieces, two of which were wrapped with #8 AWG cable. A switching DC power supply was used to provide the coils with a constant current.

Calibration of the electromagnet was performed before every trial. The variation of magnetic flux density (B) with vertical position along the center of the pole piece gap where EMV gauges were located was measured, and an average flux density was used for simplicity. The variation in B along the sensing width of the EMV foil is neglected, since lateral fluctuations in the magnetic field were within better than 1% over the gauge width.

The EMV gauge model developed in this paper is applied to the velocity data of the copper samples acquired in two of the EMV gauging trials. A separate experiment was performed to determine the normal stress at the location of the EMV gauge within the target sample for trial 295A using a Dynasen Inc. MN10-0.050-EPTFE manganin gauge. The copper material velocity was then calculated via the known Hugoniot data (Marsh, 1980) given the normal stress at the EMV gauge location. The measured peak normal stress was 20.6GPa which corresponds to a particle velocity of 0.50mm/μsec.

From the raw experimental data (Figs. 5 and 8), we can observe that in both trials the waveforms first show a negative peak with a magnitude ranging between 0.34–0.41mm/μsec. The EMV gauge model developed in this paper suggests that the moving top copper disk perturbed the magnetic field and induced a current in the EMV gauge circuit before the gauge produced motional emf. This is followed by a positive peak, where the motional emf from the EMV gauge is embedded.

The modal analysis is performed on both waveforms using the procedures described in last section. Twenty-six modals (Fig. 6) for the data of trial 295A, and thirty-five modals (Fig. 9) for trial 275A, were solved at various time instants with suitable strength (i.e., satisfying the boundary values), and then applied to the waveforms to compensate for the negative signal distortion and positive signal perturbation on the EMV gauge. It should be noted that all the EMV gauge model outputs are shown in terms of velocities that are converted from the corresponding induced current in the EMV gauge. The results are shown in Figs. 7 and 10. The negative reversal signals were nearly eliminated and the positive signals were also compensated for the extended effect of the induced currents. In Fig. 7, the extracted EMV gauge signal shows an average peak value of 0.53 mm/μsec for trial 295A, which matches the peak value of 0.50 mm/μsec inferred by the manganin gauge for trial 295A. The charge diameter for trial 275A was about 2.6 times larger than and twice as long as the donor charges in all other tests. A higher average peak value of 0.72mm/μsec particle velocity is observed from the output of the EMV gauge model for trial 275A, as shown in Fig. 10, which appears to confirm the expected greater delay in both lateral and rear expansion waves. These values suggest that the EMV gauge model provides a correct measure of the incident particle velocity.

It can be also observed in Figs. 7 and 10 that the EMV gauge model increases the period over which an effective measurement of particle velocity can be made. In trial 295A the effective measurement time was extended from about 0.15 to 0.26 μsec, whereas in trial 275A it was extended from about 0.2 to 1 μsec.

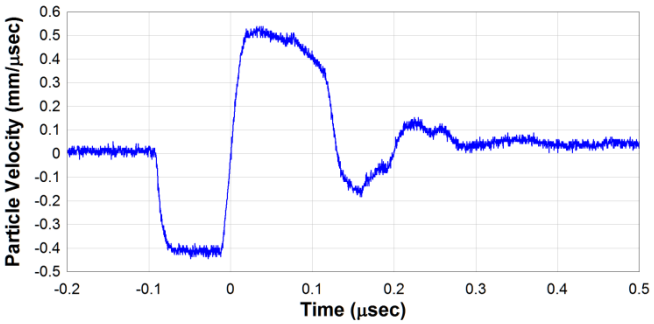

FIG. 5: PARTICLE VELOCITY RAW DATA CONVERTED FROM EMF MEASURED BY THE EMV GAUGE IN TRIAL 295A

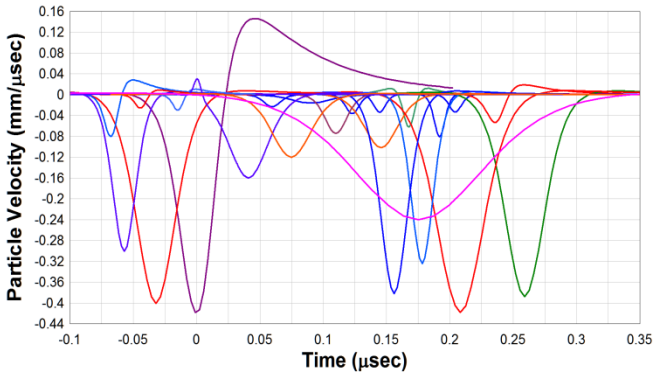

FIG. 6: CONVERTED MODES OF INDUCED EMF SOLVED FROM THE INDUCED CURRENT MODEL FOR TRIAL 295A

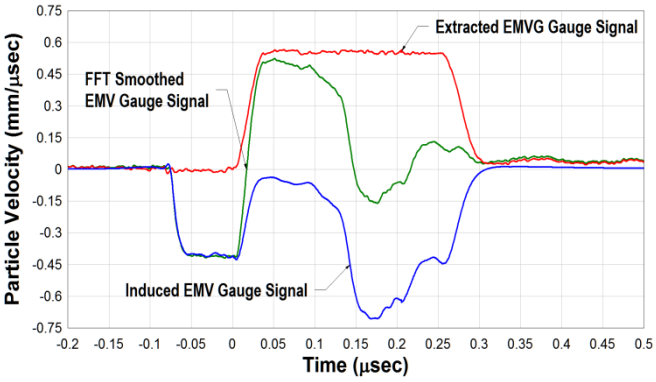

FIG. 7: COMPARISON OF THE INPUT, INDUCED AND EXTRACTED EMV GAUGE SIGNALS FOR TRIAL 295A

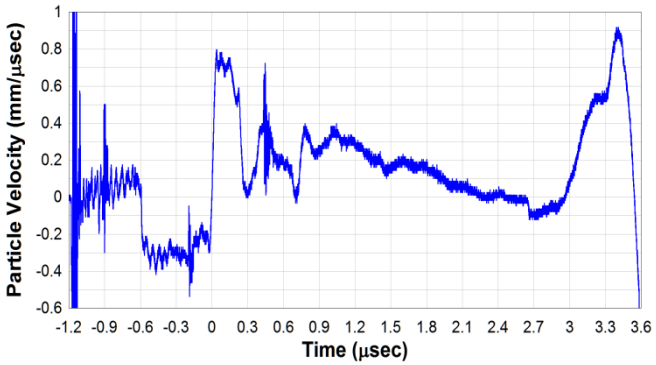

FIG. 8: RAW DATA OF THE PARTICLE VELOCITY CONVERTED FROM EMF MEASURED BY THE EMV GAUGE IN TRIAL 275A

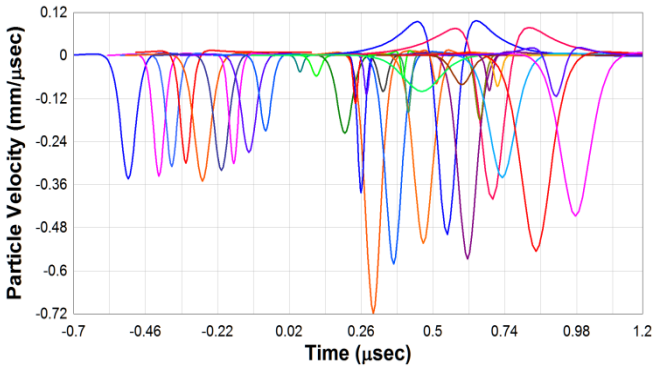

FIG. 9: CONVERTED MODES OF INDUCED EMF SOLVED FROM THE INDUCED CURRENT MODEL FOR TRIAL 275A

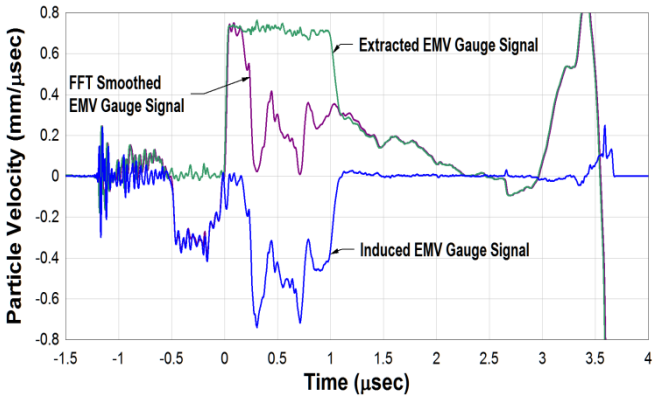

FIG. 10: COMPARISON OF THE INPUT, INDUCED AND EXTRACTED EMV GAUGE SIGNALS FOR TRIAL 275A

Conclusions

A model was developed in attempt to discriminate motional emf from the resultant signal produced by an electromagnetic velocity (EMV) gauge embedded within shock compressed copper. While the current model only accounts for the effects of bulk motion of a copper sample on the upstream (relative to the direction of shock propagation) side of the EMV gauge, the results suggest that it is possible to eliminate the negative signal distortion induced by a moving conductor in an external magnetic field, thereby extending the measurement of particle velocity history (up to 1 µsec for the cases examined in this paper). Although the EMV gauge technique developed in this paper requires further development to account for the fact that a moving conductor was also located dowstream of the gauge, we expect that a similar model designed to capture a bulk copper volume moving away from the foil gauge could further extend the useful part of the velocity signal. Further model refinement will be needed to confirm this.

REFERENCES

Rosenberg, Z., Ginzberg, and A., Dekel, E. "High shock pressure measurements using commercial manganin gauges." INT J IMPACT ENG, 36(12):1365-1370, 2009.

Sheffield, S., Gustavsen, R., Alcon, R. "In-situ magnetic gauging technique used at LANL." Los Alamos National Laboratory report LA-UR-99-3277, 1999.

Fritz, J. N., Morgan, J. A. "An electromagnetic technique for measuring material velocity." Review of Scientific Instruments. 44 (2): 215-221, 1973.

Marsh, S.P. "LANL Shock Hugoniot Data." University of California Press, 1980.